Programmable Individual Addressing and Floquet Hamiltonian Dynamics in a Trapped Ion Quantum Processor

by

Chung-You Shih

A thesis
presented to the University of Waterloo
in fulfillment of the
thesis requirement for the degree of
Doctor of Philosophy
in
Physics (Quantum Information)

Waterloo, Ontario, Canada, 2023

Examining Committee Membership

The following served on the Examining Committee for this thesis. The decision of the Examining Committee is by majority vote.

External Examiner:	Amar Vutha Associate Professor, Department of Physics, University of Toronto
Supervisor(s):	Kazi Rajibul Islam Associate Professor, Department of Physics and Astronomy, University of Waterloo
Internal Member:	Thomas Jennewein Associate Professor, Department of Physics and Astronomy, University of Waterloo
Internal Member:	Roger Melko Professor, Department of Physics and Astronomy, University of Waterloo
Internal-External Member:	Michal Bajcsy Associate Professor, Department of Electrical and Computer Engineering, University of Waterloo

Author's Declaration

I hereby declare that I am the sole author of this thesis. This is a true copy of the thesis, including any required final revisions, as accepted by my examiners.

I understand that my thesis may be made electronically available to the public.

Abstract

Trapped ions have been gaining traction as a platform for quantum information processing (QIP) in both academia and industry over the last decade. Their long coherence time, high fidelity gate operations, and built-in all-to-all connectivity are some of the key features that make trapped ions promising. However, to unlock the full potential of the trapped ion platform, sophisticated quantum controls are required. In this thesis, we present our efforts in individual optical addressing to control an ion's quantum state at an individual level, as well as efforts in generating complex and time-dependent Hamiltonians through arbitrary radio frequency (RF) waveform generation.

We present two types of individual addressing systems. One is based on a holographic beam shaping technique. We experimentally show that an intensity crosstalk level of 10^{-4} can be achieved, translating to a greater than 99.9% fidelity in individual quantum state control and 99.6% fidelity in individual spin readout without corrupting the adjacent ion's quantum state.

The other addressing system is specifically optimized for coherent manipulation of qubits with Raman beams in contrast to the addressing system described in the previous paragraph. This system is based on acousto-optic deflectors (AOD). We have designed a mirrored setup to compensate for site-dependent frequency shifts that result from the intrinsic properties of the AOD. The Raman transition is a two-photon process where only the frequency difference between the two beams matters. The two AODs produce the same amount of site-dependent frequency shift, which cancels out in the frequency difference. Simulations show that the system is capable of addressing 30-50 ions with crosstalk at a sub-10^{-4} level.

The presented individual addressing systems can be applied to different species operated with different wavelengths. The holographic beam shaping system has even greater flexibility in that it can be applied to various quantum systems, such as neutral atom arrays or nitrogen vacancy centers in diamonds.

In addition to the individual addressing system, we also present our efforts in constructing complex and time-dependent Hamiltonians utilizing an arbitrary waveform generator. We use it to engineer and study the Floquet Hamiltonian. This type of system is intriguing because spatiotemporal orders can emerge from a quantum chaotic system. In this thesis, we use it to generate a transverse field Ising model with an additional time-dependent Floquet drive. Under specific conditions, the Floquet drive exhibits emerging conservation in total magnetization. We experimentally demonstrate dynamic freezing behavior for the total magnetization in a four-ion system and show that the Hilbert space is fragmented into multiple sectors with different total magnetizations.

Lastly, we also present our approach in various aspects of efforts in scaling up a trapped ion quantum processor. This includes building high-stability optics boards, analysis on scalable detection with qualitative CMOS (qCMOS) technology, and the in-house design of a microscope objective tailored for experimental requirements.

Acknowledgements

I would like to express my deepest gratitude to all those who have supported me throughout the journey of completing this thesis.

First and foremost, I am immensely thankful to my advisor, Dr. Kazi Rajibul Islam, whose unwavering guidance, patience, and expertise have been instrumental in shaping this research. I feel extremely lucky to be able to start my Ph.D. as the first generation of the graduate student in his labs. Being able to build the lab from scratch and learn the fist-hand knowledge and experience from him is a truly valuable and remarkable experience. Beyond his guidance in research, Rajibul deeply cares about the well-being of the graduate students and always strives to make the lab a friendly working environment. Doing research is never an easy job, but in a friendly environment and with support from the advisor, every challenge becomes a lesson, every failure a stepping stone to success. His constant encouragement and support have been the driving forces behind my academic and personal growth, allowing me to overcome the myriad of hurdles encountered during this journey, and for that, I am profoundly grateful.

I would also like to express my gratitude to my thesis committee: Dr. Thomas Jennewein, Dr. Roger Melko, and Dr. Michal Bajsy, for their valuable advice throughout my journey. A special thank you to the external examiner, Dr. Amar Vutha for his constructive criticism and for accepting the role of external examiner at short notice.

Building a complex trapped ion apparatus requires teamwork. I am truly grateful that I can meet all my amazing colleagues. Dr. Roland Hablützel, Sainath Motlakunta, and Nikhil Kotibhaskar built the lab with me. At my early stage of the Ph.D., Roland, who worked as the postdoc in the lab study, gave me much guidance. Nikhil and Sainath started their Ph.D. around the same time, and it's been a pleasure to build the lab side by side. Not only on the research, having you two to work through the obstacles and milestones together in the Ph.D. journey has been enriching. I'd also like to thank my colleagues who joined the lab later, the newer generation of the graduate students, including Anthony Vogliano, Jingwen (Monica) Zhu, and Lewis Hahn. It's a pleasure to work with you, and I sincerely wish you all the best for your Ph.D. journey. I thank Dr. Yu-Ting Chen and our theory collaborators, Dr. Asmi Haldar and Dr. Arnab Das, for their valuable contributions to the Floquet Hamiltonian experiment presented in this thesis.

In the University of Waterloo, we have a co-op program, I had many chances to work with many brilliant co-op students on various projects. Many research projects we did in the lab would not have been possible without their contributions. It's a pleasure to work with these brilliant minds. Not only just me mentoring them on projects, but I often find

myself learning many new things from them. I want to say thank you to Kalab Ruscitti on the holographic engineering projects, Austin Con on participation in lenses design and custom software development for aiding optical pegboard design, and Ziyan (Jerry) Li, Ryan Mark, Mariah De Torres, and Paige Angela Harford on high stability optics for our next-generation optics.

Staring a new lab requires building many infrastructures. It's a task that demands precision, proficiency, and a vast array of knowledge. I want to thank Steve Weiss for the assistance in setting up the necessary IT infrastructure with me and Chris Kleven for the help on the AC system and the lab renovation.

I also would like to extend my gratitude to Judy McDonnell and Kayla Sutton from the physics department, who have been our pillars of support, assisting us graduate students in myriad ways. Their professionalism and kindness have significantly eased the handling of paperwork, allowing us to focus on our research with fewer distractions and worries. I'd also like to thank the physics department and the Institute for Quantum Computing for the financial support throughout my Ph.D. journey.

Outside of the lab and the research, my heartfelt thanks go to all my friends and family for their emotional support, which was an anchor through the turbulent times of this journey.

Elena Kwon and Martinet Lee, my housemates through most of my Ph.D. and the pandemic era, deserve special mention. Not only sharing the same household, but we also shared countless delightful moments and hearty laughter. I cherish all the memories and conversations we had at 34 Elgin.

I wish to convey my profound appreciation to my girlfriend, Ruoxuan Xu, for her continuous emotional support throughout this journey. Her unwavering belief in me has been a source of strength, encouragement, and inspiration. Thank you for being my pillar, especially during the final leg of this journey, where every word of encouragement and every gesture of support meant a lot to me.

Last, but certainly not least, I want to thank my parents for their unceasing support as I pursued a Ph.D. for many years. The pandemic has kept us apart, but it is their love, support, and values that have fortified my resolve on this journey. Now, as I stand at the end of this fruitful journey, a journey filled with learning, growth, and discovery, I eagerly await the moment I can return home and envelop them in a heartfelt hug to convey my immense gratitude and love for them.

Finally, I would like to thank all the individuals whose names may not appear here but whose contributions, in one way or another, have been vital to the completion of this thesis.

Dedication

To my colleagues, friends, and family, who have supported me throughout this journey.

Table of Contents

Chapter 1

Introduction

Trapped ions have become one of the leading platforms for quantum information processing (QIP). Researchers have been using it for studying various intriguing topics, including simulating quantum field theories[17, 46, 28, 53], estimating properties of molecules[52, 33], studying quantum many-body physics[74, 49, 63], and more.

In addition to its academic significance, the trapped ion as a QIP platform is earning recognition within the industry as a potential pathway towards achieving general quantum computing or domain-specific optimizers[32] capable of resolving intricate problems. For example, IonQ Inc. successfully raised $84 million in its Series B funding round for constructing a trapped ion quantum computer. Similarly, Honeywell International, a NASDAQ 100 company, joined forces with Cambridge Quantum Computing to establish Quaninuum, dedicated to the same ambition.

Long coherence time[68], natural all-to-all connectivity[41], excellent quantum gate fidelity[27], and multiple-level quantum states[43] for densely encoding quantum information are some key advantages of trapped ion quantum computing. To unlock the full potential of a trapped ion quantum processor, it is crucial to have sophisticated quantum controls. In the context of trapped ions, laser-induced light-matter interactions are the most common way of manipulating the quantum state of the ions.

We can view quantum controls in two dimensions: spatial quantum controls and temporal quantum controls. Spatial quantum controls refer to controlling the quantum state of each individual ion. However, implementing high-quality individual optical addressing is fundamentally challenging. The typical inter-ion spacing in trapped ion quantum apparatuses is 4-6 μm, a good compromise between individual addressing capability and ion-ion interaction strength. Bringing the ions closer to each other enhances Coulomb interactions

between them, thus accelerating multi-qubit quantum operations. Nonetheless, this demands lens systems with higher numerical apertures (NA) to resolve individual ions for individual addressing. Any leakage of the laser beam to the adjacent ions will result in errors, which is referred to as crosstalk. In this thesis, we present our solutions in engineering individual ion addressing systems in chapters 4 and 6.

As for the temporal quantum controls, they are required for engineering complex Hamiltonians and/or time-dependent Hamiltonians. For trapped ions, this often involves generating multiple phase-referenced RF frequencies and the capability to modulate the RFs over time. We will discuss how we engineer various types of Hamiltonians and use them to study a time-dependent Floquet quantum system in chapter 5.

A Floquet system refers to a periodically driven system. Recent studies show that spatiotemporal orders in spins can emerge from it, instead of becoming "thermalized" and featureless [73, 11]. Rather than studying the Floquet system in the perturbative regime, we investigate the system in the strongly driven regime, which is rarely studied experimentally, in this thesis.

Beyond spatial and temporal quantum controls, we can also categorize controls based on their impact on the quantum states. The operations we perform can be classified as either coherent or non-coherent quantum operations.

Coherent quantum operations encompass actions like forming entanglement between the quantum states of a pair or multiple ions, rotating the quantum sphere on the Bloch sphere, and engineering spin-spin interactions. These operations are fundamental building blocks for quantum algorithms and Hamiltonian quantum simulation.

In contrast, non-coherent quantum operations involve the collapse of all or part of the system's quantum state, and these are typically irreversible. Reading out information, resetting quantum states, or tracing out part of the system are a few of the non-coherent quantum operations. Well-engineered controls over these quantum operations are essential for applications like quantum error correction, research on measurement-induced phase transitions, and open quantum system studies.

Scalability is a key consideration when discussing quantum controls. As the number of controllable ion qubits increases, the Hilbert space capable of encoding the quantum information expands exponentially. This growth is one of the factors that could potentially allow a quantum processor to outshine its classical counterpart in certain problems.

Hence, our design goals for quantum controls extend beyond high precision and low error. We also strive for compatibility with a large number of ions. Throughout the thesis, we will consistently examine the scalability of the quantum controls we designed. Given the

diverse properties exhibited by different quantum operations, a single solution may not be universally applicable. For example, chapters 4 and 6 both describe individual addressing systems, but one may be better suited for non-coherent quantum controls while the other may be more appropriate for a specific type of coherent quantum control.

1.1 Chapter Outline

My PhD journey commenced in the Fall term of 2019, two months after we trapped the first ion, with our first generation ion trap apparatus, which uses a four-rod Paul trap (Sec. 3.2). At that point, I had just completed my M.Sc. degree in the same group.

The four-rod apparatus, in the design and construction of which I participated during my M.Sc. studies, was not optimized to work with a large number of ions due to its limited optical access and low trapping frequencies. These limitations were intrinsic to its ion trap design and the design of the vacuum chamber, neither of which were easily upgradeable. As the first-generation ion trap apparatus in the lab, the four-rod apparatus was intended to validate new ideas and develop new techniques.

To overcome these limitations, we began designing the next-generation ion trap apparatus. The objective for this new apparatus was to trap ∼30-50 ions while providing control at the individual ion level. At this scale, the system's Hilbert space becomes too large to simulate classically, even with the most powerful supercomputers, potentially opening the door to quantum advantage. Given the complexity of these controls, we aimed to have a modular and well-engineered design, optimized for stability and upgradeability. These efforts resulted in the high stability optical and optomechanical designs presented in Section 3.3.2 and Chapter 6.

In parallel, we continued to develop new hardware and upgraded the four-rod apparatus. Our aim was not only to enable us to study intriguing physics with the four-rod apparatus, but also to validate the design, so it could be applied to the next-generation ion trap apparatus. This led to the works presented in Chapters 3, 4 and 5.

Below is a brief outline of the thesis:

1. Chapter 2: This chapter provides a concise overview of the trapped ion quantum information processing platform with $^{171}Yb^{+}$, the ion species used in our lab. We will introduce basic quantum operations and discuss how spin-spin interactions between ions can be generated. We will examine the commonly used transitions of the $^{171}Yb^{+}$ and introduce quantum operations for manipulating the quantum states

of the ions, including Rabi flopping, Raman transitions, and the Mølmer-Sørensen scheme.

2. Chapter 3: This chapter introduces the experimental setup of the four-rod trapped ion apparatus that we used. It includes discussions about the trap design, vacuum system, optics with laser system, and the imaging system. The chapter also includes the recipe to a 0.2NA microscope objective that I designed with all in-stock lenses, which allows the construction of cost-effective but high-performance imaging systems. We will also present an analysis comparing two camera sensor technologies, qualitative CMOS (qCMOS) and electron-multiplying CCD (EM-CCD), and discuss their impact on the fidelity of ion state detection and the scalability of reading out the quantum state of a large number of ions.

3. Chapter 4: We will discuss the design and implementation of the individual addressing system that utilize holographic beam shaping with a digital micromirror device (DMD). We will discuss how we use a single ion as a sensor to characterize the optical aberrations in the system and how we actively correct them down to less than $\lambda/20$ RMS wavefront error at $\lambda = 369$ nm wavelength. This allows us to achieve 10^{-4} level of intensity crosstalk error at the adjacent ions. We measure both the population transfer between the two hyperfine ground states and the decoherence of quantum states of the ions to experimentally characterize the intensity crosstalk. The ultra-low crosstalk error allows us to reset the target ion's quantum state without affecting the adjacent ion with $> 99.9\%$ fidelity. With the assumption of using the current state-of-the-art detector, this crosstalk error translates to the fidelity of $> 99.6\%$ for reading out the target ion's quantum state without affecting the adjacent ion. This low level of crosstalk opens up the possibility of studying new type of physics, for example, measurement-induced phase transitions[16].

4. Chapter 5: In this chapter, we will discuss how we engineer various types of Hamiltonians using arbitrary waveform generators (AWGs). We will also examine how these are used to study emergent conservation laws in a time-dependent, strongly driven, interacting Floquet quantum system. We have experimentally demonstrated that total magnetization can be preserved in a transverse field Ising system with an appropriate Floquet drive. Additionally, we have presented evidence suggesting that the Hilbert space fragments into multiple sectors, each with a different total magnetization, and that dynamics can be confined within each of these sectors.

5. Chapter 6: In this chapter, we will discuss the design of the Raman beam individual addressing system optimized for our next-generation ion trap. The design is crafted

with scalability in mind and can handle a substantial number of ions (30-50 ions). The individual addressing system employs a mirrored optical setup of the acousto-optic deflector (AOD) for the two Raman beams. This enables us to compensate for the site-dependent frequency shift from each individual AOD. Simulations of the optical design demonstrate its capability to achieve sub-10^{-4} level intensity crosstalk error at the adjacent ions. We adopted a modular design approach to separate beam preparation from individual addressing controls. The modules are interconnected with hollow-core photonic crystal fibers. This design choice allows for mode cleaning and simplifies the placement of optical components. The design maintains image telecentricity while using less total beam path than the typical 4-f lens system design. This configuration enables us to minimize coupling to undesired axial modes while retaining a compact footprint for the optical setup.

1.2 Author Contribution

The work presented in this thesis, which includes the results from Chapters 3, 4, 5, and 6, is a product of collaborative effort. The specific contributions from each author are listed at the beginning of each respective chapter.

Chapter 2

Trapped Ion Basics for Quantum Information Processing

This chapter delves into the key principles and fundamental elements of trapped ion systems as tools for quantum information processing. Primarily, our attention will be centered on the $^{171}Yb^{+}$ ion, however, many of the concepts explored here can be adapted for use with other ion species.

We begin by presenting a concise overview of the basics of trapped ion systems, encompassing aspects such as energy levels, laser cooling, state detection, and the ion trap itself. Following this, we'll delve into the tools used for quantum information processing, highlighting how spin manipulation and spin-spin interaction are put into effect within the trapped ion system.

2.1 Overview

In our lab, we utilize $^{171}Yb^{+}$ ions as the qubits for quantum information processing. Its energy levels, lifetime, and corresponding transitions are shown in Fig. 2.1.

The $^{171}Yb^{+}$ ions exhibit four hyperfine ground states of $^{2}S_{1/2}$, namely $|F=0, m_F=0\rangle$, $|F=1, m_F=0\rangle$, $|F=1, m_F=1\rangle$, and $|F=1, m_F=-1\rangle$. Out of these four states, we select $|F=1, m_F=0\rangle$ and $|F=0, m_F=0\rangle$ as the qubit states due to the energy splitting between these two states being insensitive to the first order perturbation in the magnetic fields. This attribute contributes to a prolonged coherence time for the qubit. It has been experimentally demonstrated that $^{171}Yb^{+}$ ions can maintain coherence over hour-long

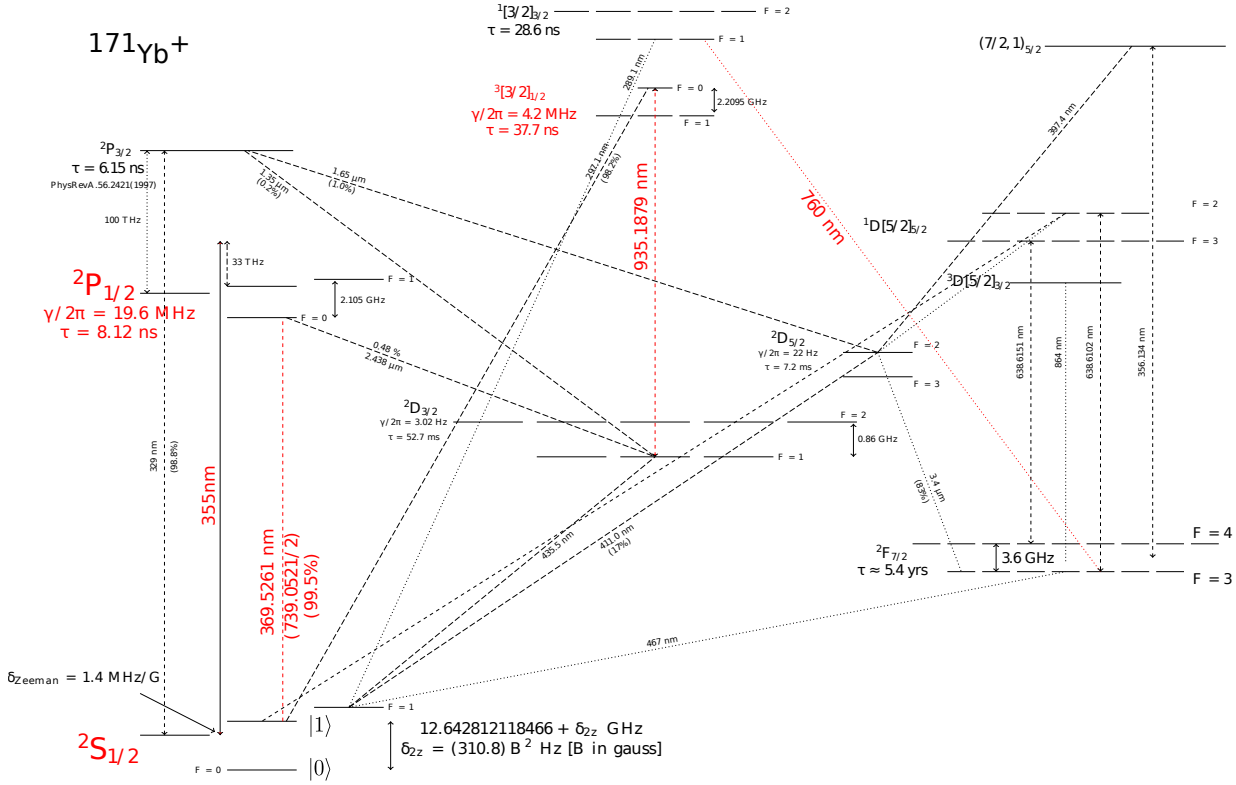

Figure 2.1: Energy level diagram of $^{171}\mathrm{Yb}^{+}$ ions. $|^2S_{1/2}, F = 1, m_F = 0\rangle$ and $|^2S_{1/2}, F = 0, m_F = 0\rangle$ are the two qubit states, and their energy splitting is insensitive to the first-order perturbation in the magnetic field. The 369 nm $^2S_{1/2}$ to $^2P_{1/2}$ is used for state detection (Sec. 2.3), state reset (Sec.2.3), and Doppler cooling (Sec. 2.4.1). The 935 nm and 760 nm beams are the repumping beams bring the ions' state from $^2D_{3/2}$ and $^2F_{7/2}$ respectively back to $^2S_{1/2}$ (Sec. 2.4.2).

durations[68]. For ease of reference throughout this thesis, we will denote $|F = 1, m_F = 0\rangle$ as $|1\rangle$ and $|F = 0, m_F = 0\rangle$ as $|0\rangle$.

In a trapped ion quantum information processor, multiple ions are typically present. These ions are confined inside a vacuum chamber using electrodes that generate direct current (DC) and radio frequency (RF) electric fields. The ions are cooled via lasers to approach their motional ground state. By applying a suitable configuration of DC and RF voltages, the ions can be arranged into a crystallized linear chain. This strategic arrangement forms the foundation for intricate quantum interactions and processing.

With more controllable ions in the system, the trapped ion quantum information process will be more powerful, as it is possible to process the quantum information in a larger Hilbert space. However, increasing the number of ions within the system also escalates its complexity, introducing additional engineering challenges. Therefore, it is crucial to take scalability into account when designing and implementing quantum controls.

2.2 Photo Ionization and Ion Trap

The $^{171}Yb^{+}$ ions are produced by photoionization of neutral Ytterbium atoms. We obtain these neutral atoms by heating solid Ytterbium metal in an atomic oven, which creates vaporized Ytterbium atomic beams. The geometric structure of the atomic oven constrains the direction of the vaporized atomic vapor that can leave the oven. The atoms pass through the center of the ion trap, where they are ionized and subsequently captured. It's worth mentioning that there are alternative methods to the atomic oven approach for generating neutral atomic beams, such as laser ablation on solid metal or oxide[69].

To convert neutral Ytterbium atoms into ions, we employ a two-step photoionization process. First, we use a 399 nm laser to excite the neutral atoms from the $^1S_0$ state to the $^1P_1$ state. Subsequently, another laser excites the electron of the atom from the $^1P_1$ state to the continuum, ejecting the electron from the atom and thus turning the neutral atom into an ion.

The first ionization beam derived from a continuous wave (CW) 399 nm laser is aligned to be perpendicular to the atomic beam to minimize the Doppler shift. By doing so, it allows us to selectively ionize the atoms of a specific isotope from the atomic beam. As for the second ionization beam, there is no specific requirement for the beam pointing. To ensure that a photon of the second ionization has enough energy to bring the electron to the continuum, the wavelength of the second ionization beam needs to be shorter than

394 nm[6]. We typically reuse the existing Doppler cooling beam (later mentioned in Sec. 2.4.1) or the Raman beam (later mentioned in Sec. 2.5.2) as the second ionization beam.

The produced $^{171}Yb^{+}$ is then trapped within the ion trap. The ion trap we utilize is a linear Paul trap[57], constructed with four electrodes. RF voltages are applied to these electrodes to provide radial confinement for the ion chain, while two needles with DC voltages created axial confinement. We do not use DC voltages on all the electrodes due to Earnshaw's theorem[19], which indicates it is impossible to create a static electrical potential minimum in vacuum. It requires non-zero charge distribution at the potential minimum. Consequently, the Paul trap utilizes a time varying saddle potentially to create effective potential for the confinement.

Within the trap, the Columb interactions between the ions have the ions oscillate with different collective modes. We can describe the position of the ith ion $\hat{X}_i$ as

$$\hat{X}_i = \bar{X}_i + \sum_{m=1}^{N} b_{im}\hat{\xi_m} \tag{2.1}$$

in which $\bar{X}_i$ is the equilibrium position of the ith ion. The indices m denotes the normal mode, and $\hat{\xi_m}$ is the displacement of the mth mode. b_{im} is its transformation matrix with the following property[47]:

$$\sum_{m} b_{im}b_{jm} = \delta_{ij} \tag{2.2}$$

$$\sum_{i} b_{im}b_{in} = \delta_{mn} \tag{2.3}$$

For more details about the design of our ion trap and the atomic oven within the system, refer to Kotibhaskar (2019)[35]. Key parameters of the ion trap we use include:

1. RF frequency: We apply an RF frequency of 22 MHz to the trap.
2. DC voltage: We can apply a DC voltage of up to 200V to the needle electrode.
3. Trap Frequency ω_m: In our typical configuration, we can achieve a radial (orthogonal to the ion chain direction) trap frequency of approximately 1.2 MHz and an axial (along the ion chain direction) trap frequency of 200 kHz.

2.3 State Detection

A critical criterion for the use of an internal state as a qubit state is our ability to detect that state. In the context of the trapped ion system, state detection is generally accomplished through the fluorescence emitted by the ion when stimulated by a laser. For $^{171}Yb^{+}$ ions, the fluorescence emanates from the transition between $^2S_{1/2} \rightarrow {}^2P_{1/2}$, specifically the transition from the three $F = 1$ states of $^2S_{1/2}$ to the $^2P_{1/2}$ $|F = 0, m_F = 0\rangle$. As illustrated in Fig. 2.2, this transition forms a cycle, which results in prolonged excitation and continuous fluorescence. In contrast, the $|0\rangle = |F = 0, m_F = 0\rangle$ state is 14.7 GHz off resonance from the laser (coupled to $F = 1$ states of $^2P_{1/2}$. See also in Sec. 2.4.1), implying that the ion in this state has a very low probability of being excited.

Consequently, the fluorescence is extinguished when the ion is in the $|0\rangle$ state. This fluorescence is captured by a detector, and the signal generated can be analyzed to classify the ion's state. A variety of detectors, such as the photon multiplier tube, avalanche photodiode, and camera, are commonly employed, each with its unique characteristics that we will be further examine in Sec. 3.4.2.

Figure 2.3 demonstrates a histogram of the fluorescence signals produced by the ion initialized in both the $|0\rangle$ and $|1\rangle$ states. The signals are measured using a photon multiplier tube (PMT). We can see there is a clear separation of the two distributions, allowing us to discriminate the two states.

Even though the transition used for detection is a cycling transition, there is still a possibility that the ion will off-resonantly couple to other states. The nearest transition (2.1 GHz detuned) is from the $F = 1$ states of $^2S_{1/2}$ to the $F = 1$ states of $^2P_{1/2}$, with a one-third likelihood that the ion will decay to the $|0\rangle$ state upon off-resonant excitation. This off-resonant coupling contributes to a skewed bright state distribution that does not fully conform to a Poisson distribution, showing an increased population at low photon counts. This limits the number of photons that the ion is able to emit during the detection process and leads to the main source of error in state detection.

It's worth noting that a magnetic field is applied to the system to break the degeneracy of the $F = 1$ states of $^2S_{1/2}$ with different m_F quantum number with the Zeeman effect. Since there are more ground states than the excited states in the cycling transition, if there are no mechanism to break the degeneracy, the ions will fall into a linear combination of the ground states that does not interact with the detection beam[4], referred as the coherent dark states. We have the Zeeman splitting to be 6.7 MHz to optimize the bright-dark state detection fidelity.

To enhance the fidelity of state detection, typical strategies involve utilizing an imaging

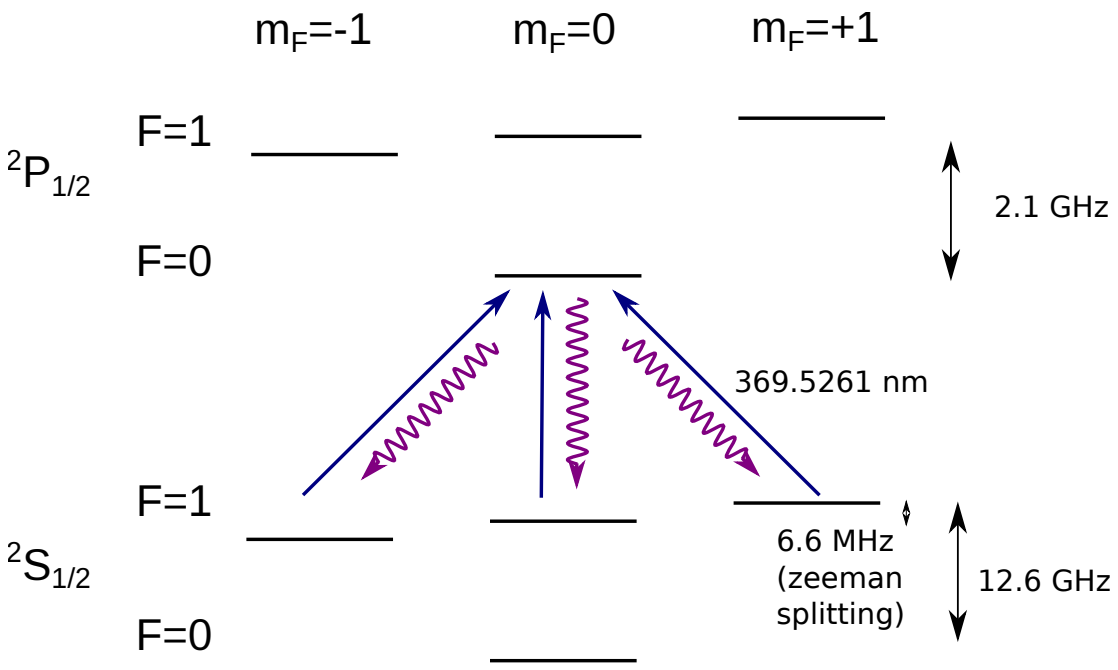

Figure 2.2: Schematic of the state detection process. The Zeeman splitting is controlled by the magnetic field applied. In our lab, we tune the Zeeman splitting to $2\pi \times 6.6$ MHz (1/3 of the natural linewidth γ) to optimize the scattering rate.[4]

system with a larger numerical aperture to gather more photons and deploying a more sensitive detector with lower noise.

2.4 State initialization

The same $^2S_{1/2} \rightarrow {}^2P_{1/2}$ transition can also be used to laser cool the ion and reset the state of the ion. More specifically, we use the transition that couples the $F = 1$ states of $^2S_{1/2}$ to the $F = 1$ states of $^2P_{1/2}$. This same transition off-resonantly pumps the ions to the $|0\rangle$ state during state detection, as explained in Section 2.3.

For state initialization, we employ a laser that resonantly pumps the ion to the $|0\rangle$ state. Such a laser beam can be generated by modulating the laser used in state detection with a $2.1GHz$ Electro-Optic Modulator (EOM). Consequently, one of the sidebands produced by the EOM resonates with the transition. Using an EOM simplifies the experimental setup, eliminating the need for an additional laser. However, the EOM is incapable of depleting the laser at the state detection frequency, which may be undesirable in some cases. For instance, if we wish to selectively reset one ion without affecting others, the undepleted laser at the detection frequency can introduce errors by collapsing the states of the remaining ions in the system. Further discussion on this issue is presented in a later chapter (see Chapter 4).

Fig. 2.4 illustrates the decay of the fluorescence signal throughout the optical pumping process. As the times goes by, the ion is pumped to the $|0\rangle$ state, resulting in the reduction of the fluorescence signal. The characteristic decay time, known as the "optical pumping time", is typically in the order of a few microseconds.

2.4.1 Doppler Cooling

As mentioned in the previous section, the $^2S_{1/2} \rightarrow {}^2P_{1/2}$ transition is also used for laser cooling. To use the laser to cool the ion, we red-detune the light from the transition. When the ion is moving towards the laser, the Doppler shift will bring the ion closer to resonance, resulting in a higher scattering rate. On the other hand, when the ion is moving away from the laser, the Doppler shift will bring the ion further away from resonance, resulting in a lower scattering rate. This way, the ion will scatter more photons when its momentum is opposite to the direction the laser beam is pointing, and hence the ion's kinetic energy will be reduced. This process is called Doppler cooling, as it uses the Doppler shift to cool the ion.

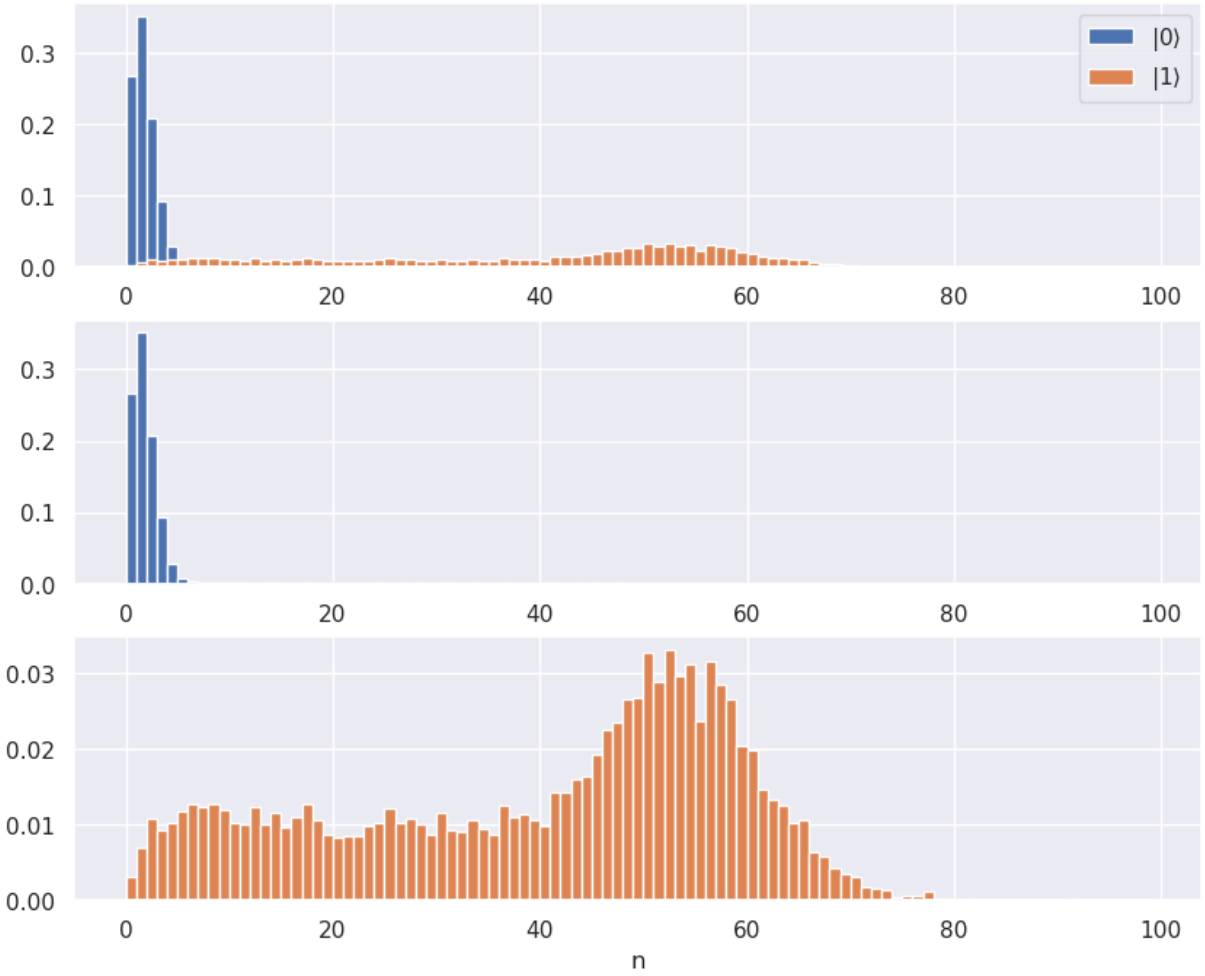

Figure 2.3: Histogram of the fluorescence signals produced by the ion initialized in both the $|0\rangle$ and $|1\rangle$ states. The signals are measured using a photon multiplier tube (PMT). The y-axis is normalized probability (occurrence divided by total number of shots) The detection time is set to be 1.5 ms. The intensity of the detection beam is $I \approx 0.9 I_{sat}$.

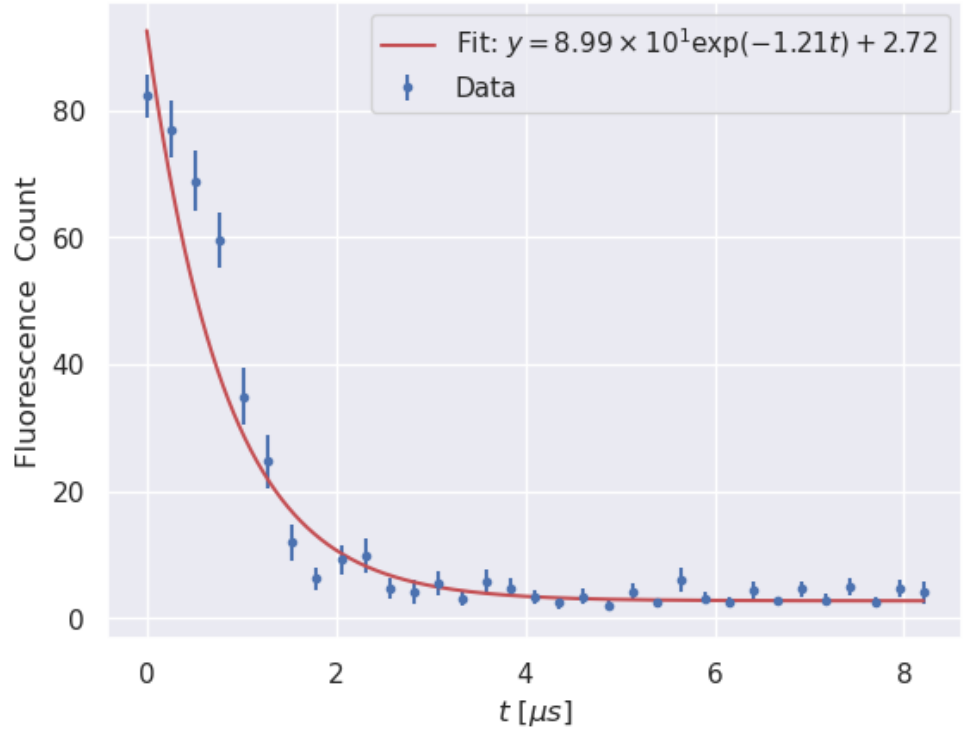

Figure 2.4: Fluorescence signal decay during optical pumping. The ion is initialized in the $|1\rangle$ state and pumped to the $|0\rangle$ state. The characteristic decay time is $(1/1.21)\mu$s $= 0.826\mu$s. Each ion has an average of about 40 counts in its bright state $|1\rangle$ as described in Fig. 2.3. The fluorescence signal measured here are from two ions both initialized in the $|1\rangle$ state.

From an observer's perspective in the lab, the ion absorbs a lower-energy photon (red-detuned) and emits a higher-energy photon. Since energy is conserved, the ion will lose its kinetic energy and consequently cool down.

We need a method to pump the ion out of the $|0\rangle$ state. We can achieve this by driving the transitions between the $|0\rangle$ and the $F = 1$ states of $^2P_{1/2}$. This transition is 14.7 GHz (2.1 GHz + 12.6 GHz) higher than the detection transition. In our lab, we use a 14.7 GHz EOM (See Sec. 3.3.1 for the part number and the implementation details) to modulate the cooling beam, creating a sideband at a few percents level to drive the transition.

Doppler cooling can theoretically cool the ion down to about 480 μK[67]. This temperature corresponds to the uncertainty in the photon's frequency, which relates to a

distribution of momentum kicks on the ion. Recoil heating is caused by the spontaneous emission of the photons. This limit is known as the Doppler limit T_{Doppler}.

$$T_{\text{Doppler}} = \frac{\hbar\gamma}{2k_b} \tag{2.4}$$

where γ is the linewidth of the transition, and k_b is the Boltzmann constant. The linewidth of the ${}^2S_{1/2} \rightarrow {}^2P_{1/2}$ transition is about $2\pi \times 19.6$ MHz. In our lab, the temperature after applying Doppler cooling for 1.5 ms is typically around $2.5T_{\text{Doppler}}$[67], which is close to the Doppler limit.

2.4.2 Repumping

There's about a 0.48% chance that an ion will decay to the ${}^2D_{3/2}$ state from the ${}^2P_{1/2}$ state. Without an additional mechanism to pump the ion out of the ${}^2D_{3/2}$ state, it would take about 52.7 ms[71] for the ion to decay back to the ${}^2S_{1/2}$ state. This hinders efficient cooling of the ion and limits the number of scattered photons. In addition, ions can be transferred from the ${}^2D_{3/2}$ state to the ${}^2F_{7/2}$ state, which has a year-long lifetime[38], through collisions with residual background gas in the chamber[38].

To address these issues, we use both 369 nm and 935 nm lasers, as well as a 760 nm laser, to optically pump the ion back to the ${}^2S_{1/2}$ state. The 935 nm laser drives the transition from the ${}^2D_{3/2}$ state to the ${}^3[3/2]_{1/2}$ state, which decays to the ${}^2S_{1/2}$ states with a characteristic time of 37.7 ns[3]. The 760 nm laser is used to drive the transition from the ${}^2F_{7/2}$ state to the ${}^3[3/2]_{1/2}$ state, which then decays to the ${}^2S_{1/2}$ state[38].

To account for the hyperfine splitting, we use a fiber-EOM (Sec. 3.3.1) to generate the necessary sidebands for the 935 nm beam. As for the 760 nm laser, the event of falling into the ${}^2F_{7/2}$ states is rare. Therefore, instead of using an EOM, we simply scan the laser frequency from one hyperfine state to the other in a few seconds timescale to cover the hyperfine transitions.

2.5 Toolbox for quantum information processing

In this section, we will discuss some important tools for engineering quantum operations, including spin manipulation and spin-spin interactions.

2.5.1 Global Qubit Rotation through Microwave

The first tool we will talk about is the microwave. Essentially, the microwave drive the Rabi flopping between the $|0\rangle$ and $|1\rangle$ states. The Rabi frequency is proportional to the amplitude of the microwave (square root of the power).

In our experimental setup, we employ a microwave source, mixing its output with an RF frequency at approximately 85 MHz from a direct-digital synthesizer (DDS). The mixed signal then passes through a band pass filter to eliminate the frequency components resulting from mixing. The filtered signal is subsequently amplified by a microwave amplifier and transmitted to the trap via a microwave horn.

In Figure 2.5, we display the ion's fluorescence signal when we apply microwave pulses of varying duration. Depending on the pulse length, the ion's state will oscillate between $|0\rangle$ and $|1\rangle$ (Rabi oscillations), leading to an oscillating fluorescence signal.

However, due to microwaves' long-wavelength nature, they are incapable of individually addressing each ion without the aid of specially designed antennas and chips. Hence, microwaves are only employed for global qubit rotation. Furthermore, microwaves are unable to generate sufficient spin-phonon coupling to facilitate phonon-mediated spin-spin interactions. Therefore, we do not use microwaves to establish spin-spin interactions.

Although the utility of microwaves in quantum control engineering is limited, their simplicity and high coherence make them an ideal tool for system characterization and diagnostics. For instance, we can use microwaves to measure the qubit coherence time with Ramsey spectroscopy, a topic we will explore in section 4.5.

2.5.2 Coherent Quantum Operation with Raman Transition

Instead of a single microwave field, we can use two Raman beams to drive the $|0\rangle \leftrightarrow |1\rangle$ transitions as illustrated in Fig. 2.6. The Raman transition is a two-photon process, where the two beams are detuned from the direct transition. The frequency difference between the two beams is equal to the energy difference between $|1\rangle$ and $|0\rangle$, allowing the beat note of the two beams to drive the transition. The two-photon Rabi frequency of the Raman transition is given by

$$\Omega_i = \frac{g_1^i g_2^i}{2\Delta} \tag{2.5}$$

where g_1^i and g_2^i are the direct Rabi frequency of the two beams of the ith ion, Δ is the detuning of the two beams from the direct transition.

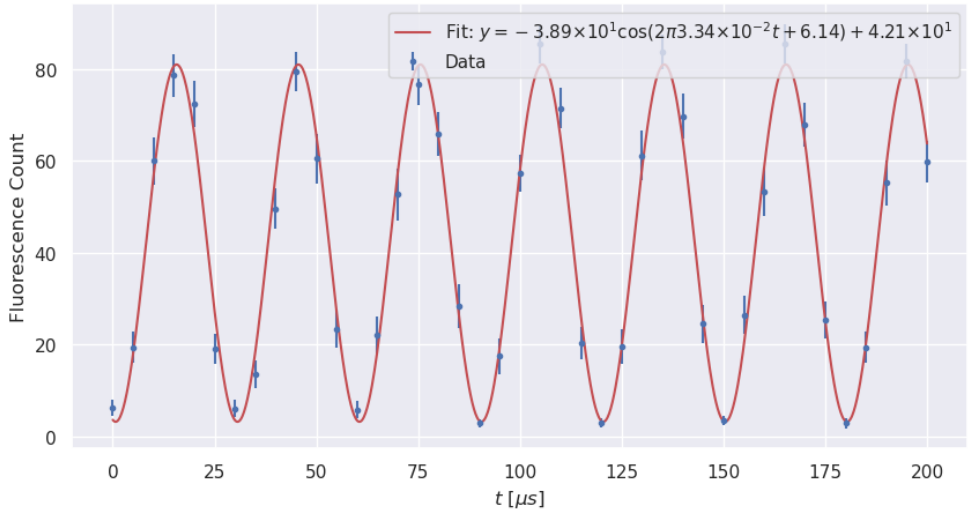

Figure 2.5: Fluorescence signal of the ion when we apply microwave pulses of varying duration. There are two ions, and the ions' are both initialized to $|0\rangle$ state. The microwave pulse is applied at $t = 0$. The fluorescence signal is recorded by the PMT.

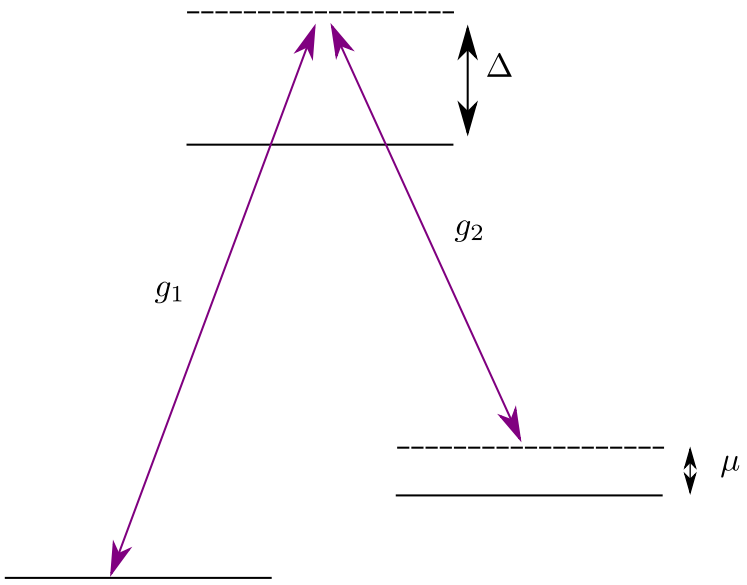

Figure 2.6: Illustration of the Raman transition. g_1 and g_2 are the Rabi frequency of the two Raman beams. Δ is the detuning of the two beams from the direct transition. μ

With rotating wave approximation (RWA), the atom light interaction Hamiltonian can be written as (Here we have $\hbar = 1$ for simplicity)

$$H(t) = \frac{1}{2}\sum_i \left[\Omega_i \left(\sigma_+^i e^{i(\delta k \hat{X}_i - \mu_i t - \delta\phi_i)} + \sigma_-^i e^{-i(\delta k \hat{X}_i - \mu_i t - \delta\phi_i)}\right) + d_i \sigma_z^i\right]. \tag{2.6}$$

in which Ω_i is the Rabi frequency we just mentioned in Eq. 2.5 of the ith ion, δk is the wave vector difference between the two Raman beams, a.k.a. the wave vector of the optical beat note, and $\hat{X}_i$ is the position of the ith ion.

On the other hand, μ_i is the detuning of Raman transition as shown in the Figure 2.6. $\delta\phi_i$ is the phase difference between the two Raman beams, and d_i is the strength of the AC Stark shift of the ith ion.

As for the polarization and magnetic field requirements, the two Raman beams need to satisfy certain polarization conditions. For instance, as shown in Fig. 2.7, if we want to drive the $|0\rangle \leftrightarrow |1\rangle$ transition, the two Raman beams need to have either σ^+ or σ^- polarization (relative to the quantization defined by the magnetic field). Since there are no common excited states with $m_F = 0$ for $|0\rangle$ and $|1\rangle$, π polarization cannot be used here. A common choice of polarization is $\sigma^+ + \sigma^-$ and $\sigma^+ - \sigma^-$. The sign difference between σ^+ and σ^- in the two beams is used to match the Clebsch-Gordan coefficient of the transition. The exact configuration we used can be found in Sec. 5.3.

Engineering Transverse Field

For the resonant Raman transition ($\mu_i = 0$, $d_i = 0$), we can deduce the atom-light interaction Hamiltonian (Eq. 2.6) as follows:

$$H_B = \frac{1}{2}\sum_i \Omega_i \sigma_{\beta_i}^i, \tag{2.7}$$

In this equation, the transverse field spin operator $\sigma_{\beta_i}^i$ is defined by

$$\sigma_{\beta_i}^i \equiv \sigma_+^i e^{-i\beta_i} + \sigma_-^i e^{i\beta_i} = \sigma_x^i \cos\beta_i + \sigma_y^i \sin\beta_i. \tag{2.8}$$

$$\beta_i = \delta\phi_i - \delta k \bar{X}_i \tag{2.9}$$

This assumes the trap frequency is greater than the Rabi frequency of the Raman transition $\omega_m \gg \Omega_i$. In this case, we can apply the time-average approximation to eliminate fast-oscillating terms in the ion position $\hat{X}_i$, replacing it with its time average $\bar{X}_i$.

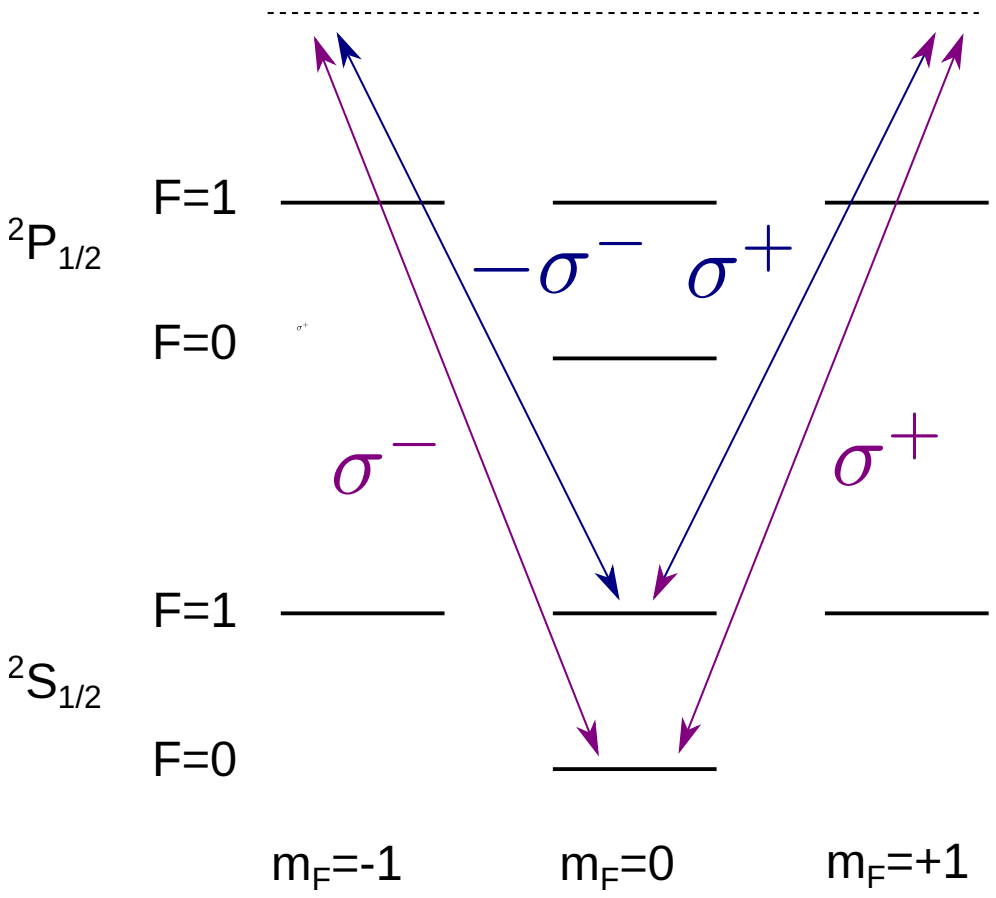

Figure 2.7: Illustration of the Raman transition coupling $|0\rangle$ and $|1\rangle$. The purple and the blue arrows indicate the field of the two Raman beams respectively. Note that the two beams have linear polarization orthogonal to each others, and thus their components in σ^- circular polarization has a sign/phase difference.

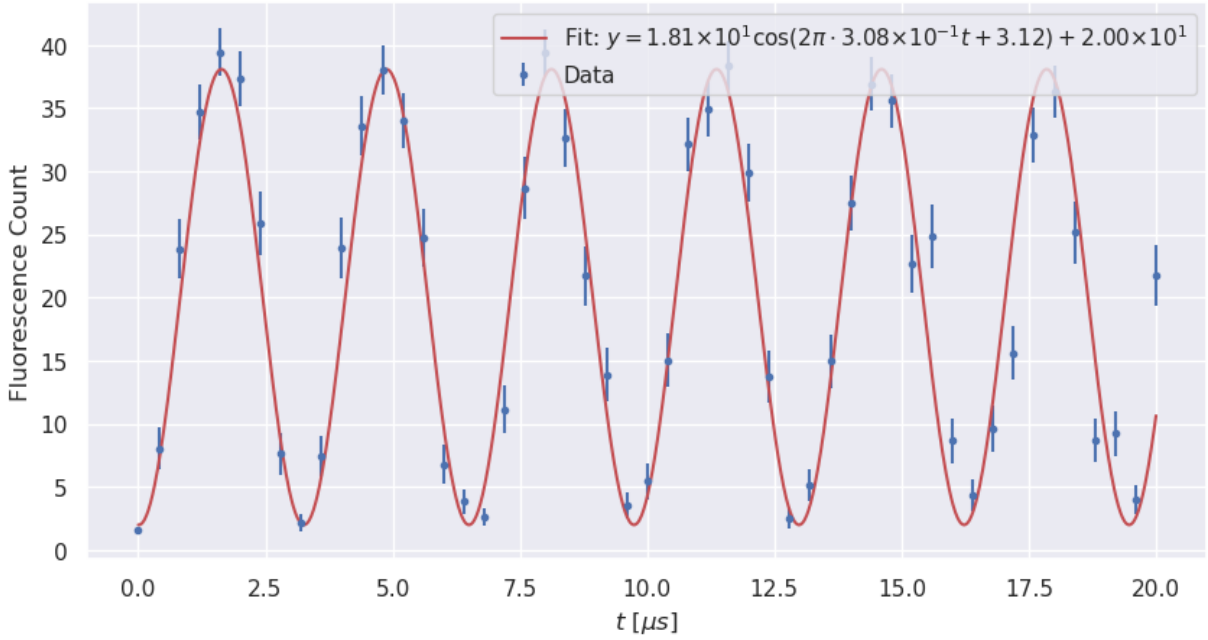

Figure 2.8: Fluorescence signal of the ion when we apply Raman pulses of varying duration. The ion is initialized to $|0\rangle$ state. The Raman pulse is applied at $t = 0$. The fluorescence signal is recorded by the PMT. The time for flopping the ion from $|0\rangle$ to $|1\rangle$ is about $\frac{1}{0.309\text{MHz}} \div 2 = 1.6$ μs. The error bars indicate the standard error. The power of both of the two Raman beams are about 400 mW and the beam has $5\mu\text{m} \times 70\mu\text{m}$ $1/e^2$ beam waists (See also Sec. 3.5.1). The laser is at 355 nm and with 15 ps pulse width and 80 MHz repetition rate.

Using the resonant Raman transition, we can engineer an effective magnetic field in the xy plane of the Bloch sphere for the spin model. The direction of this effective magnetic field is determined by the phase difference between the two Raman beams, the average position of the ion, and the wave vector of the beat note. However, the average position and the wave vector of the beat note are generally fixed by the experimental setup and typically can't be altered during the experiment. Hence, we utilize the phase difference between the two Raman beams as our controllable degree of freedom to determine the orientation of the effective magnetic field.

Fig. 2.8 shows the Rabi flopping driven by the resonant Raman transition. This behavior is similar to the flopping driven by the microwave (shown in Fig. 2.5 and discussed in Section 2.5.1), with the ion oscillating between the two qubit states, $|0\rangle$ and $|1\rangle$.

Spin-Phonon Coupling and Raman Sideband Cooling

The Raman transition can not only couple purely between spin states, but also to states with differing phonon numbers. To derive the spin-phonon coupling, we start from the Hamiltonian of the light matter interaction in Eq. 2.6 and expand the ion position operator $\hat{X}_i$ in terms of the phonon creation $a_m^\dagger$ and annihilation a_m operators:

$$\hat{\xi_m} = \xi_m^{(0)}(a_m^\dagger e^{i\omega_m t} + a_m e^{-i\omega_m t}) \tag{2.10}$$

$$\xi_m^{(0)} = \sqrt{\frac{\hbar}{2m\omega_m}} \tag{2.11}$$

where ω_m is the frequency of mode m. This leads to the following expression for the operator of the ion's position in terms of the phonon operators and the transformation matrix b_{im} (see also previously in Eq. 2.3):

$$\hat{X}_i = \bar{X}_i + \sum_{m=1}^{N} b_{im}\xi_m^{(0)}(a_m^\dagger e^{i\omega_m t} + a_m e^{-i\omega_m t}) \tag{2.12}$$

Plugging this into the light-matter interaction Hamiltonian in Eq. 2.6, we obtain

$$H(t) = \frac{1}{2}\sum_i \left[\Omega_i \left(\sigma_+^i e^{-i\beta_i} e^{i\sum_m \eta_{im}(a_m^\dagger e^{-i(\mu_i-\omega_m)t} + a_m e^{i(\mu_i-\omega_m)t})} + \text{h.c.}\right) + d_i\sigma_z^i\right] \tag{2.13}$$

where $\eta_{im} = \delta k b_{im}\xi_m^{(0)}$ is the Lamb-Dicke parameter which characterizes the strength of the coupling between the ion i and the phonon mode m. In the Lamb-Dicke regime, where $\eta_{im} \ll 1$, we can expand the exponential term in the Hamiltonian to the first order of η_{im}:

$$H(t) = \frac{1}{2}\sum_i \Omega_i \left[\sigma_+^i e^{-i\beta_i} e^{-i\mu_i t} + \text{h.c.}\right] + \tag{2.14}$$

$$\frac{1}{2}\sum_{im} \Omega_i \left[\eta_{im}\sigma_+^i e^{-i\beta_i}(a_m^\dagger e^{-i(\mu_i-\omega_m)t} + a_m e^{-i(\mu_i+\omega_m)t}) + \text{h.c.}\right] + \tag{2.15}$$

$$\frac{1}{2}\sum_i d_i\sigma_z^i \tag{2.16}$$

The first term (Eq. 2.14) relates to the carrier transition, which aligns with Eq. 2.7 when we impose the resonance condition $\mu_i = 0$ and discard the rapidly oscillating terms. The second term (Eq. 2.15) corresponds to the sideband transition, which introduces coupling between the spin states and the phonon states.

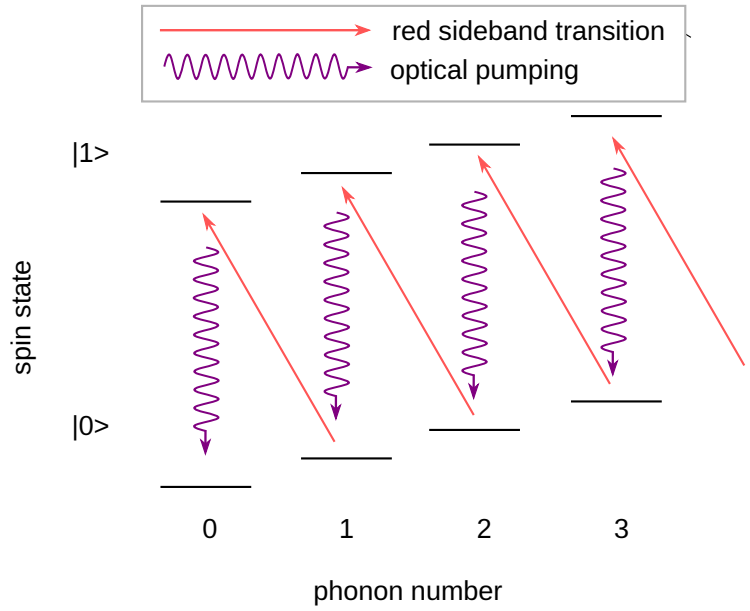

Figure 2.9: Illustration of the Raman sideband cooling.

Depending on the detuning of the Raman transition μ_i from the phonon frequency ω_m, we can further differentiate the sideband transition into blue sideband transitions ($\mu_i = \omega_m$) and red sideband transitions ($\mu_i = -\omega_m$). This detuning determines the pairing between the spin and phonon operators, as one exponential term in Eq. 2.15 becomes 1 while the other term becomes a fast oscillating term and thus is dropped with the approximation. For the blue sideband transition, the raising spin operator σ_+^i pairs with the phonon creation operator $a_m^\dagger$, while for the red sideband transition, it pairs with the phonon annihilation operator a_m. This configuration is achieved once the rapidly oscillating terms with the other phonon operator are eliminated.

The spin-phonon interaction allows us to drive sideband transitions to increase or decrease the phonon number. The blue sideband transition couples the $|0\rangle$ state with a lower photon number to the $|1\rangle$ state with a higher phonon number ($|0\rangle |n\rangle_m \leftrightarrow |1\rangle |n+1\rangle_m$). Conversely, the red sideband transition couples the $|0\rangle$ state with a higher photon number to the $|1\rangle$ state with a lower phonon number ($|0\rangle |n\rangle_m \leftrightarrow |1\rangle |n-1\rangle_m$).

Given the presence of the phonon number operator in the Hamiltonian, the Rabi frequency for the sideband transitions depends on the phonon number. The Rabi frequency of blue sideband transition is $\Omega_i^{bsb} = \Omega_i \eta_{im} \sqrt{n+1}$, while that of the red sideband transition is $\Omega_i^{rsb} = \Omega_i \eta_{im} \sqrt{n}$.

Combining the spin reset mentioned in section 2.4, we can use the red sideband transition to cool the ions' motion to the ground state in a process known as Raman sideband cooling. As illustrated in Fig. 2.9, the ion is initially in the $|1\rangle |n\rangle_m$ state. The Raman transition drives the ion to the $|0\rangle |n-1\rangle_m$ state. The ion is then optically pumped back to the $|1\rangle$ state, and the phonon number remains at $n-1$. Repeating this process eventually reduces the ion's phonon number to zero.

The ions after Doppler cooling has the phonon number distribution follows a thermal distribution. In practice, we apply the red sideband Raman transition and an optical pumping beam with its characteristic time close to the timescale of the red sideband Rabi frequency simultaneously to continuously cool the ions.

Although Raman sideband cooling can cool ions down to their motional ground state and below the Doppler limit, it is not as efficient as Doppler cooling, as the Raman transition is a second-order process, and we have our ions under the Lamb-Dicke regime of which transitions with more than one phonon number are strongly suppressed. Therefore, we typically use Doppler cooling to cool the ions to a temperature close to its limit, then use Raman sideband cooling to further cool the ions to their motional ground state.

2.5.3 Engineering Spin-Spin Interaction through Mølmer-Søresen Scheme

We show that the spin-phonon interaction can be created through the Raman transition. This interaction also allows us to engineer spin-spin interactions between ions using phonon modes as buses to connect the ions.

The most commonly used scheme to engineer spin-spin interactions is the Mølmer-Søresen scheme [64]. In the Mølmer-Søresen scheme, we use a pair of the Raman beat notes that are symmetrically detuned from the carrier frequency but not resonantly driving the sideband transition. With rotating wave approximation, we can rewrite the spin-phonon interaction term of the Hamiltonian in Eq. 2.15 as

$$H(t) = \frac{1}{2} \sum_{i,m} \eta_{im} \Omega_i \sigma^i_{\theta_i} \left[a^\dagger_m e^{-i(\delta_{im} t + \psi_i)} + a_m e^{i(\delta_{im} t + \psi_i)} \right]. \tag{2.17}$$

where $\delta_{im} = \mu_i - \omega_m$ is the detuning of the Raman beat note from the phonon frequency. The two phase terms θ_i and ψ are referred as the spin phase and the motional phase. The spin phase θ_i determines the orientation of the spin operator in the XY plane, while the motional phase ψ_i determines the phase of the spin-phonon coupling, but it does not affect the spin-spin interaction.

Depending on whether the bichromatic beat notes are copropagating or counterpropagating, the spin phase and the motional phase have different configurations. We refer to them as phase-sensitive and phase-insensitive configurations respectively.

Phase sensitive configuration (copropagating beat notes)

$$\theta_i = \left(\frac{\delta\phi_{i+} + \delta\phi_{i-}}{2}\right) - \delta k \bar{X}_i - \frac{\pi}{2} \tag{2.18}$$

$$\psi_i = \left(\frac{\delta\phi_{i+} - \delta\phi_{i-}}{2}\right) \tag{2.19}$$

Phase insensitive configuration (counterpropagating beat notes)

$$\theta_i = \left(\frac{\delta\phi_{i+} + \delta\phi_{i-}}{2}\right) \tag{2.20}$$

$$\psi_i = \left(\frac{\delta\phi_{i+} - \delta\phi_{i-}}{2}\right) - \delta k \bar{X}_i - \frac{\pi}{2} \tag{2.21}$$

Here, ϕ_{i+} and ϕ_{i-} denote the phase of the two Raman beat notes on the ith ion.

As we can see, the main difference between the two configurations is the dependencies of the ion position $\bar{X}_i$ on the spin phase and the motional phase. In the phase sensitive configuration, the spin phase is more susceptible to drifts in the ion position and may have shorter coherence time. However, this configuration makes referring the phase to the rest of the Hamiltonian easier. As we can see in Eq. 2.7, the phase of the spin operator of the transverse effective magnetic field also have the $-\delta k \bar{X}_i$ term.

Regardless the configuration, it can be shown that for beat note frequency is far from the normal mode ($|\delta_{im} \gg \eta_{im}\Omega_i|$), it only virtually excite the phonons, and the spin-photon interaction is negligible. The effective Hamiltonian becomes

$$H_{J_\theta} = \sum_{i<j} J_{ij} \sigma^i_{\theta_i} \sigma^j_{\theta_j}, \tag{2.22}$$

where the spin-spin interaction matrix J_{ij} is given by

$$J_{ij} = \Omega_i \Omega_j \omega_{\text{rec}} \sum_m \frac{b_{im} b_{jm}}{4\omega_m} \left(\frac{1}{\delta_{im}} + \frac{1}{\delta_{jm}}\right) \tag{2.23}$$

$$= \Omega_i \Omega_j \omega_{\text{rec}} \sum_m \frac{b_{im} b_{jm}}{2\omega_m \delta_m} \text{ for } \delta_{im} = \delta_m. \tag{2.24}$$

$$\omega_{\text{rec}} = \frac{\hbar(\delta k)^2}{2M} \tag{2.25}$$

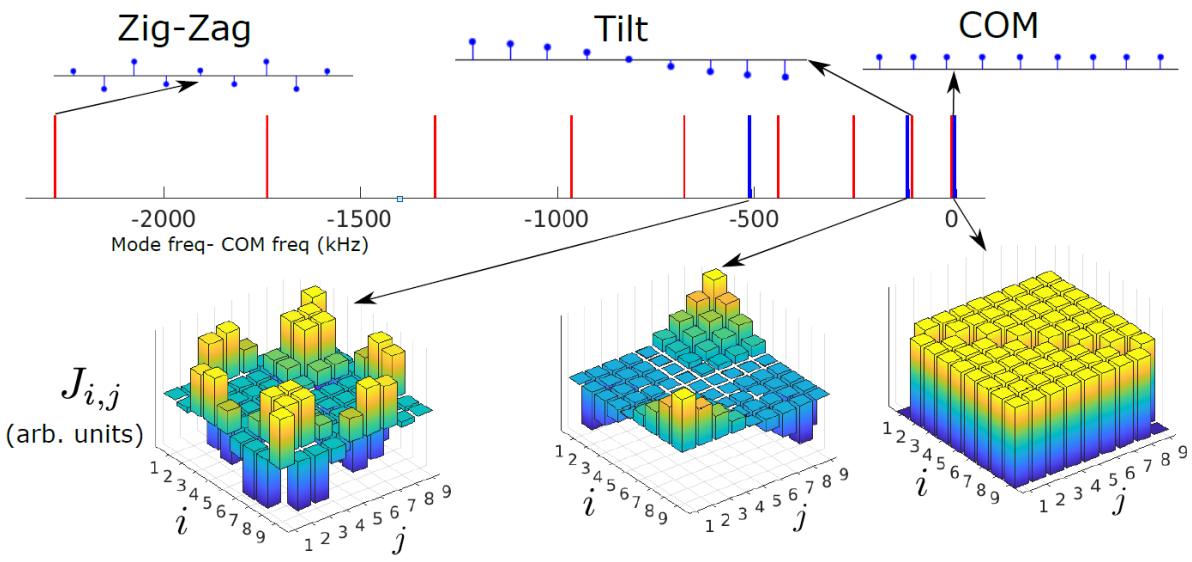

Figure 2.10: Examples of spin-spin interaction matrix J_{ij} with various Mølmer-Søresen detuning

In Fig. 2.10, we show a few examples of the mode vector b_{im}, and how the interaction matrix J_{ij} looks like by parking the Mølmer-Søresen detuning μ at different frequency.

2.6 Conclusion

In this chapter, we have given a concise overview of some important concepts of $^{171}Yb^{+}$ quantum information processor. We also discuss various techniques to manipulate the qubits state that will be used in the later chapters. In particular, we will discuss more details about the implementation of the Raman transition and the Mølmer Søresen scheme in chapter 5 and 6. As for the qubit initialization and readout, we will discuss their implementation at the individual ion level in chapter 4.

Chapter 3

The Four Rod Apparatus

In this chapter, we will introduce the experimental apparatus used throughout most parts of the thesis. The apparatus is a four-rod linear Paul trap. We will discuss the trap design, vacuum system, optics with laser system, and the imaging system.

I participated in the building process of the apparatus presented in this chapter, mostly on the optical systems and control systems. The work showcased here is a collaborative effort with other members of the lab, including Nikhil Kotibhaskar, Sainath Motlakunta, Anthony Vogliano, Lewis Hahn, Jingwen Zhu, Roland Hablutzel, Manas Sajjan, and Rajibul Islam. Of particular note, I spearheaded the design of the imaging system and the laser and optical system.

3.1 Overview

In Fig. 3.1, we present a concise overview of the ion trap and the vacuum system. The ion trap is housed inside an ultra-high vacuum (UHV) system, equipped with an ion pump and a getter pump, which enables us to achieve a vacuum level of 10^{-11} mbar.

The top and bottom view ports provide higher optical access (0.3 NA) to the ion, accommodating our imaging system and individual addressing system. Conversely, the side view ports, which have relatively lower optical access (0.1 NA), are connected to our global beam system. This includes cooling, detection, optical pumping (spin reset), repumping, first-ionization, and Raman beams. Notably, the global cooling, detection, optical pumping, and repumping beams are combined and delivered to the chamber through a fiber.

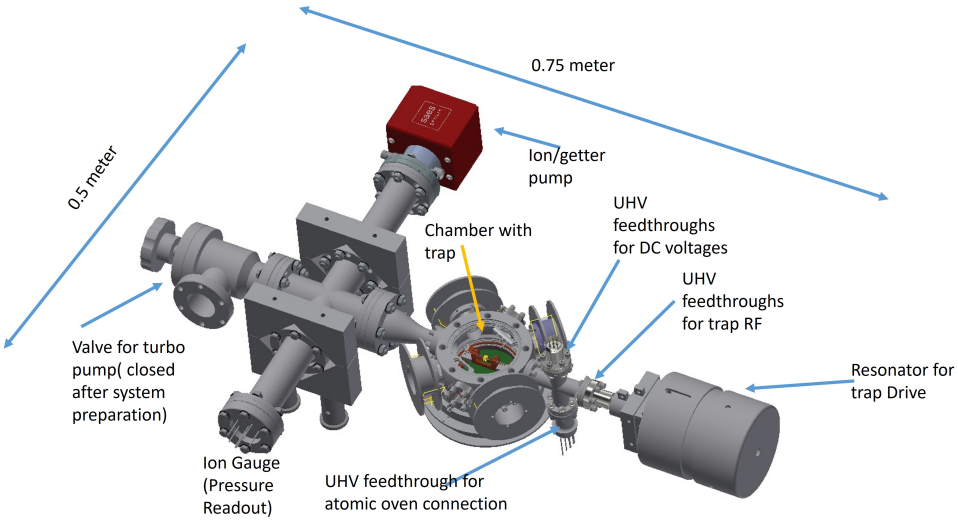

Figure 3.1: Overview of the experimental apparatus.

Fig. 3.2 shows the cross-section of the vacuum chamber as viewed from the top, alongside the layout of the beams and their respective entry points into the chamber. We use dichroic beam splitters at the exit view port of the two Raman beams to separate them from the beams entering from the other side of the vacuum chamber and redirect the Raman beams to a beam dump. As for the individual spin reset or detection beams, they enter the chamber from the top view port. We have an additional set of imaging systems below the chamber that allows us to monitor the ion and the individual addressing beams simultaneously.

3.1.1 Outline

1. Section 3.2: We will introduce the ion trap we used and relevant trapping parameters.

2. Section 3.3: We will introduce the optics for preparing cooling, detection, and optical pumping beams. We will also present our works on designing high stability optical mechanics.

3. Section 3.4: We will introduce the imaging system we designed along with a custom microscope objective I design. We will also present our analysis on detector technologies of photomultiplier tubes, qualitative CMOS, and electron-multiplying CCD, and how their noise profiles affect the ion state detection.

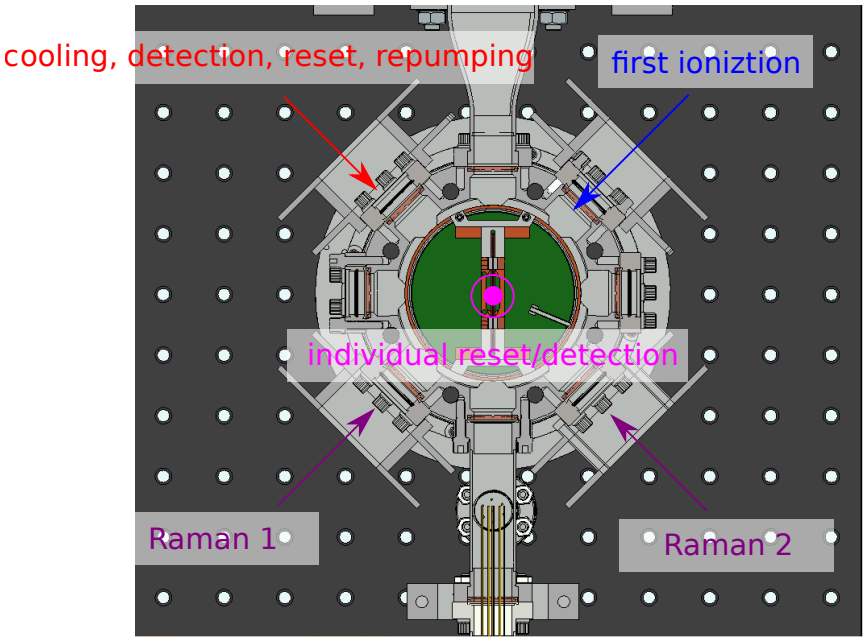

Figure 3.2: Overview of the beams. The individual reset and detection beams are delivered from the top viewport (entering the surface of the page), while the rest of the beams are delivered from the side viewport. The beams are overlaid on the technical drawings of the cross-section of the vacuum chamber and the ion trap.

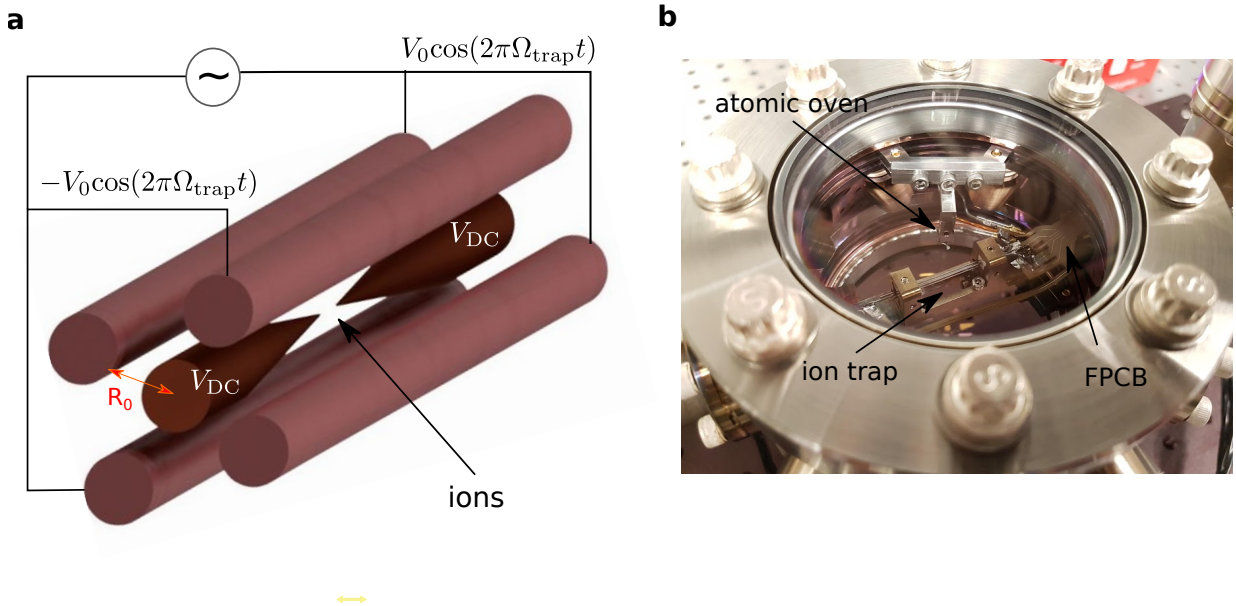

Figure 3.3: **a.** Schematic and Images of the ion trap. The ion trap is a linear Paul trap. It consists of four rod electrodes and two needle electrodes. **b.** The picture of the ion trap in the vacuum chamber. The picture is taken from the top viewport. Along with the trap, an atomic oven for dispensing neutral Ytterbium atoms and the flexible printed circuit board (FPCB) for routing the RF and DC voltages from the feedthroughs to the trap are also shown.

.

4. Section 3.5: We will introduce the Raman optics and the RF system for beat note locking and waveform generation.

3.2 Ion Trap

Fig. 3.3 presents both a schematic and an actual image of the ion trap. We employ a linear Paul trap, consisting of four rod electrodes and two needle electrodes. These electrodes are made from electro-polished tungsten rods. The needle electrodes were fabricated using electrochemical etching, and the detailed recipe can be found in Kotibhaskar et al. (2023)[36].

The rod electrodes are supplied with both DC and RF voltages. The RF voltages provide radial confinement of the ions by creating a pseudo potential, while the DC voltages

fine-tune the position of the ions. The DC voltages supplied to the needle electrodes are used to create axial confinement.

The DC voltage is generated and controlled by a microcontroller chip, ATSAMN16C from Microchip. This is an ARM Cortex M4 microcontroller that operates at 100 MHz, featuring a 10-bit DAC and 16-channel 12-bit ADC. We employ the DAC to generate the DC voltage and the ADC to monitor it. For the rod electrodes, an operational amplifier boosts the maximum peak-to-peak voltage to 6 V, while a high voltage amplifier increases the maximum peak-to-peak voltage to between 0 V and 350 V for the needle electrodes.

The RF voltages are generated by a direct digital synthesizer (RIGOL DG4102) at 22 MHz. These voltages are then amplified by a water-cooled RF amplifier (MPA-40-40 from Centric RF), and passed through a copper helical resonator for further voltage amplification and impedance matching for the trap. Additional details on the resonator design can be found in Kotibhaskar (2019)[35].

Both DC and RF voltages are connected through vacuum feedthroughs. From the feedthrough to the trap electrodes, we use a flexible printed circuit board (FPCB) for electrical connections. The FPCB also features bias-T circuits to combine the RF and DC voltages for the rod electrodes.

The trap is typically operated at about 125 V for the needle DC voltages and with a $V_0 \approx 200$ V amplitude for the RF voltages on the trap. This results in approximately a 1.1 MHz radial trap frequency and a 200 kHz axial trap frequency.

3.3 Cooling, Detection, and Optical Pumping Beam

We combine the cooling, detection, and repumping beams into a single mode photonic crystal fiber (LMA-PM-10 from NKT Photonics) and deliver the beam to the chamber. Instead of using conventional collimators or lenses to collimate and then focus the light onto the ion, we employ parabolic reflectors. This is due to the fact that the use of glass lenses introduces chromatic focal shifts to the beam, preventing different beams from focusing simultaneously onto the ion. In contrast, parabolic reflectors use reflection to collimate and focus the beam, ensuring that its focus is independent of the light's wavelength.

Specifically, we use Thorlabs' RC04FC-F01 (RFL = 15 mm) to collimate the beam and MPD169-F01 (RFL = 152.4 mm) to focus the beam. This results in approximately a tenfold magnification from the fiber tip to the focus spot on the ion, yielding a beam waist diameter of about 90 mm.

3.3.1 Beam Preparation

Shown in the Fig. 3.4 is the schematic of the optical setup of how we modulate the laser to prepare individual beams. The 369 nm laser is first modulated by an acousto-optic modulator (AOM). The first-order beam is used for detection and optical pumping, and an EOM (EO-T2100M3-VIS from Qubig GmbH) is used to create 2.1 GHz side band for generating optical pumping frequency. We switch the RF of the EOM to switch between the detection and optical pumping beams. When the detection/optical pumping AOM is off, the unmodulated beam is used for creating cooling beam. We employ a 14.7 GHz EOM (EO-WG14.7M2-VIS from Qubig GmbH) to create a necessary sideband for pumping the ion out of the dark state $|0\rangle$ (Sec. 2.4.1), so the cooling process can continue. The cooling beam also has an AOM (ASM-200B8 from IntraAction) for power switching and amplitude control. The frequencies of the two AOM is set such that the cooling beam frequency is 30 MHz lower than the detection frequency.

The cooling beam and the detection/pumping beams are combined with a polarization beam splitter, and the combined 369 nm beams are subsequently combined with the repumping beams (935 nm and 760 nm) with a dichroic mirror. The combined beam is then coupled into the photonic crystal fiber and delivered to the chamber.

Note that we use a 3.1 GHz fiber EOM (NIR-MPX950-LN-05-P-P-FA-FA from iXblue) to modulate the 935 nm beam for covering the hyperfine splitting in the $^3[3/2]_{1/2}$ state (Sec. 2.4.2).

3.3.2 High Stability Optical Mechanics Design

To enhance stability and minimize maintenance requirements, we designed a set of boards for the upgrade. These boards have been individually tested and are ready for deployment to the existing system.

All optical mechanics are directly bolted down to a solid aluminum baseboard. The orientation is referenced with dowel pins, rather than being clamped with forks and pedestals. The beam height from the baseboard is set at 0.75 inch.

Lowering the beam height enhances stability. Avoiding the use of forks allows us to position individual optical elements closer together, making the setup more compact and reducing its footprint. The use of dowel pins not only enables precise placement of individual components but also facilitates the removal and reinstallation of optical elements with minimal effort needed for realignment.

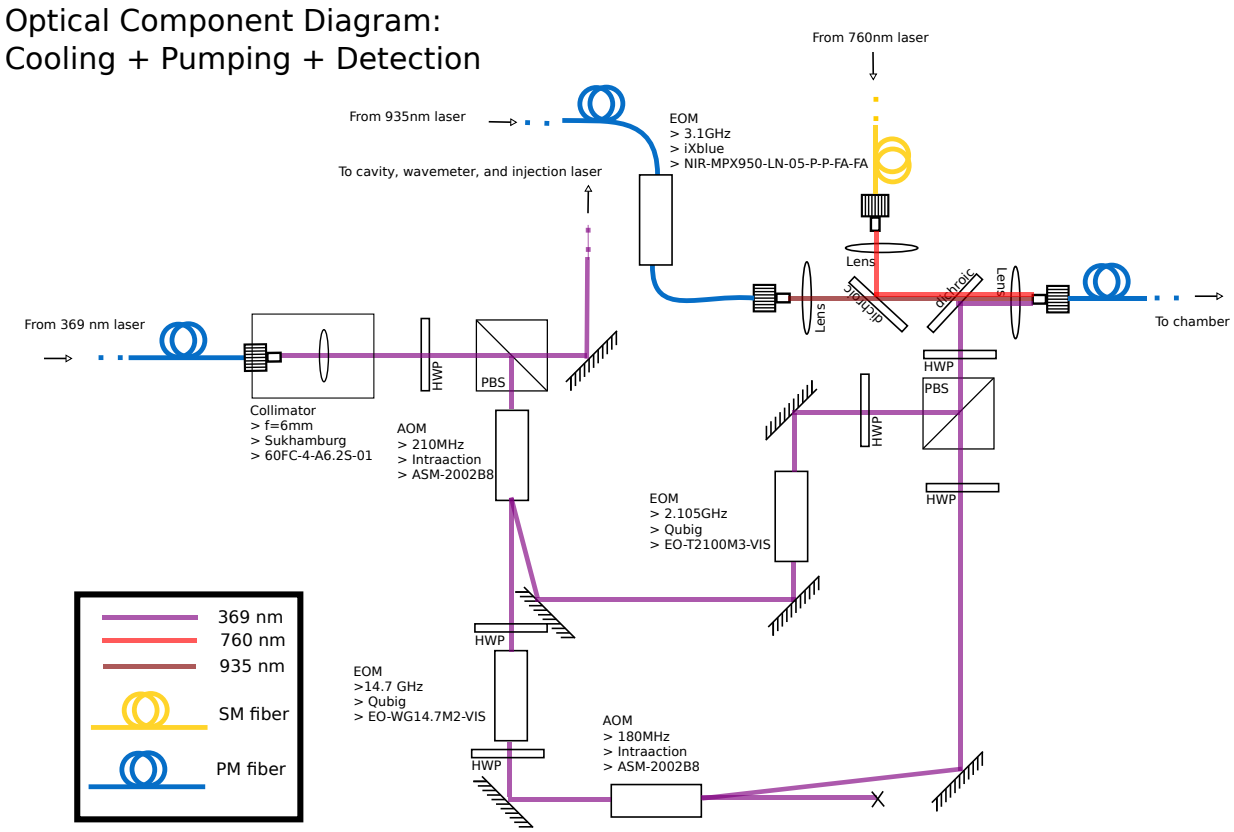

Figure 3.4: Schematic for preparing the cooling, detection, optical pumping beams, and repumping beam preparation. The SM and PM fibers denote single-mode and polarization-maintaining fiber respectively.

We designed and constructed two boards. The first one houses an ECDL and the optics for the cooling beam, while the second contains the optics for the detection and optical pumping beams.

Laser and Cooling Board

Fig. 3.5 shows the cooling board. Mounted on it is an external cavity diode laser (ECDL) from Moglabs, which outputs a 369 nm laser and passes it through an optical isolator (711C-1 from Conoptics). The board also features a double-pass AOM setup.

We opted for shearing mode tellurium dioxide (TeO_2) AOMs from Brimrose instead of fused silica or quartz. This is due to TeO_2 AOMs having a larger deflection angle because of their slower acoustic velocity (0.6 km/s for shearing mode[60] versus 4.2 km/s for longitudinal mode[42]), resulting in a cleaner separation between the diffracted beam and the non-diffracted beam. We recorded an extinction ratio of more than 60 dB (limited by the photo sensor's dynamic range) between turning the AOMs on and off. The exact relation between the acoustic velocity and the deflection angle is discussed in section 6.4.4.

Detection and Optical Pumping Board

The detection and optical pumping board accommodates four double-pass AOM setups within a 24-inch by 24-inch area. Fig. 3.6 illustrates this board. The four modules correspond to the controls of two sets of detection and optical beams for both global illumination and individual addressing. To ensure this intricate optical setup fits within the board's confines, we use supports to vertically route and fold the beams, thus reducing their footprint on the board.

The global detection and optical pumping beams are merged using a polarization beam splitter and then directed to another vertically-mounted board. This secondary board is furnished with multiple dichroic beam splitters to further amalgamate the beam with the repumping beams (935 nm, 760 nm) delivered via fiber. The combined beam is then coupled into the single-mode photonic crystal fiber, as mentioned in Sec. 3.3, and transported to the chamber.

Similarly, the individual optical pumping and detection beams are combined with a polarization beam splitter and coupled into a polarization-maintaining fiber. We aim to deliver the beam to the individual addressing system as described in Chapter 4.

Beyond the 935 nm and 760 nm beams, we've also reserved beam paths for 411 nm, 435 nm, and 1650 nm lasers. These wavelengths are instrumental for shelving the ion into

Front

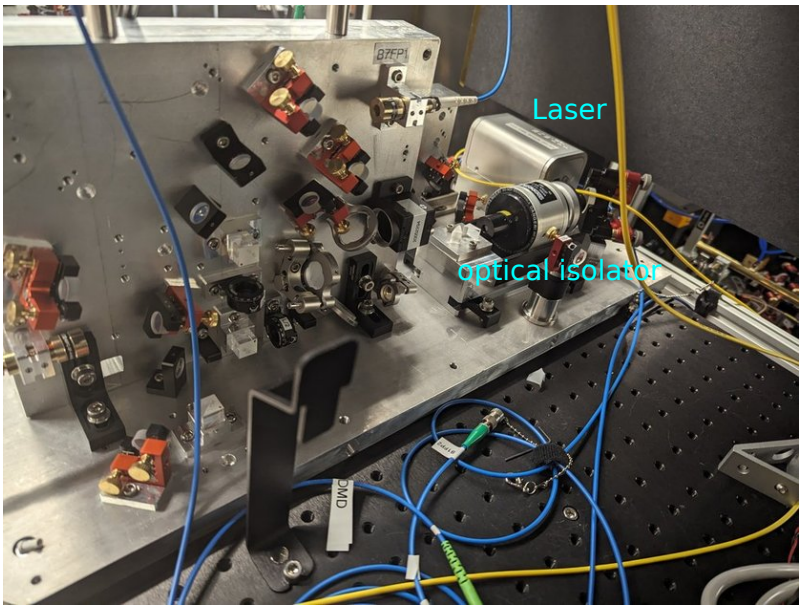

Back

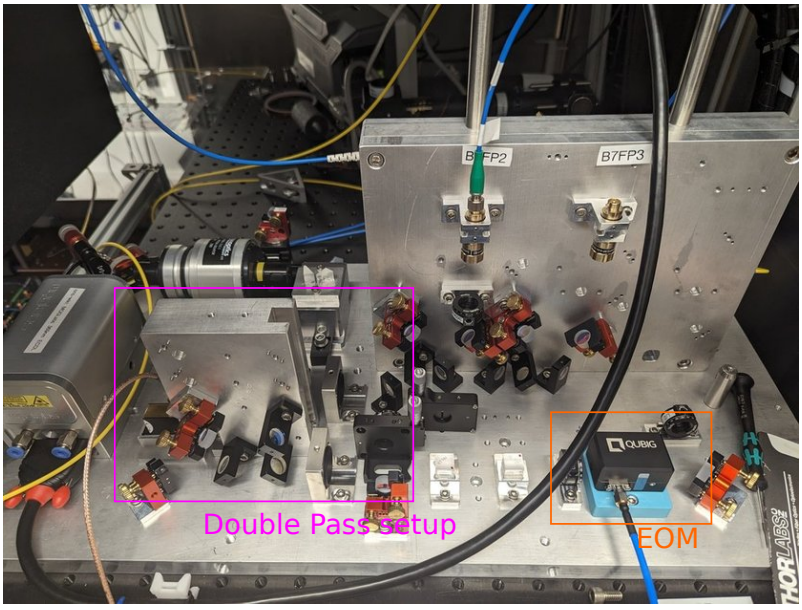

Figure 3.5: Photograph of the optical board for the cooling beam. This optomechanical design was collaboratively created by myself and Paige Angela Harford, a co-op student in the lab.

the metastable states, and we plan to deploy them in future experiments[59, 72, 20]. More details about these transitions can be found in Fig. 2.1.

3.3.3 Approach for Designing High Stability Optical Mechanics

Given that all mounting holes of the optical elements need to be precisely positioned on the board, any errors in placement or orientation could make the entire board unusable.

To minimize human error, we've developed a unique approach and a set of tools to assist with the design process. Instead of creating a CAD model of the baseboard directly, we create individual CAD models for each optical element and use an in-house developed Python program to generate the baseboard model. These individual CAD models include not only the 3D model of the optical element but also instructions for drilling the mounting holes and the dowel pin holes. To make them usable by the program, we ensure that each CAD model follows a convention regarding orientation and placement relative to its own origin. This convention is illustrated in Fig. 3.7.

While designing the board, rather than specifying the placement of individual elements, we indicate how we want the laser beam to be routed. The Python program we've developed determines the precise orientation of each element and programmatically constructs the 3D model of the baseboard. More specifically, the program interfaces with Autodesk Inventor through its Component Object Model (COM) and uses Inventor as its CAD engine to generate the CAD model.

The program was a joint effort between myself and two co-op students, Austin Con, and Mariah De Torres. I conceived the original idea and supervised the development. Austin implemented the functionality for CAD model synthesis, while Mariah implemented the Python scripting interface, allowing us to design the board through Python scripting.

3.4 Imaging System

The imaging system consists of a microscope objective and a set of lenses designed to image the ion onto photo sensors.

The microscope objective collimates the fluorescence light emitted from the ion, and the beam is subsequently focused by a lens with a 125 mm focal length to re-image the ion. At the focus (the image plane), we have an adjustable slit and an iris, which serve to filter out undesired scattering. The image is subsequently relayed by two 125 mm lenses

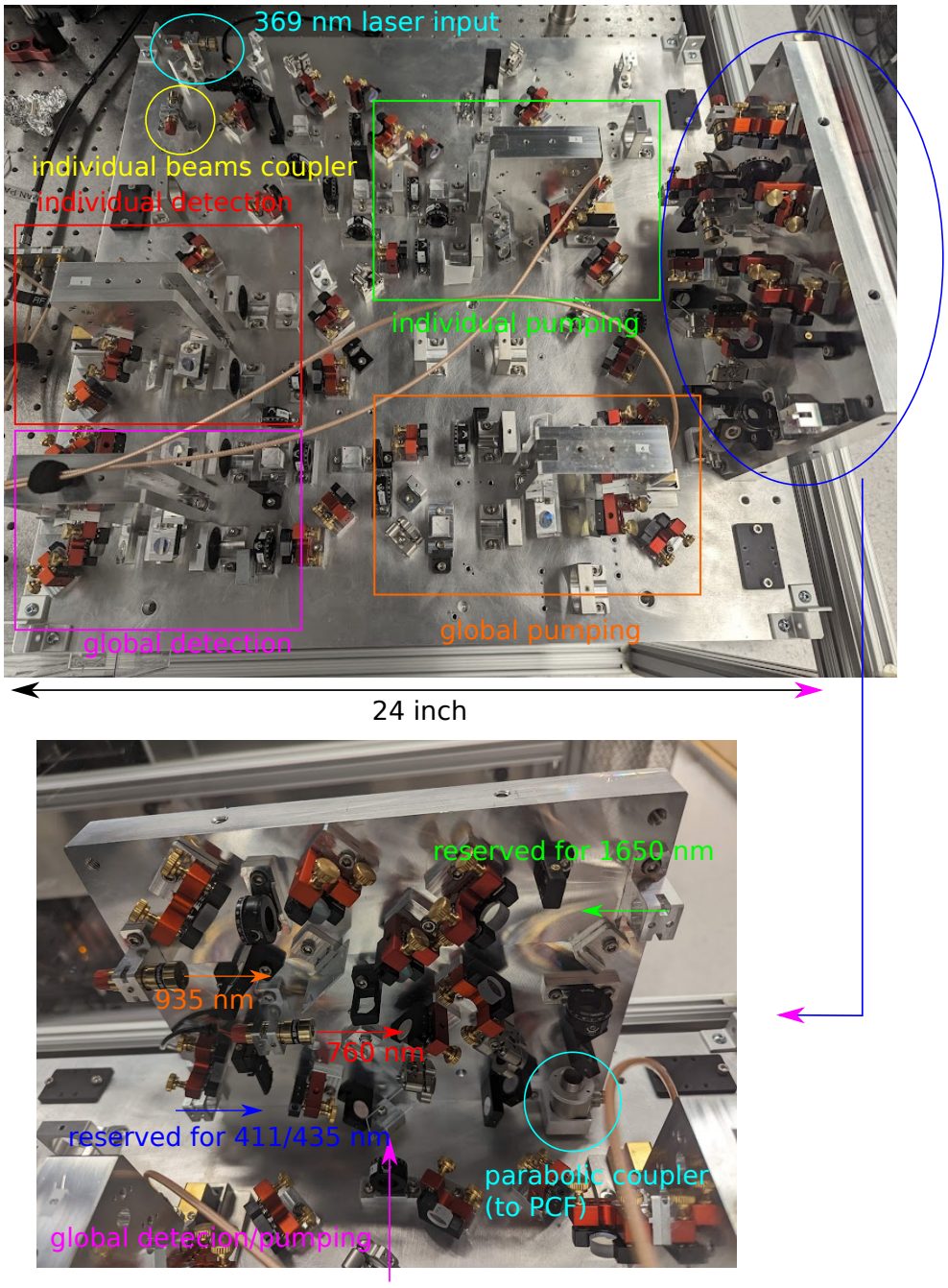

Figure 3.6: Photograph of the optical board for the detection and optical pumping beams. This optomechanical design was collaboratively created by myself, Zi Yan Li

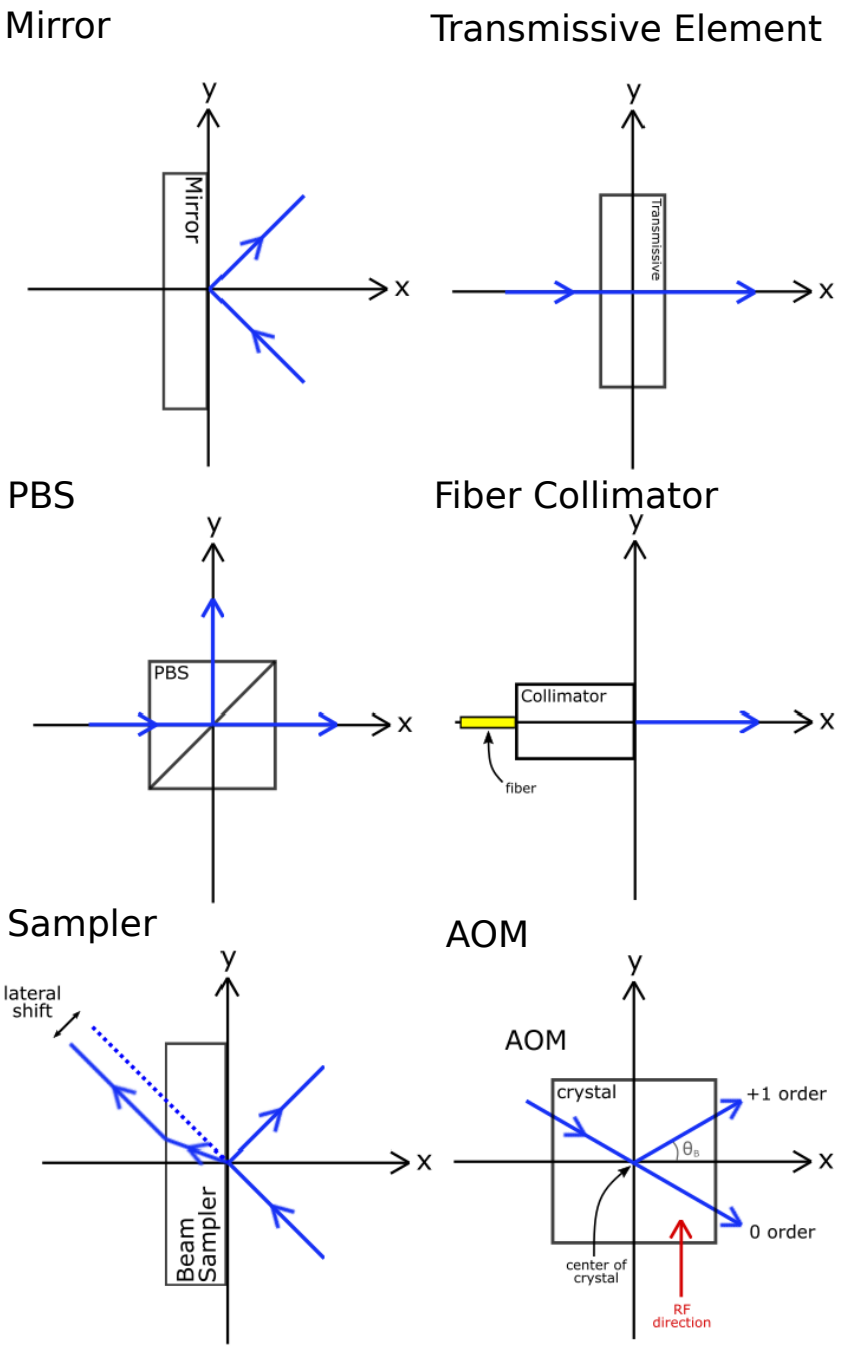

Figure 3.7: Convention for the orientation and placement of the optical elements.

to either the camera or the photomultiplier tube (PMT). An electronically controllable flip mirror (MFF101 from Thorlabs) is used to switch between the camera and the PMT.

Before the beams hit the iris, a pellicle beam splitter combines the path of the individual addressing beam, allowing the same objective to be used for individual addressing. More details about the individual addressing system can be found in Sec. 4.3.

3.4.1 Microscope Objective

The microscope objective we utilize is a custom design that I created, guided by a few key criteria:

1. Field of view: Our aim was to have a field of view that allows us to image a lengthy chain of ions. We designed it to be 400 μm, which is sufficient for imaging 20 ions with 6 μm spacing. The extra field of view also allows us for an easier alignment.
2. Reduced input aperture: It was desirable to minimize the input aperture of the objective to enable the use of a 1-inch circular mirror for directing the light. Our goal was to have a 10 mm input aperture, smaller than the 1-inch cross-section at 45 degrees, which is $25.4/\sqrt{2} = 17.63$ mm. This is not feasible with a single-lens design, such as using an aspheric lens.
3. All fused silica design: We wanted to maximize the transmission of 369 nm light, making fused silica the optimal material for our purposes.

In Fig. 3.8, the schematic of the design is presented. The design comprises six lenses and the vacuum window of the top viewport, and all the lenses are off-the-shelf items from Thorlabs. The objective is housed within an SM1 lens tube from Thorlabs. Between the lenses, CNC-machined Delrin spacers have been used to ensure the correct inter-lens spacing. Below are the key parameters of the design:

1. Image Space NA: 0.2
2. Primary Wavelength: 369 nm
3. Effective Focal Length (EFL): 23.9855 mm
4. Entrance Pupil Diameter: 10 mm

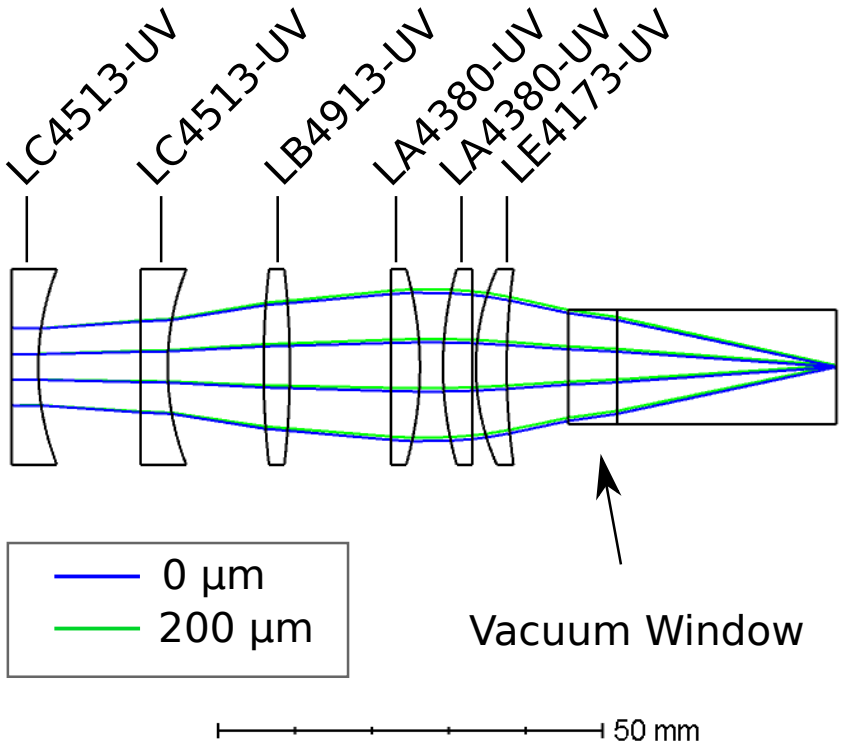

Figure 3.8: Schematic of the microscope objective.

5. Infinite Conjugate

The prescription of the design is table 3.1 with a 6.35 mm thick Vacuum window included.

Table 3.1: Prescriptions of the microscope objective. "F_SILICA" is the fused silica material, and "VACUUM" is the vacuum. The part number of the off-the-shelf lenses are denoted in the Comment column. The microscope objective is optimized with a field of view of 400 μm and constraining the numerical aperture at 0.2 NA and with 10 mm entrance pupil diameter during optimization, and the performance metrics are presented in Fig. 3.9.

Surface	**Type**	**Comment**	**Radius [mm]**	**Thickness [mm]**	**Material**
0	STANDARD	-	Infinity	Infinity	-
1	STANDARD	LC4513-UV	Infinity	3.50E+00	F_SILICA
2	STANDARD	-	3.45E+01	1.33E+01	-
3	STANDARD	LC4513-UV	Infinity	3.50E+00	F_SILICA
4	STANDARD	-	3.45E+01	1.25E+01	-
5	STANDARD	LB4913-UV	1.14E+02	3.41E+00	F_SILICA
6	STANDARD	-	-1.14E+02	1.31E+01	-
7	STANDARD	LA4380-UV	Infinity	3.78E+00	F_SILICA
8	STANDARD	-	-4.60E+01	3.00E+00	-
9	STANDARD	LA4380-UV	4.60E+01	3.78E+00	F_SILICA
10	STANDARD	-	Infinity	5.00E-01	-
11	STANDARD	LE4173-UV	3.10E+01	4.00E+00	F_SILICA
12	STANDARD	-	9.12E+01	8.00E+00	-
13	STANDARD	Vacuum Window	Infinity	6.35E+00	F_SILICA
14	STANDARD	-	Infinity	2.85E+01	VACUUM
15	STANDARD	-	Infinity	0.00E+00	-

In Fig 3.9, we present the performance metrics of the design evaluated by Zemax Optics Studio. This design demonstrates low aberration ($< 0.03\lambda$ RMS) within a field of view of 400 μm. The part numbers of the off-the-shelf components from Thorlabs are included in the comment column of the table.

Comparing to the use spherical lens and aspheric lens, a micro objective composites of multiple lenses offers a few advantages. First, comparing to spherical lenses, the objective can be optimized to compensate the spherical aberration, which is a dominant source of error for spherical lens in high NA applications, by having multiple lens surfaces canceling

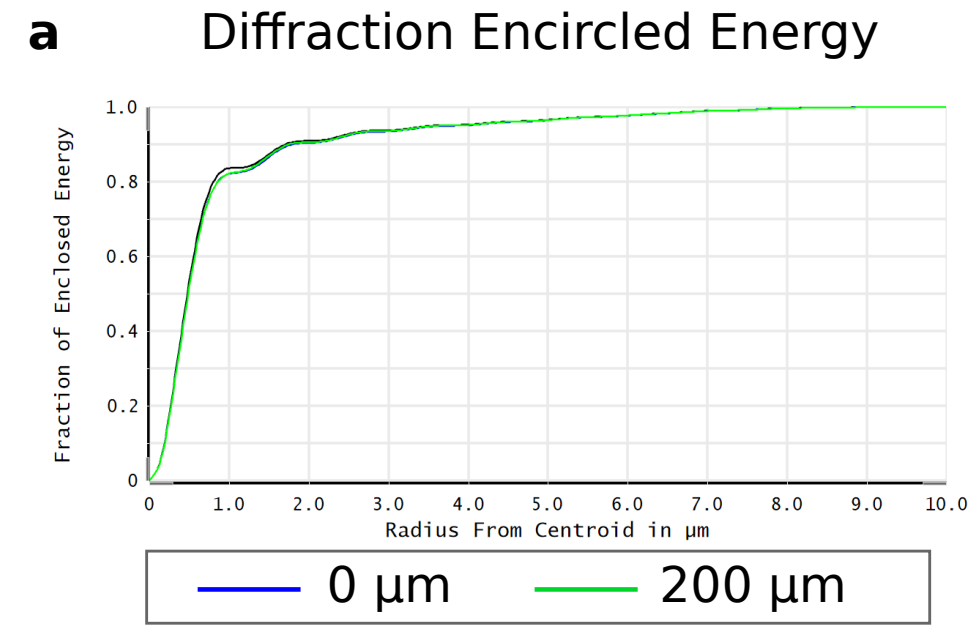

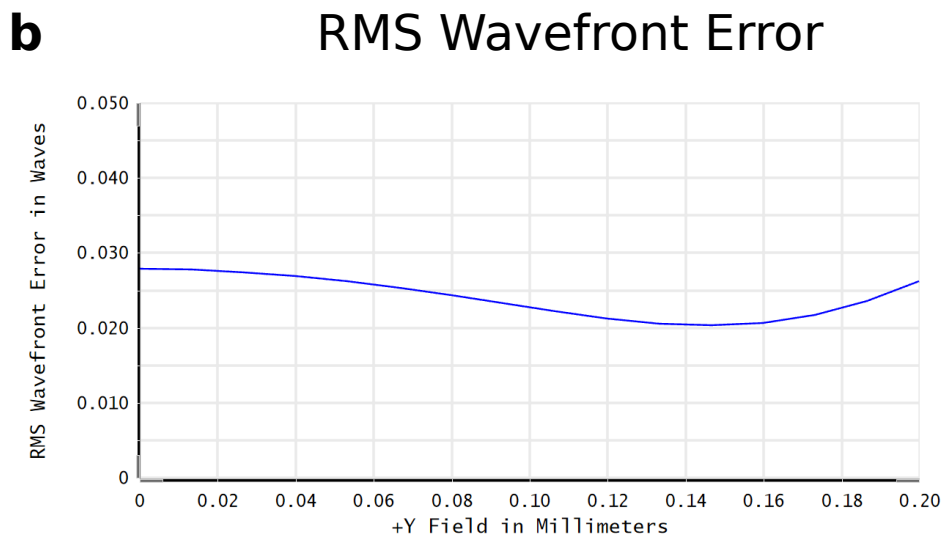

Figure 3.9: Performance of the microscope objective. **a.** Diffraction Encircled Energy Diagram. This diagram shows the encircled energy of the 0 μm (center of the targeted FOV) and the 200 μm (edge of the targeted FOV) field points. The diffraction limit is also plotted for comparison. **b.** RMS Wavefront Error across the field of view. Both diagrams are evaluated with a uniform input field and 100 mm input aperture.

each other's aberration and eventually resulting in a low net aberration. Aspheric lenses, on the other hand, is optimized to remove spherical and high-order aberration, but it is optimized for a single field point. As a result, the aspheric lens has a lower field of view and suffers more aberration with angular dependencies (e.g. coma).

In addition, for trapped ions or cold atom experiments, ions (or atoms) are within the Vacuum chamber. This limits the minimum working distance of the optics. With the objective we can reduce the entrance pupil diameter, so it can be easier to work with, while maintaining a higher NA.

3.4.2 Detector

In our lab, we use both a photomultiplier tube (PMT) and a camera for detecting the ion's fluorescence. Based on the fluorescence signal, we can determine the quantum state of the ion.

Photomultiplier Tube

A photomultiplier tube (PMT) operates on the principle of the photoelectric effect. As shown in Figure 3.10, when a photon strikes its photoelectric surface (the cathode), there's a probability that it will excite an electron. Propelled by the potential difference, this electron will then strike the dynodes within the PMT. Each dynode collision has the potential to excite additional electrons. In this manner, akin to an avalanche, a single photon can instigate the excitation of millions of electrons. This cascade effect amplifies the photon signal, enabling us to use a counter to register each photon incident.

Given that the photons originate from the ion, only one photon can impact the PMT at any given moment (there are no two-photon or multiphoton states). To accurately register photon incidents, we require a pulse duration significantly shorter than the scattering rate, which is around 20 MHz. The PMT model we use, H11890-01 from Hamamatsu, has a pulse duration of 10 ns, meeting this requirement. As we can resolve individual photon incidents, the avalanche effect in the PMT doesn't broaden the photon counting distribution like an EM-CCD would. (We will elaborate on this in the next section).

The PMT serves as an excellent instrument for detecting the quantum state of a single ion. Our four-rod trap apparatus allows us to achieve about a 96% measurement fidelity with the PMT limited by the off-resonant scattering described in Sec. 2.4.

However, to apply it for measuring the quantum states of multiple ions at the same time. The PMT is may not be the best choice. The pitch of multi-channel PMTs is

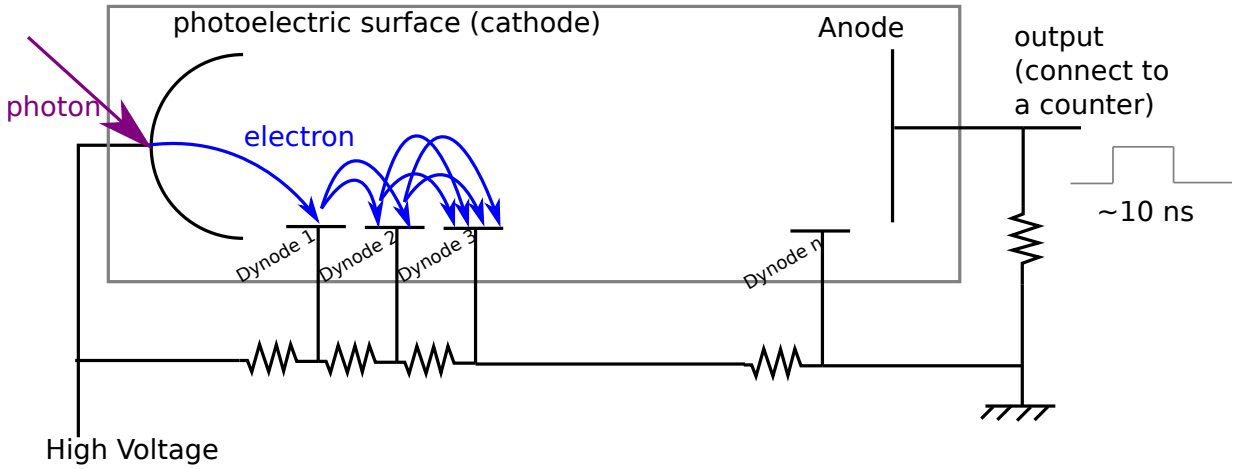

Figure 3.10: Schematic of the photo multiplier tube.

typically > 1 mm, which is orders of magnitude larger than the ion interspacing, posing challenges for the imaging system design.

Therefore, in our lab, we use the PMT for detecting a single ion state or total fluorescence of the ions (e.g., measuring total magnetization of a spin chain), and we use a camera for measuring the individual quantum state of multiple ions.

Camera

For a camera sensor, when a photon hits the semiconductor of the sensor, there is a chance that the photon will excite a pair of electrons and holes. The electric field within the sensor would then guide the generated photocharge to photodetection circuits, which convert the photocharge Q into a voltage signal V.

$$V = \frac{1}{C}Q \tag{3.1}$$

where C is the effective capacitance. The proportionality of the photocharge-voltage conversion is called "charge detection sensitivity" or "conversion gain". One of the main sources of error, the readout noise σ_R, results from the detection circuit. The readout noise approximately follows the following proportional relation:

$$\sigma_R \propto C\sqrt{BT} \tag{3.2}$$

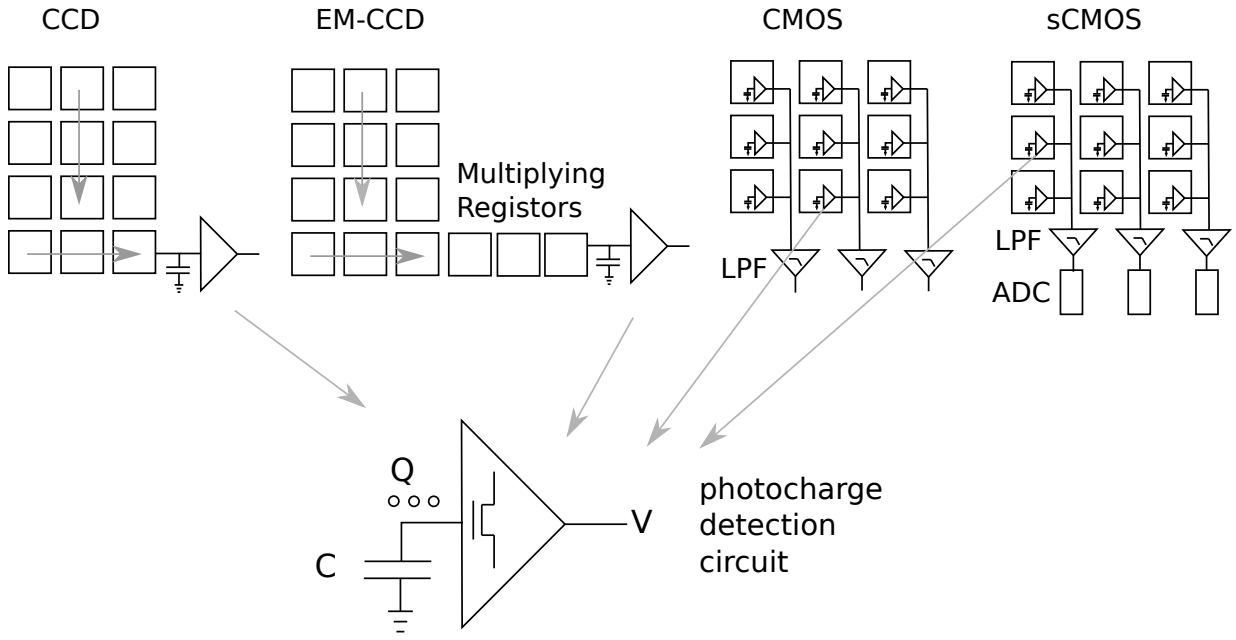

Figure 3.11: Architecture of different types of camera sensors. LPF is the abbreviation of low pass filter, and ADC is the abbreviation of analog-to-digital converter.

where B is the bandwidth of the detection circuit and T is the absolute temperature. Compared to another type of noise, dark current noise σ_D, which results from the thermally excited electron-hole pairs captured by the detection circuit, the readout noise is the dominant source of error for ion state detection. The duration of the trapped ion state detection process is typically between 10 μs to 1 ms, and the dark current noise that occurs during this time is negligible with a sufficiently cooled sensor. Note that the dark noise is proportional to the square root of the exposure time, but the readout noise is independent of the exposure time.

Shown in Fig. 3.11, we illustrate the architecture of different types of camera sensors.

For charged coupling devices (CCDs), the charge is stored in the potential well of the sensor. During the readout, the charges shift from pixel to pixel and eventually to the readout electronics. The typical readout noise of CCD is ~10-100 e^-. It was a significant breakthrough in the 1990s when it was invented. However, the readout noise is insufficient for many scientific applications.

To further reduce the readout noise, the electron-multiplying CCD (EM-CCD) was developed. The EM-CCD has a multiplication register that multiplies the photocharges

by a factor typically of the order of 1000. The photocharges after multiplication are much higher than the readout noise, effectively eliminating it. However, the multiplication process is stochastic. In the high gain limit and high number of multiplication registers, the probability distribution $p(x)$ of the output multiplication registers can be approximated as,

$$p(x) = \frac{x^{n-1} \exp(-x/g)}{g^n (n-1)!} \tag{3.3}$$

[2] where n is the number of electrons at the input of the multiplication registers, and g is the average gain. This broadens the statistical distribution of the photon counts and thus halves the quantum efficiency (QE) of the device[2].

On the other hand, the CMOS (complementary metal oxide semiconductor) sensor has a photodetection circuit for each pixel. The photocharges are converted to voltages and read out directly. This allows for a much faster readout speed as multiple pixels can be read out simultaneously. In addition, the CMOS sensor is compatible with modern semiconductor manufacturing processes. Moreover, low-pass filters can be integrated into the CMOS sensor to reduce the readout bandwidth B, resulting in a lower readout noise σ_R as described in Eq. 3.2. Modern CMOS sensors can easily achieve readout noises less than $10e^-$.

As fabrication technology improves, more electronics can be integrated into the CMOS sensor. The invention of the scientific CMOS (sCMOS) further integrates multiple analog-digital converters (ADCs) into the sensor. This allows for parallel readout of the voltages, maintaining the same data readout speed but reducing the readout noise by using a low-pass filter with an even lower bandwidth.

In addition to the bandwidth B in Eq. 3.2, another important parameter is the effective capacitance C. The advancement in semiconductor manufacturing technology allows for the fabrication of very small structures. Ma et al. (2017)[44] demonstrated image sensors with a 0.21 e^- readout noise. The ultra-low readout noise allows for resolving individual photon counting, and this type of sensor is called a quantitative CMOS (qCMOS).

Both EM-CCD and qCMOS offer superior signal-to-noise ratios (SNR), however, the noise profiles of the two sensors are very different. In Fig. 3.12, we show the simulation of photon counting statistics of a qCMOS sensor, an EM-CCD, and a hypothetical noise-free sensor. We can see the EM-CCD has a significant broadening of the photon counting distribution for ions in the bright state $|1\rangle$. As for the qCMOS, the broadening is independent of the photon number. Consequently, the optimal detection threshold and exposure time will differ for the two sensors. In general, qCMOS tends to favor slightly longer detection

times. Additionally, it appears that the qCMOS camera tends to favor a slightly higher detection threshold than the EM-CCD.

In our lab, we use a qCMOS camera (C15550-20UP from Hamamatsu). The qCMOS camera has a readout noise of 0.27 e^-. It offers a significant improvement in readout speed over the EM-CCD, especially with a long chain of ions, as the qCMOS reads the entire row of pixels simultaneously. For the ultra-quiet mode (the lowest readout noise at 0.27 e^-), it takes 0.375 ms to read out a row of pixels. On the other hand, EM-CCD typically takes a few ms to tens of ms depending on the number of pixels being read.

When designing the imaging system for the qCMOS camera, it would be beneficial to limit the spread of the ion spot to the size of a pixel (4.6 μm), as the readout noise exists in individual pixels. As for the EM-CCD, there is no such requirement. For historical reasons, our imaging system is not optimized for the qCMOS camera. However, we can achieve a $\approx 94\%$ fidelity with the current system, and we are implementing an upgrade to the better focus the light to a single pixel.

The ion-state classifier is implemented with a random forest algorithm[29, 58] and trained with dark and bright state images prepared with microwave rotation (Sec. 2.5.1). The random forest algorithm is an ensemble machine learning algorithm, which consists of multiple decision tree classifiers. Each decision tree is trained with resampled data from the training images. The final classification is determined by the majority vote of the decision trees. The random forest algorithm is robust to overfitting and can find the optimal classification boundary in the high-dimensional feature space (multiple pixels). The use of a machine learning algorithm performs better than summing the counts within a region of interest, as direct summing over pixels accumulates the readout noise, but the machine learning algorithm is not affected when using a larger region of interest.

3.5 Raman Optics

Both the Raman 1 beam (R1) and the Raman 2 beam (R2) originate from the same laser source (Paladin 355-8000 from Coherent), each being modulated by an AOM. The laser we use is a picosecond-pulsed type. The rationale for selecting this laser will be discussed later in Sec. 3.5.

The RF source for the AOM of R1 is an arbitrary waveform generator (AWG). The optics are designed such that the AOM and the ion position are imaging conjugates, allowing beams modulated by different RF frequencies to overlap at the ion plane. The modulation frequencies of the two AOMs are $f_{R1} = 211$ MHz for R1 and $f_{R2} = 185$ MHz for R2. As

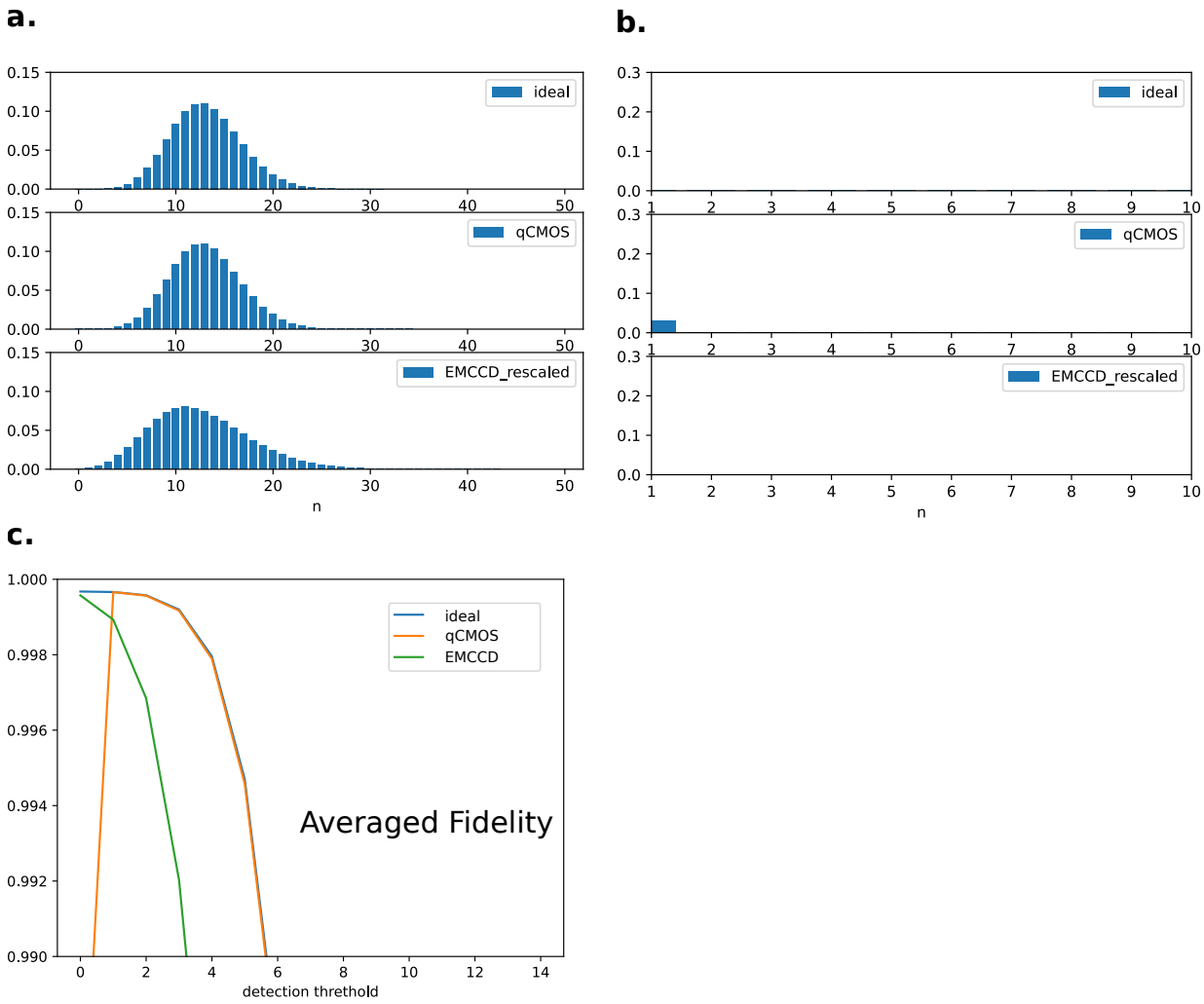

Figure 3.12: Photon counting statistics for a qCMOS sensor, an EM-CCD, and a hypothetical noise-free sensor. **a.** Photon counting distribution of bright states. **b.** Photon counting distribution of dark states. We plot from 1 count to 10 counts as the majority of the counts are at 0 count. We plot the distribution excluding 0 counts to highlight the differences. **c.** Average (between dark and bright state) fidelity versus the detection threshold. The simulation is performed with the following parameters: $I/I_{\text{sat}} = 1$, 400 μs detection time, 0.27 e^- readout noise for qCMOS, 0.4 NA, 0.2 Quantum Efficiency (QE), 1000 em-gain for EM-CCD. The averaged fidelity is defined as the average of the dark state measurement fidelity and the bright state measurement fidelity.

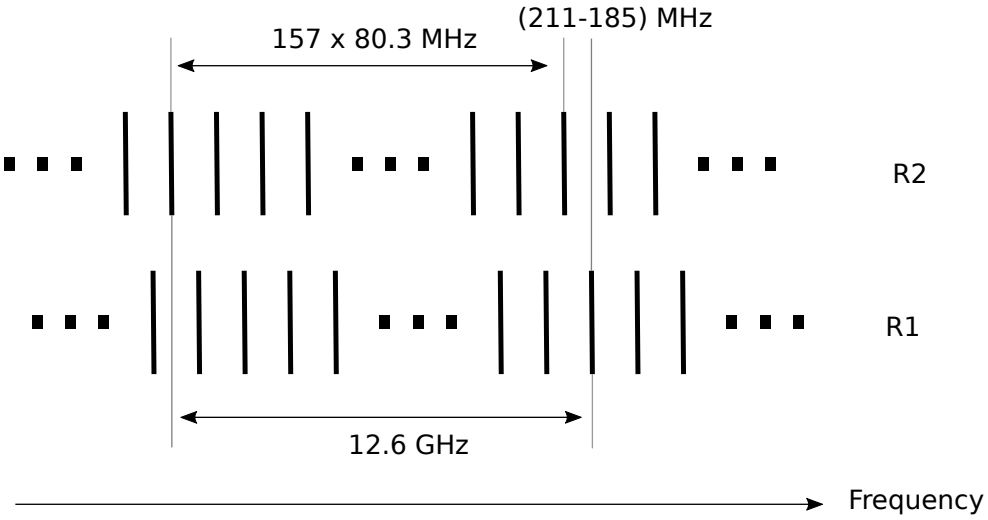

Figure 3.13: Comb tooth frequencies of R1 and R2

shown in Fig. 3.13, these two frequencies are chosen such that the qubit frequency splitting is equal to one beam path's comb tooth and the comb tooth that is 157th splitting away. The comb tooth splitting is essentially the repetition rate ν_{rep} of the pulse laser, which is 80.3 MHz.

$$157 \times \nu_{rep} + (f_{R1} - f_{R2}) = \tag{3.4}$$
$$157 \times 80.3\text{MHz} + (211\text{MHz} - 185\text{MHz}) \approx 12.6 \text{ GHz} \tag{3.5}$$

Polarization and Orientation

The beams R1 and R2 are set to be 90 degrees apart, and the difference in wave vectors is along the radial direction of the ion chain. This arrangement minimizes coupling to the axial mode of the ions.

The magnetic field, responsible for determining the spin's quantization axis, is produced by a pair of bias coils connected to the vacuum chamber. The magnetic field is oriented along the R1 direction. Both R1 and R2 are linearly polarized, with their polarization orientations chosen to be perpendicular to each other. Moreover, there is no π-polarization component present. The selection of polarization orientation and magnetic field direction is motivated by several reasons:

The chosen polarization orientation and magnetic field direction serve several purposes, as outlined below:

1. Minimize coupling to Zeeman states: The suppression of the π-component of polarization helps minimize the coupling to the Zeeman states $|F = 1, m_F = -1\rangle$ and $|F = 1, m_F = 1\rangle$.

2. Minimize coupling to axial phonon modes: The difference in beam pointing between R1 and R2 leads to a beat note along the axial phonon direction. This choice minimizes the coupling to these modes.

3. Minimize fourth-order AC Stark shift: Linear polarization ensures that the individual Raman beams have a zero fourth-order AC Stark shift[39].

Laser Selection

In terms of laser selection, pulsed lasers have been widely adopted in trapped ion quantum information processing platforms, particularly for those employing the $^{171}Yb^{+}$ qubit. The use of pulsed lasers allows us to use different comb teeth to facilitate Raman transition. This eliminates to have a separate phase-locked laser detuned by the qubit transition (12.6 GHz), as it is challenging to shift the frequency of laser by such a large amount.

While choosing the laser, the following laser requirements must be met:

- Pulse Duration: The pulse duration of the laser affects the width of the envelope encompassing multiple frequency combs. To achieve sufficient Rabi frequency for the two comb teeth, the pulse duration must be long enough so that its Fourier transformation, which corresponds to the envelope in the frequency domain, covers the two qubit states.

- Repetition rate: The repetition rate of the laser determines the frequency separation of the comb teeth. As coherent quantum operations for entanglement often involve phonon-mediated spin-spin interactions, it is ideal for the frequency separation between comb teeth to be larger than the trap frequency. This allows the contributions of other comb teeth to be ignored or minimized.

- Wavelength: Although the Raman transition, as a two-photon process, does not impose strict constraints on the laser wavelength, it is preferable to select a wavelength that has minimum Stark shifts and differential Stark shifts between qubit states, as

these could add further complexity to the system. Additionally, in practice, it is desirable to choose a wavelength for which high-power lasers are readily available, since two-photon processes generally necessitate greater optical power. A common choice for this purpose are Nd:YAG lasers[8].

For $^{171}Yb^{+}$ hyperfine qubits, the frequency separation between the two qubit states is $\omega_{HF} = 2\pi \times 12.6\text{GHz}$[8]. Consequently, the pulse duration should be shorter than tens of picoseconds ($\ll 1/\omega_{HF}$). In the case of a linear Paul trap, the typical radial trap frequency amounts to a few MHz. As such, it is preferable to have a repetition rate an order of magnitude higher than this value.

We selected the Paladin 355-8000 laser from Coherent. This tripled Nd:YAG laser features a wavelength of 355 nm, a repetition rate of 80 MHz, and a pulse length of approximately 15 ps. The repetition rate and pulse duration satisfy the criteria. In addition, the 355 nm wavelength lies between the D_1 and D_2 line transitions of $^{171}Yb^{+}$, thereby cancelling the majority of the Stark shift and differential Stark shift[8].

Electronics: PLL for beat note lock

The beat note from the laser can drift or fluctuate over time. Therefore, it is important to correct for this beat note frequency drift.

Instead of providing feedback to the laser (which lacks an exposed control port in the model we use), we measure the beat note and adjust the frequency of the R2 AOM, f_{R2}, to ensure Eq. 3.4 still holds.

This is achieved by using a phase-lock loop (PLL) to multiply the beat note frequency by 157 ν_{rep} and feedforward to the R2 AOM. The electronic setup is illustrated in Fig. 3.14. The pulsed laser's output is measured by a fast photodiode (G4176 from Hamamatsu), and its signal is mixed with a 79.16 MHz RF signal before passing through a low pass filter (LPF).The filtered signal is $1.185\text{MHz} + \delta\nu_{rep}$, where $\delta\nu_{rep}$ is the drift of the beat note frequency.

This signal frequency is then multiplied by 157 using the PLL, resulting in an output frequency of $186\text{MHz} + 157\delta\nu_{rep}$, which is used for the R1 AOM. As a result, the beat note frequency drift is amplified 157 times, effectively canceling the impact of the beat note frequency drift in Eq. 3.4. Therefore, the two comb teeth depicted in Fig. 3.13 remain resonant with the qubit transition.

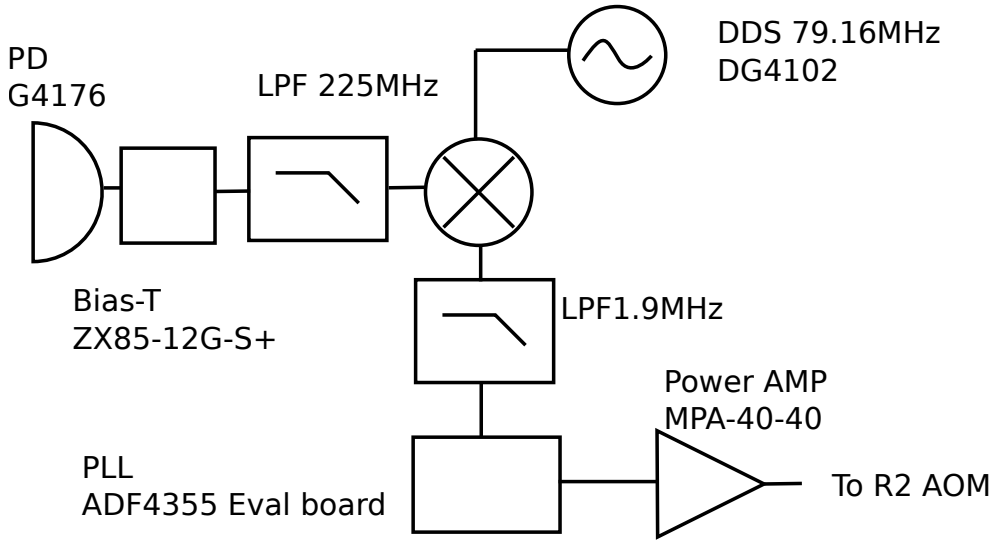

Figure 3.14: Schematic illustrating the beat note lock circuit with PLL. LPF stands for low pass filter, AMP for amplifier, PD for photodiode, DDS for direct digital synthesizer, and PLL for phase lock loop.

Electronics: AWG for multi-tone generation

The AWG we utilize for the experiment is the M4i.6621-x8 from Spectrum Instrumentation. This AWG is equipped with a PCI Express Gen2 x8 interface, facilitating high-speed (4.0 GB/s) data transfer between the computer and the AWG. This data transfer rate surpasses many commonly used interfaces, such as gigabit Ethernet (≈125 MB/s) and USB 3.0 (≈625 MB/s), by orders of magnitude. This marked improvement substantially reduces experimental overhead and enhances the duty cycle of the experiment.

The AWG's output has a 16-bit depth and a 625 mega samples per second sampling rate. The output bandwidth is fast enough to directly drive the AOM, eliminating the need for additional up conversion.

The use of AWG enables us to generate multiple phase-coherent waveforms simultaneously. This is particularly useful for the Floquet experiment, where we need to generate multiple waveforms with different phases. The AWG also allows us to periodically change the phase of the waveform in a programmatic manner, which is necessary for implementing the Floquet Hamiltonian used in chapter 5.

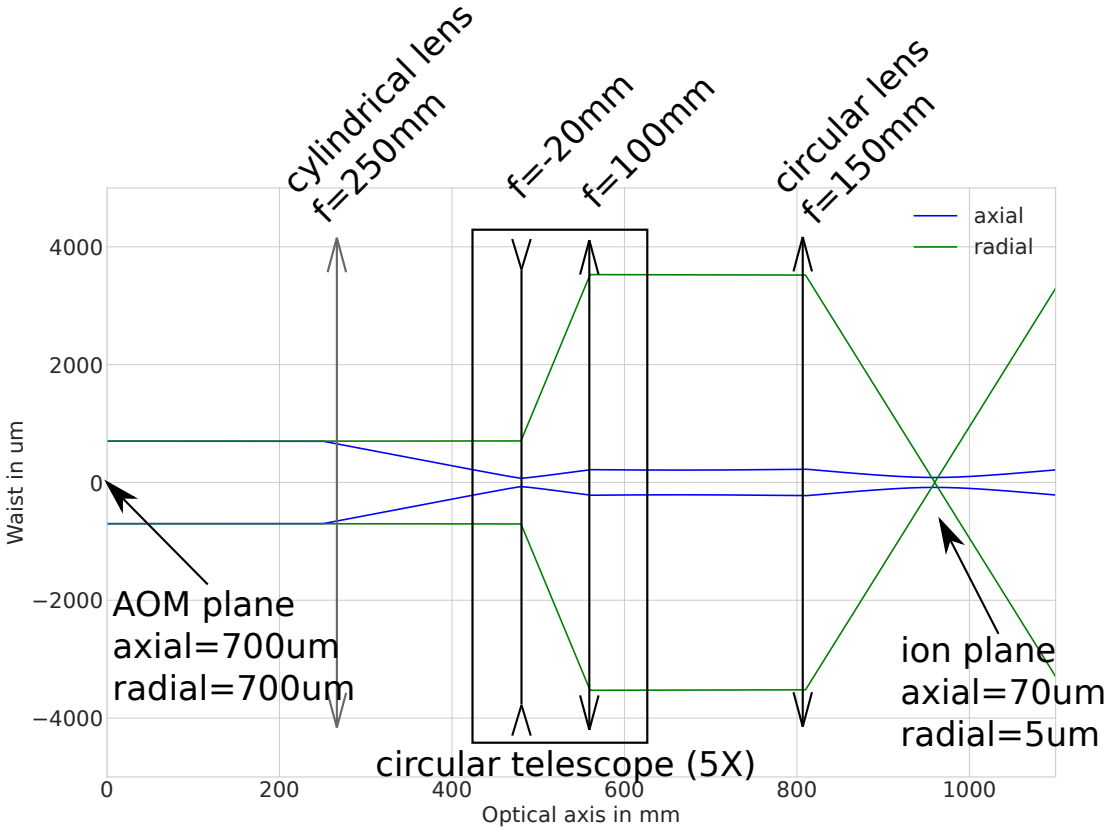

Figure 3.15: Schematic and beam waist simulation for the Raman beam. The double-headed arrows is the notation of the lens. We use the convention that a diverging lens has inwards pointing arrows and a converging lens has outwards pointing arrows.

3.5.1 Beam Shaping Optics

We employ identical beam shaping optics for both R1 and R2 after their respective AOMs. The only discrepancy in optics stems from the waveplates, which are set to different angles to control the polarization in order to satisfy the requirements discussed previously in Sec. 3.5.

In Fig. 3.15, we present the schematic and simulated $1/e^2$ beam waist in two axes from the AOM to the ion. The simulation is based on paraxial Gaussian beam propagation. At the AOM plane, the beam waist measures 700 μm in both directions. At the ion plane, the beam waist along the axial direction is 70 μm and along the radial direction, it is 5

μm. The disparity in beam waist across the two directions is attributed to the utilization of a cylindrical lens.

The AOM deflection direction corresponds to the axial axis. It's important to note that in the axial direction, the AOM plane and ion plane are conjugate focal planes. Consequently, beams deflected at different angles by the AOM will overlap again at the ion plane. This allows us to generate beams with multiple RF frequencies that share the same beam profile at the ion plane.

3.6 Conclusion

In this chapter, we presented the experimental apparatus for the trapped ion quantum processor. This includes the ion trap, the laser system, imaging system, and the electronics.

The apparatus will be used for the experiments performed in the chapter 4 and 5.

Chapter 4

Individual Optical Addressing of Trapped Ions

In this chapter, we will discuss the experimental setup and the techniques utilized for individually addressing trapped ions with holographic beam shaping methods. We will also delve into the experimental results derived from the implementation of these techniques. Some of the results presented in this chapter have also been published in Shih, et al. (2021)[62] and Motlakunta, et al. (2023)[50].

The research presented in this chapter has been a collaborative endeavor, with contributions from Sainath Motlakunta, Nikhil Kotibhaskar, Manas Sajjan, Anthony Vogliano, Darian Mclaren, Lewis Hahn, Jingwen Zhu, Roland Hablutzel, and Rajibul Islam.

My main contributions are leading the development of the holographic beam addressing system in the hardware implementation, the optical design and the software framework. I also develop the algorithm for hologram generation, and establishing the protocol for both optical aberration characterization and crosstalk error characterization.

Besides, I conducted the experiment, data analysis presented in this chapter and for the publication in both Shih, et al. (2021)[62] and Motlakunta, et al. (2023)[50].

My work, which has facilitated the results presented in this chapter, has also led to the following open-source software contributions:

1. **pySLM2** (as the leading developer): A python-based full stack software framework from GPU-accelerated hologram generation and simulation to hardware control.

2. **Luxbeam** (as the lead developer): A Python-based package developed for implementing the control protocol for interfacing with the DMD controller manufactured by Visitech. This package also serves as a fundamental building block for pySLM2's hardware control.

4.1 Overview

The ability to individually address trapped ions is of paramount importance in the field of quantum information processing. When we can manipulate ions at an individual level, it opens up a vast range of experimental opportunities and applications. We can categorize these applications into two groups: coherent and non-coherent optical manipulation.

1. Coherent Optical Manipulation: This allows us to entangle the internal states between arbitrary sets of ions, and perform quantum gates between them. It's an essential ingredient for general quantum computation. Additionally, it enables the engineering of non-trivial Hamiltonians for quantum simulation experiments, including the study of strongly correlated many-body phenomena[46, 63].

2. Non-Coherent Optical Manipulation: This form of operation comprises individually resetting or measuring the spin of the ions. Its applications encompass the creation of non-trivial quantum states, performance of quantum error correction, study of measurement-induced phase transitions, and study of dissipative systems.

Among these two categories, the non-coherent optical manipulation imposes more stringent requirements on crosstalk error – the error that occurs when light intended for one ion affects its neighbors. Although the errors from the coherent optical manipulation can be actively suppressed through techniques such as refocusing[56], crosstalk errors from non-coherent optical manipulation are more difficult to mitigate. This is because non-coherent operations collapse the quantum state of the ions, a generally irreversible process. Therefore, there is a pressing need for an addressing scheme that can provide ultra-low crosstalk error for non-coherent optical manipulation.

A number of techniques for this purpose have been developed, encompassing methods such as the use of an acousto-optic deflector (AOD), a multi-channel acousto-optic modulator[18, 52, 21], or laser-written guides[5], as demonstrated in previous studies.

However, these methodologies are not without their drawbacks. In the case of the AOD, the frequency of the addressing beam is contingent upon the deflection angle of the beam,

a characteristic directly correlating to the ion's position. Meanwhile, both laser-written guides and multi-channel acousto-optic modulator present their own challenges. Constructed with fixed channel spacing, both of the device are manufactured to be optimized for a single system size, limiting its adaptability. Further discourse on the comparative analysis of these techniques can be accessed in preceding literature[61].

In this chapter, we will discuss the use of a Fourier holographic beam shaping scheme we developed for ion addressing. This method allows precise control of the amplitude and phase of the light on each ion addressed independently and does not suffer from the coupled frequency and position dependence of the AOD. Additionally, a key advantage of the holographic beam shaping method is its immunity to static optical aberration resulting from the imperfections in the optical system. This allows us to achieve true diffraction-limited focusing of the addressing beam on each ion and even beyond the typical field of view (FOV) of the imaging system.

4.1.1 Outline

1. Section 4.2: We will discuss the basic principle of Fourier holography and how we can apply it to optically individual ion addressing.

2. Section 4.3: We will discuss the experimental setup for implementing the Fourier holography beam shaping for ion addressing.

3. Section 4.4: We will discuss the optical aberration characterization and correction methodology we developed. We will also present the relative experimental results.

4. Section 4.5 and 4.6: We will discuss how we measure the crosstalk error and its experimental results. In addition, we will also discuss how it transforms to the fidelity of spin reset or measurement of a target ion without collapsing the quantum state of adjacent ions.

5. Section 4.7: We will discuss the scalability of the presented scheme.

4.1.2 Change logs with Prior Publications

Major changes in setup and methodologies between the two publications[62, 50] are:

1. **Optics Setup Upgrade**: We have revamped our microscope objective from a 0.12NA to a 0.2NA system that I personally designed (refer to Sec. 3.4.1). In addition, the beam splitter responsible for merging the individual addressing beam path with the fluorescence collection has been replaced from a polarization beam splitter to a pellicle beam splitter. These changes have substantially improved our fluorescence collection efficiency. A detailed account of these alterations is provided in Section 4.3.

2. **Methodologies for optical aberration characterization**: We have adopted a novel method that leverages the ion population transfer instead of the ion fluorescence scattered from the addressing beam as the signal for optical aberration characterization. This innovative approach effectively mitigates the adverse impact of unwanted scattering from the addressing beam and significantly diminishes the power requirements for the address beam. Please refer to Section 4.4 for more exhaustive explanations.

4.2 Fourier Holography

4.2.1 Optical Fourier Transformation

In a paraxial lens system, the lens act as a Fourier transform operator mapping the electric field in one focal plane to the electric field in the another focal plane. In the context of Fourier Holography, the two focal plane are referred as the image plane (IP) and the Fourier plane (FP). Their electric fields, $E_{\mathrm{IP}}(\mathbf{x}')$ and $E_{\mathrm{FP}}(\mathbf{x})$ are related by the following equation:

$$E_{\mathrm{FP}}(\mathbf{x})\mathrm{e}^{\mathrm{i}\Phi_{\mathrm{ab}}^{(\mathrm{IP})}(\mathbf{x})} = \frac{\lambda f}{2\pi}\mathcal{F}\left[E_{\mathrm{IP}}(\mathbf{x}')\right](\mathbf{k}')\Big|_{\mathbf{k}'=\frac{2\pi}{\lambda f}\mathbf{x}}. \tag{4.1}$$

In which, $\mathbf{x}'$ and $\mathbf{k}'$ denote the spatial coordinate and the wave vector at the image plane respectively, and $\mathcal{F}$ denotes Fourier transformation. The wave vector $\mathbf{k}'$ is related to the spatial coordinate $\mathbf{x}$ at FP by $\mathbf{x} = \frac{\lambda f}{2\pi}\mathbf{k}'$.

In reality, the lens system is not perfect and the electric field at the image plane is not exactly mapped to the electric field at the Fourier plane. This is due to the aberrations in the lens system. The aberrations can be modeled as a phase map $\Phi_{\mathrm{ab}}^{(\mathrm{IP})}(\mathbf{x})$ in the Fourier plane. A more detailed derivation of this equation can be found in the Chapter 2 of Shih (2019)[61].

With that, if we are able to control the beam profile in the Fourier plane, we are able to engineer the beam profile in the image plane. In the Fourier holography, a hologram, which is a device that modified the wavefront of the beam, is placed in the Fourier plane. The hologram modified the wavefront of the beam such that the beam profile in the image plane is the desired beam profile.

4.2.2 Reprogrammable Hologram

In the context of trapped ions using Fourier hologram to engineer the individual addressing beams, we need to be able to reprogram the hologram to switch between different beam profiles. A reprogrammable hologram can be implemented with adaptive optics. There are various types of commercially available adaptive optical devices, including liquid-crystal spatial light modulators (LC-SLM)[23], deformable mirrors, and digital micro-mirror devices (DMD)[75].

A significant advantage of using adaptive optics is that they are reconfigurable. We can reprogram the adaptive optics to switch between different holograms to generate various beam profiles.

When choosing adaptive optics for our experiment, we have to consider the following factors:

1. The wavelength of the light: We need to choose an adaptive optics that can operate at the wavelength of the light we are using. In particular, our application of using the adaptive optics with Ytterbium ions requires the adaptive optics to operate at the UV wavelength.

2. The speed of the switching: The switching speed . It will affect the experiment time of the quantum algorithm and the number of operations that can be performed within the coherence time.

We choose to use digital micro mirror device (DMD) as it is capable of handling higher power at UV wavelength (up to 10 Watts in the UV and higher for longer wavelengths) and has a faster switching speed (>10 kHz) compared to other adaptive optics. In comparison, the switching speed of liquid crystal on silicon spatial light modulator (LCOS-SLM) is <1 kHz[65] and suffers from UV induced solarization unless extra UV hardening is applied.

Individual micromirrors of a DMD can be switched as fast as in 10 μs and can potentially be made even faster[14]. However, the data transfer rate between the DMD controller and

the chip is currently a bottleneck. Megahertz rate light switching, required for some QIP experiments, can be achieved by using an acousto-optic modulator (AOM) in conjunction with the DMD.

4.2.3 Hologram Generation

The individual micromirrors of the DMD can be operated with two states. In the on state, the micromirror is tilted at an angle such that the light is reflected to the desired direction. In the off state, the micromirror is tilted at an opposite angle such that the light is reflected to a different direction. This gives us local binary amplitude control of the light.

However, to achieve full control of the beam profile at the image plane, we need to be able to control not only the amplitude but also the phase of the beam. This can be achieved by creating amplitude grating with the DMD and use the diffracted beam. The amplitude grating is a periodic pattern of alternating bright and dark regions. The bright regions are the on state of the micromirrors and the dark regions are the off state of the micromirrors. The phase of the diffracted beam can be controlled by the spacial phase of the grating.

Below we show the derivation of the required grating function. For simplicity, here we use $\mathbf{k}'$ as a proxy for the spatial coordinate in the Fourier plane, keeping in mind that the FP spatial coordinate $\mathbf{x}$ is related to $\mathbf{k}'$ through the scaling, $\mathbf{x} = \frac{\lambda f}{2\pi}\mathbf{k}'$.

By deploying an amplitude grating $G(\mathbf{k}')$ in the FP, we are able to control the amplitude and phase of the diffracted beam. The grating is of the form,

$$G(\mathbf{k}') = \eta \left| \frac{F(\mathbf{k}')}{E_{\text{in}}(\mathbf{k}')} \right| \frac{1}{2}(\cos(\mathbf{k}' \cdot \mathbf{x_0}' + \Phi(\mathbf{k}') - \Phi_{\text{in}}(\mathbf{k}')) + 1), \tag{4.2}$$

where $F_{\text{k}'}$ is the Fourier transformation of the targeted image plane beam profile $f(\text{x})$. $E_{\text{in}}(\mathbf{k}')$ is the electric field of the input beam on DMD, and $\Phi(\mathbf{k}')$ is the phase profile of the target beam profile at the FP and $\Phi_{\text{in}}(\mathbf{k}')$ is the aberration phase profile of the input beam on DMD.

$$\Phi(\mathbf{k}') = \text{angle}(F(\mathbf{k}')) \tag{4.3}$$

$$\Phi_{\text{in}}(\mathbf{k}') = \text{angle}(E_{\text{in}}(\mathbf{k}')) \tag{4.4}$$

The $|\mathbf{x_0}| = \frac{\lambda f}{a}$ determines the separation between diffraction beam which one can observe in Eq. 4.6, and the normalization factor η is to ensure that $G(\mathbf{k}')$ is between zero

and one.

$$\eta = \max\left(\left|\frac{E_{\text{in}}(\mathbf{k}')}{F(\mathbf{k}')}\right|\right) \tag{4.5}$$

As seen from the grating profile in Eq. 4.2, the outgoing beam from the DMD is composed of three diffraction orders. The beam profile in the image plane is

$$\begin{aligned} E_{\text{IP}}(\mathbf{x}') &= \mathcal{F}^{-1}[(E_{\text{in}}(\mathbf{k}')G(\mathbf{k}'))] \\ &= \eta \left(\frac{1}{4} f(\mathbf{x}' + \mathbf{x_0}') \right. \\ &\quad + \frac{1}{4} f^*(-(\mathbf{x}' - \mathbf{x_0}')) * \mathcal{F}^{-1}[\mathrm{e}^{\mathrm{i}(2\Phi_{\text{in}}(\mathbf{k}'))}] \\ &\quad \left. + \frac{1}{2}\mathcal{F}^{-1}[|F(\mathbf{k}')|\mathrm{e}^{\mathrm{i}\Phi_{\text{in}}(\mathbf{k}')}] \right), \end{aligned} \tag{4.6}$$

where, we have used Eq. 4.3-4.4. The first term in (Eq. 4.6) represents the $m = -1$ diffraction order, and is independent of the aberration phase. This produces the target image profile with high precision. The second term corresponds to $m = 1$ diffraction order, and suffers twice the phase aberration. The third term corresponds $m = 0$ diffraction order or the 'carrier', and suffers from the aberrations as well. Note that by replacing $\Phi(\mathbf{k}') - \Phi_{\text{in}}(\mathbf{k}')$ by $-\Phi(\mathbf{k}') + \Phi_{\text{in}}(\mathbf{k}')$ in Eq. 4.2, we can make the $m = 1$ order aberration free instead. Our choice of $m = -1$ is motivated by the higher grating efficiency (corresponding to the blazing condition, discussed later) for this order.

However, each DMD micromirror provides us with local binary control over the amplitude of light. Hence, we need to binarize the greyscale hologram, $G(\mathbf{k}')$ before displaying it on the DMD. Unfortunately, binarization is a highly nonlinear process and necessarily introduces additional errors. Our IFTA finds a binary grating function $G_{\text{b}}(\mathbf{k}')$ to approximate the greyscale grating $G(\mathbf{k}')$ such that the errors in the image plane are kept at a minimum within a signal window $\mathcal{D}$. The flow chart of the algorithm is shown in Fig. 4.1. We begin the loop with a greyscale hologram $G(\mathbf{k}')$ and binarize the hologram with a binarization operator U_t. We adopt a dynamic-threshold binarization similar to Wyrowski (1989) [70], for a fast convergence to the target image plane profile. The binarization proceeds as follows,

$$G_{\text{b}}^{(i)}(\mathbf{k}') = U_t[G^{(i)}(\mathbf{k}')] = \begin{cases} 0 & \text{if} \quad \text{Re}[G^{(i)}(\mathbf{k}')] < t \\ 1 & \text{if} \quad \text{Re}[G^{(i)}(\mathbf{k}')] > (1-t) \\ \text{Re}[G^{(i)}(\mathbf{k}')] & \text{otherwise} \end{cases} \tag{4.7}$$

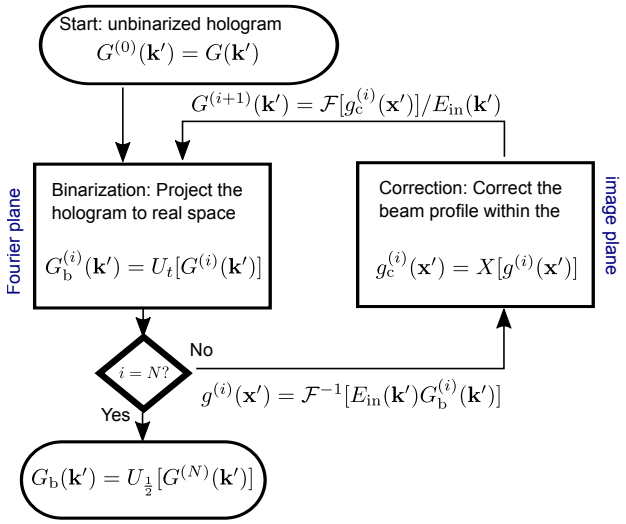

Figure 4.1: The flowchart of our iterative Fourier transform algorithm.

where t is the threshold. The threshold t is dynamically changed with the iteration number i as

$$t = \frac{i}{2N}, \tag{4.8}$$

where N is the total number of iterations. The image plane profile $g(x')$ is obtained from this binarized hologram and suffers from binarization errors. Next, we correct the beam profile within the signal window $\mathcal{D}$ to remove the binarization error with the correction operator X, as

$$g_c^{(i)}(\mathbf{x}') = X[g^{(i)}(\mathbf{x}')] = \begin{cases} g(\mathbf{x}') & \text{if} \quad \mathbf{x}' \in \mathcal{D} \\ g^{(i)}(\mathbf{x}') & \text{otherwise} \end{cases} \tag{4.9}$$

where $g(\mathbf{x}') = \mathcal{F}^{-1}[E_{in}(\mathbf{k}')G(\mathbf{k}')]$ is the beam profile at the image plane created with greyscale grating. Note that $g(\mathbf{x}') = f(\mathbf{x}' - \mathbf{x_0}')$ (i.e. the ideal target profile) within the signal window if the contributions from other diffraction orders in Eq. 4.6 are negligible, as is the case in our experiments. It is worth emphasizing that the input beam profile $E_{in}(\mathbf{k}')$ must be included during the Fourier and inverse Fourier transforms in IFTA (Fig. 4.1) to achieve a low error, especially in presence of aberrations. This results from the fact that aberrations broaden the point-spread function in the image plane and thus destroy the sharpness of the signal window leading to larger errors.

Power Scaling Factor for Improving Power Efficiency

Shown in Eq. 4.6, the diffraction efficiency of the $m = -1$ order is given by $(\frac{1}{4})^2$. However, we are able to further improved the power efficiency by scaling up the target field with $s = \frac{4}{\pi}$ during the IFTA binarization process. This can be implemented by a modified correction operator X' as

$$g_c^{(i)}(\mathbf{x}') = X'[g^{(i)}(\mathbf{x}')] = \begin{cases} sg(\mathbf{x}') & \text{if} \quad \mathbf{x}' \in \mathcal{D} \\ g^{(i)}(\mathbf{x}') & \text{otherwise} \end{cases} \tag{4.10}$$

The corrected beam profile is scaled with a scaling factor s within the signal window $\mathcal{D}$.

This new improvement is based on the fact that for a square wave $x(t)$ its fundamental mode $\sin(\omega t)$ can have a coefficient greater than 1.

$$x(t) = \frac{4}{\pi} \sum_{k=1}^{\infty} \frac{\sin((2k-1)\omega t)}{2k-1} \tag{4.11}$$

$$= \frac{4}{\pi} \left(\sin(\omega t) + \frac{1}{3}\sin(3\omega t) + \frac{1}{5}\sin(5\omega t) + ... \right) \tag{4.12}$$

Even though DMD can have binarized control on the grating amplitude (0 1), a higher modulation level can be achieved.

Improvements over Prior Works

With the new improvement, the power of the signal can be enhanced by $(\frac{4}{\pi})^2 \approx 1.6$ times, which also effectively improves the signal-to-noise background ratio. Higher power scaling factor may be possible with small signal window size, but it often leads to artifacts within the signal window.

Our algorithm is based on Wyrowski (1989)[70] with two significant modifications. First, we introduce phase constraints at the image plane, making the algorithm suitable for QIP experiments requiring optical phase control[64, 12]. Second, we incorporate the ability to account for aberrations and non-uniform illumination in the Fourier plane. Third, we introduce a power scaling factor to improve the power efficiency of the signal beam.

4.3 Experimental Setup

Shown in the Fig. 4.2 is the experimental setup for holographic beam shaping. The s-polarized 369.5 nm output beam from the fiber is expanded by the collimation lens L1

to a 5 mm ($1/e^2$ intensity radius) Gaussian beam illuminating a circular aperture on the DMD (Texas Instruments DLP9500UV) at an incident angle of approximately 24°. The DMD is placed in the Fourier plane (FP) of a focusing lens L2 ($f = 200$ mm). In order to maintain the polarization and power stability of the beam, a two-fold approach is employed. A polarizer is used to filter the beam's polarization, while power stability is achieved by utilizing feedback from the photodiode signal of the sampled beam.

The micromirror pitch of the DMD is $d = 10.8\,\mu$m and each micromirror can be toggled between two angles, behaving like a local binary light-switch. A binary amplitude grating (with periodicity $a = 4d = 43.2\ \mu$m) is employed to modulate both the phase and amplitude of the electric field of light, E_{FP} in the DMD plane (FP), such that the target electric field profile in the image plane E_{IP} (with IP referring to either IP1 or IP2, shown in Fig. 4.2) can be generated with high accuracy. A pinhole placed in the image plane (IP1) of L2 allows us to choose a specific diffraction order ($m = -1$ here) of the DMD binary grating to propagate to the $^{174}\mathrm{Yb}^{+}$ ion.

A flip mirror can direct the light onto a camera C1 to monitor the optical intensity profile and characterize aberrations at IP1. A photo-multiplier tube (PMT) is used to detect fluorescence from the ion. The DMD beam is introduced into the fluorescence-imaging path through a pellicle beam splitter. Ion-addressing and fluorescence collection are achieved using a 0.2NA shared homemade microscope objective and an imaging lens L3. The effective focal length between the DMD FP and IP2 is 24 mm. Here, we choose a coordinate system convention where the beam is propagating along the $z-$direction.

4.4 Results: Aberration Correction

To realize diffraction-limited performance at an image plane, we first characterize the aberration phase map $\Phi_{\mathrm{ab}}^{(\mathrm{IP})}(\mathbf{x})$, following a similar approach as in Zupancic, et al. (2016)[75], schematically shown in Figs. 4.3-4.4.

Note that the result presented in 4.4 is with a setup that is different from the setup described in 4.2. The beam splitter is a polarization beam splitter rather than a pellicle beam splitter, the numerical aperture is 0.12 rather than 0.2, and we use a camera rather than a PMT to collect the fluorescence.

More detailed information about this setup can be found in Shih, et al. (2021)[62], and we upgraded the setup to the one shown in 4.2 to achieve a higher numerical aperture and increase the transmission in photon collection.

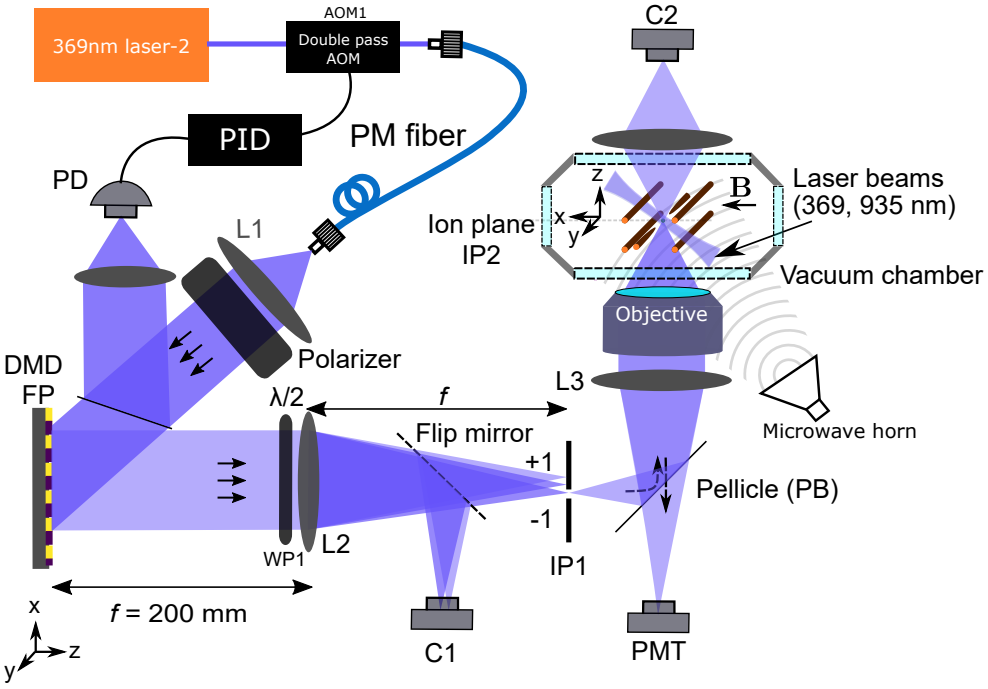

Figure 4.2: Experimental Setup

We let the light from two FP patches (Figs. 4.3a and 4.4a), centred at $\mathbf{x} = \mathbf{0}$ (centre of the FP aperture) and $\mathbf{x} = \mathbf{\Delta}$, consisting of a small number of DMD micromirrors, interfere in the image plane IP. The interference fringes are measured on the camera C1 for IP1 (Fig. 4.3b) or with the ion for IP2 (Fig. 4.4b) for extracting the aberration phase $(\Phi_{\mathrm{ab}}^{(\mathrm{IP})}(\mathbf{\Delta}) - \Phi_{\mathrm{ab}}^{(\mathrm{IP})}(\mathbf{0}))$ (see Appendix A).

To measure the interference fringes with an ion, we use the ion as an point-like detector to extract the local intensity information of the beam. This can be done in multiple manners. The most straightforward one is using the fluorescence emitted from the ion, and this is the approach we used in Shih, el al. (2021)[62]. However, this approach suffers from undesired scattering from the Vacuum window and the microscope objective, as the photon collection and the individual addressing shares the same optical beam path, which leads to a low signal-to-noise ratio.

Instead, we came up with an alternative approach to quantify the intensity of the light falling on the ion. In this approach, we initialize the ion in the bright state $|1\rangle$, and use the optical pumping beam instead of the detection beam for the DMD beam, and later measure the population (with the ion fluorescence) of the ion in bright state $|1\rangle$ and the

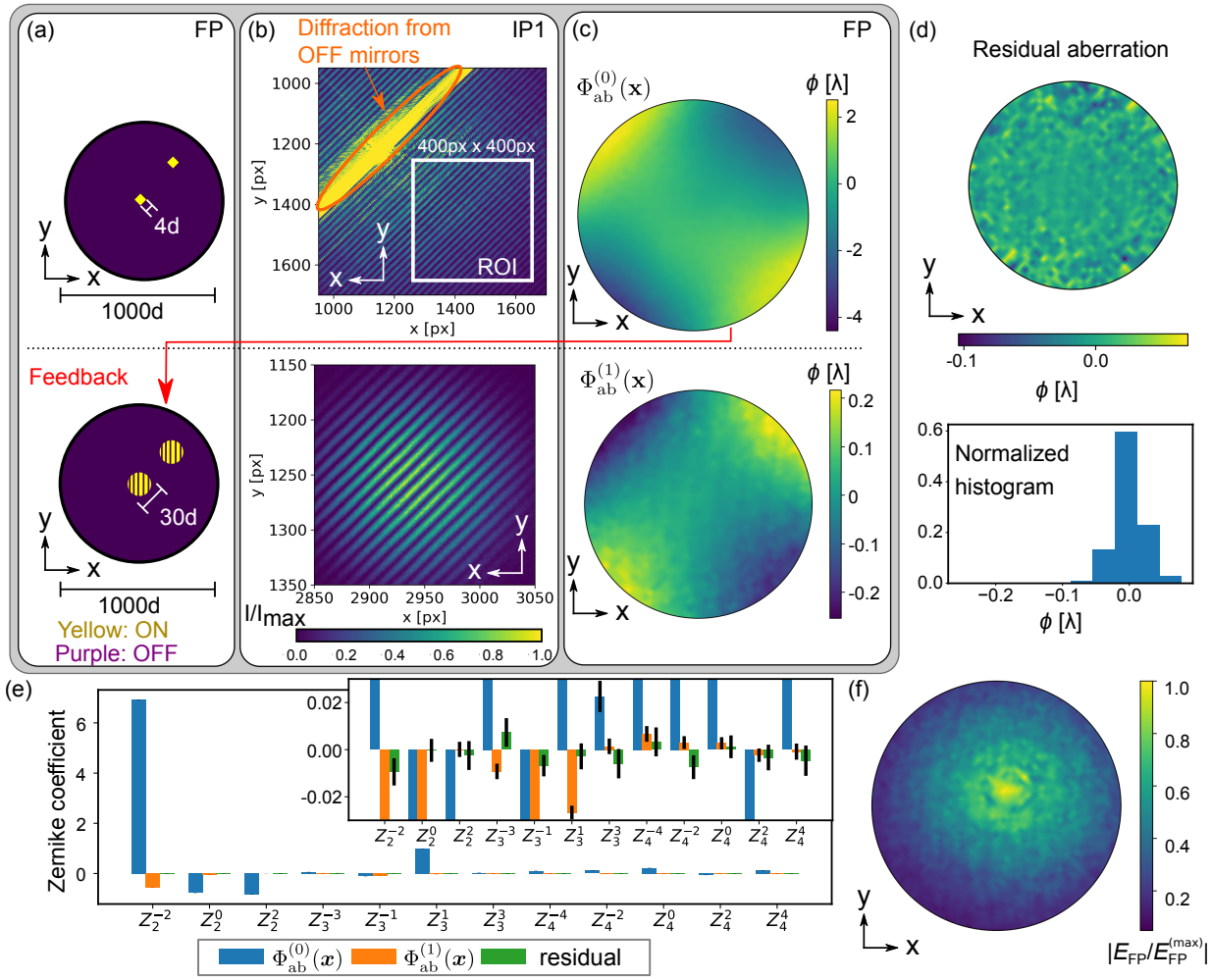
(a)
FP
4d
1000d
Feedback
30d
1000d
Yellow: ON
Purple: OFF
(b)
Diffraction from OFF mirrors
IP1
400px x 400px
ROI
y [px]
x [px]
I/Imax
(c)
FP
$\Phi_{ab}^{(0)}(x)$
$\Phi_{ab}^{(1)}(x)$
ϕ [λ]
(d)
Residual aberration
ϕ [λ]
Normalized histogram
(e)
Zernike coefficient
residual
(f)
$|E_{FP}/E_{FP}^{(max)}|$

dark state $|0\rangle$ to extract the local intensity information of the DMD beam. The fluorescence collection happened at a different timing, and thus the undesired scattering does not affect measurement. In addition, this approach is highly sensitive as it only takes in average a few photons to pump the ion from the bright state to the dark state, and thus greatly reduce the power requirements of the beam. This is the approach we used in Motlakunta, et al. (2023)[50], and the results are shown in Section 4.4.2.

With the central patch as a reference, we vary Δ to scan the FP aperture on a grid in steps of d_g to reconstruct the aberration phase map, after unwrapping the phases[66] and interpolating between the grid lines. The FP patch sizes are chosen to get a good signal-to-noise ratio, while making sure that the optical phase does not vary appreciably ($\ll 2\pi$) within a patch.

4.4.1 Aberration Characterization with Fluorescence Count

We choose the patch size empirically, such that the standard error in the ion fluorescence signal is approximately ten times smaller than the fringe contrast (Fig. 3b). This leads to about $\lambda/50$ uncertainty in phase estimation.

We characterize the total aberrations in terms of three phase maps: $\Phi_{ab}^{(0)}(\mathbf{x})$, $\Phi_{ab}^{(1)}(\mathbf{x})$, and $\Phi_{ab}^{(2)}(\mathbf{x})$, such that $\Phi_{ab}^{(IP1)}(\mathbf{x}) = \Phi_{ab}^{(0)}(\mathbf{x}) + \Phi_{ab}^{(1)}(\mathbf{x})$ and $\Phi_{ab}^{(IP2)}(\mathbf{x}) = \Phi_{ab}^{(0)}(\mathbf{x}) + \Phi_{ab}^{(2)}(\mathbf{x})$.

Figure 4.3 *(preceding page)*: **Aberration characterization and compensation up to IP1. (a)-(c)** describe the characterization of aberration phase maps $\Phi_{ab}^{(0)}(\mathbf{x})$ (top row) and $\Phi_{ab}^{(1)}(\mathbf{x})$ (bottom row). **(a)** DMD FP patches, as defined in the text. **(b)** Corresponding interference fringes at IP1, measured by the camera C1. The diffraction pattern from the OFF micromirrors (see Supplementary information) limits the region of interest (ROI) for phase extraction. Note that the two interference fringes are located at different positions on the camera C1. This is because a non-zero diffraction angle of the $m = -1$ order translates to a spatial offset of the beam at IP1. **(c)** Interpolated and unwrapped measured phase profiles (piston and tilts removed) reconstructed from respective interference fringes. **(d)** The measured residual aberration map without piston and tilt components and its histogram after correcting for $\Phi_{ab}^{(0)}(\mathbf{x})$ and $\Phi_{ab}^{(1)}(\mathbf{x})$. The histogram is based on re-sampled data from the interpolated phase map at each micromirror position. **(e)** First few Zernike coefficients of $\Phi_{ab}^{(0)}(\mathbf{x})$, $\Phi_{ab}^{(1)}(\mathbf{x})$, and the residual aberration. The error bars indicate the standard deviation from error propagation **(f)** The amplitude profile of the beam (scaled to the maximum amplitude, see Methods) illuminated on the DMD.

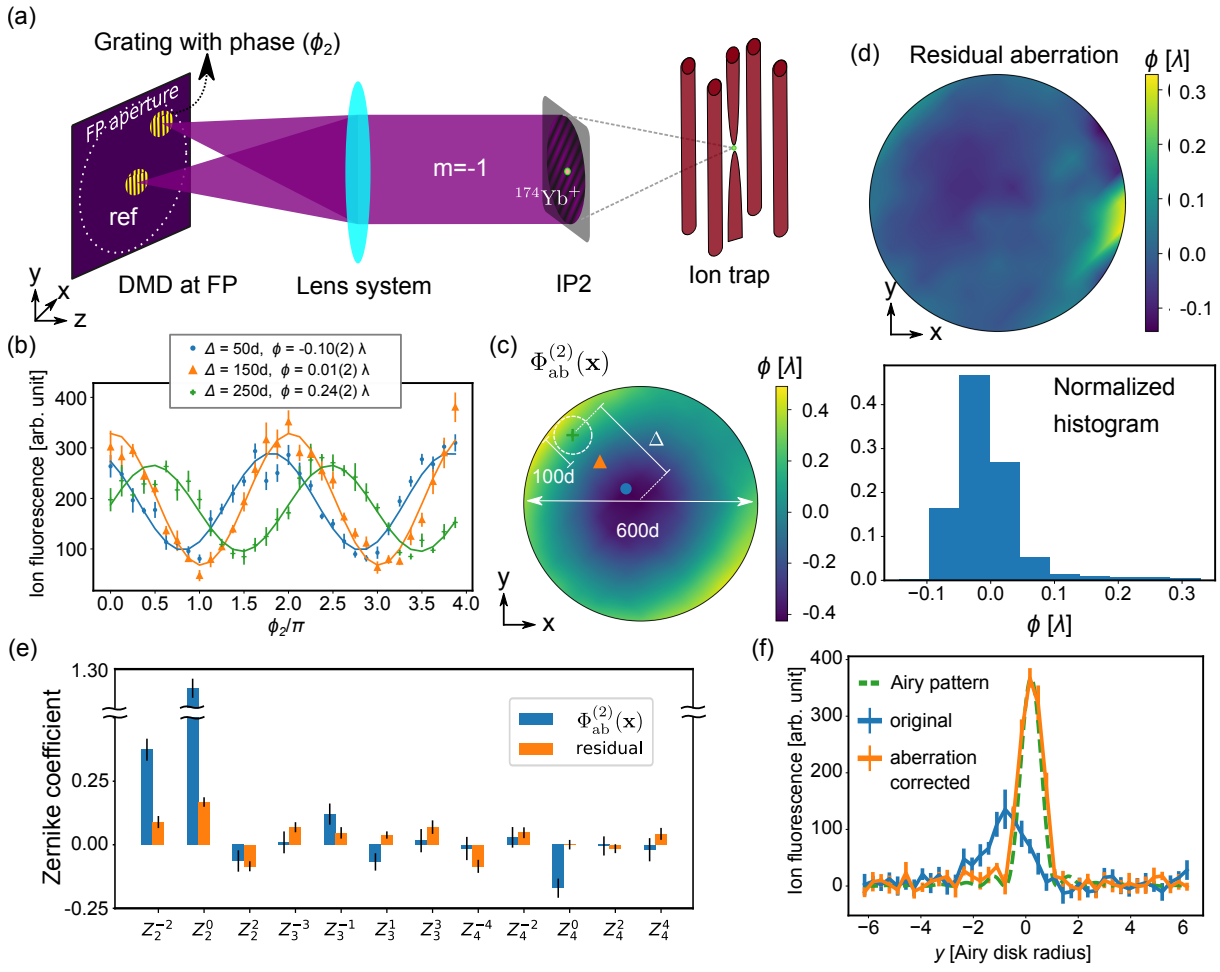
(a)
Grating with phase (ϕ_2)
FP aperture
ref
m=-1
$^{174}Yb^+$
DMD at FP
Lens system
IP2
Ion trap
(b)
Δ = 50d, ϕ = -0.10(2) λ
Δ = 150d, ϕ = 0.01(2) λ
Δ = 250d, ϕ = 0.24(2) λ
Ion fluorescence [arb. unit]
ϕ_2/π
(c)
$\Phi^{(2)}_{ab}(\mathbf{x})$
Δ
100d
600d
ϕ [λ]
(d)
Residual aberration
ϕ [λ]
Normalized histogram
ϕ [λ]
(e)
Zernike coefficient
$\Phi^{(2)}_{ab}(\mathbf{x})$
residual
(f)
Ion fluorescence [arb. unit]
Airy pattern
original
aberration corrected
y [Airy disk radius]

The measured phase maps are shown in Fig. 4.3c and Fig. 4.4c respectively, and the measured residual aberration phase maps after aberration correction are shown in Fig. 4.3d and Fig. 4.4d.

The phase map $\Phi_{\mathrm{ab}}^{(0)}(\mathbf{x})$ characterizes a majority of the total aberrations from the source up to IP1 with high precision. For this, we turn on all the micromirrors within the two patches (4×4 micromirrors each), as shown in Fig. 4.3a (top), and choose a grid size $d_{\mathrm{g}} = 20d$. We measure about 6.5λ (13π) peak-peak and $1.13(2)\lambda$ RMS phase aberrations (Fig. 4.3c top), dominated by astigmatism (Zernike coefficient Z_2^{-2}), as seen in Fig. 4.3e. In this manuscript, all phase aberration-specifications are reported after removing the 'piston' (Z_0^0) and 'tilt' terms (Z_1^{-1} and Z_1^1), as piston is an inconsequential global phase, and tilts can be easily fixed by tilting a mirror placed in an FP.

The phase map $\Phi_{\mathrm{ab}}^{(1)}(\mathbf{x})$ characterizes additional aberrations, up to IP1, caused by the

---

Figure 4.4 *(preceding page)*: **(a)** Schematic of aberration measurement with a single $^{174}\mathrm{Yb}^+$ ion in a 'four-rod' trap. **(b)** Interference fringes measured by observing the $^2S_{1/2} - {}^2P_{1/2}$ fluorescence of the ion. For each value of the phase ϕ_2 of the scanning grating patch, in steps of $\pi/8$ from 0 to 4π (with the redundancy for a robust phase extraction), we acquire the fluorescence for 100 ms. The 369.5 nm light is red-detuned by approximately 20 MHz from resonance, for maximizing the signal-to-noise ratio while Doppler-cooling the ion. We estimate the peak optical intensity of the fringes on the ion to be about $0.5I_{\mathrm{sat}}$, where I_{sat} is the saturation intensity. Each data point is an average over 5 identical experiments, and error bars represent the standard error. Each solid line is a cosine wave at a fixed angular frequency of 1, reconstructed from the amplitude and phase ϕ obtained from fast Fourier Transform (FFT) of the data set. **(c)** The aberration phase map $\Phi_{\mathrm{ab}}^{(2)}(\mathbf{x})$ (corresponding scanning patches for plots in **b** are superimposed). **(d)** The residual aberration phase map and normalized histogram (with the same method in Fig. 4.3b) after aberration compensation. **(e)** First few Zernike coefficients of $\Phi_{\mathrm{ab}}^{(2)}(\mathbf{x})$ and the residual aberration, extracted in the same manner as in Fig. 4.3. **(f)** 369.5 nm single-ion addressing beam profile before (blue) and after (orange) the aberration correction, as measured (see Methods) by ion fluorescence. Error bars indicate the standard error over 5 repeated measurements. The beam profile is created by employing a grating over the entire FP aperture (diameter $600d$), without any amplitude modulation. We scan the beam on the ion by adding a programmable tilt in the phase map. The spatial location of the beam (horizontal axis) at the ion is calculated from the known value of the tilt and the effective focal length. The effective NA here is 0.08 (the ideal Airy pattern shown), corresponding to an Airy radius of 2.8 μm.

non-zero diffraction angle of the $m = -1$ order of the DMD hologram. For this, we employ the binary grating ($a = 4d$), pre-compensated for $\Phi_{\text{ab}}^{(0)}(\mathbf{x})$, within two circular FP patches of diameter $d_p = 30d$ each, as shown in Fig. 4.3a (bottom) and choose the grid size $d_{\text{g}} = 25d$. We measure about 0.45λ peak-peak and $0.09(1)\lambda$ RMS phase in $\Phi_{\text{ab}}^{(1)}(\mathbf{x})$ (Fig. 4.3c bottom), validating our assumption that $\Phi_{\text{ab}}^{(0)}(\mathbf{x})$ characterizes the majority of aberrations. This $\Phi_{\text{ab}}^{(1)}(\mathbf{x})$ is again dominated by astigmatism (Z_2^{-2}) which is the primary aberration (except the tilt) from an angled beam. We find that the residual aberrations up to IP1 (Fig. 4.3d), after compensating for $\Phi_{\text{ab}}^{(0)}(\mathbf{x})$ and $\Phi_{\text{ab}}^{(1)}(\mathbf{x})$, is 0.014λ RMS (0.15λ peak-peak) which falls below the standard error of 0.025λ.

The phase map $\Phi_{\text{ab}}^{(2)}(\mathbf{x})$ is measured with fluorescence from the ion, which behaves as a point detector because it is well-localized (estimated to be approximately 130 nm RMS at Doppler cooling temperature) compared to the diffraction limit of 2.8 μm. Instead of moving the ion, we scan the phase difference (ϕ_2 in Fig. 4.4b) between the two circular FP grating patches ($d_{\text{p}} = 100d$, $a = 4d$, $d_{\text{g}} = 50d$) to move the interference fringes across the ion. The 0.9λ peak-peak and $0.20(1)\lambda$ RMS aberrations in $\Phi_{\text{ab}}^{(2)}(\mathbf{x})$ are compensated to a residual aberration of $0.05(2)\lambda$ RMS (Fig. 4.4d), resulting in a diffraction-limited spot at the ion, as demonstrated by measuring the beam profile using ion fluorescence in Fig. 4.4f.

The residual aberrations in both IP1 (Fig. 4.3d) and IP2 (Fig. 4.4d) are lower than standard manufacturing tolerance of precision lenses (typically $\lambda/10$ at 633 nm).

4.4.2 Aberration Characterization with Quantum Sensing

Comparing to the fluorescence method in Section 4.4.1, we have some modifications to the parameters.

We are able to use a smaller patch size of $25d$ and a smaller grid size of $25d$ to characterize the aberrations to better characterize the local aberrations. In addition, we are able to characterize a wider range of the Fourier plane from $600d$ to $900d$. Using a smaller patch will diffract less light and has a larger spread at the ion image plane both result in a lower intensity. This was not previously possible with the fluorescence method because the ion fluorescence signal from the smaller patches will be too weak to be detected.

As for characterizing the aberrations at the edge of Fourier plane, the intensity of patches at the edge are lower and consequently creates interference fringes with lower contrast. One can notice that in Fig. 4.4b the contrast of the fringes decreases as the patch moves away from the center. The quantum sensing method is able to characterize

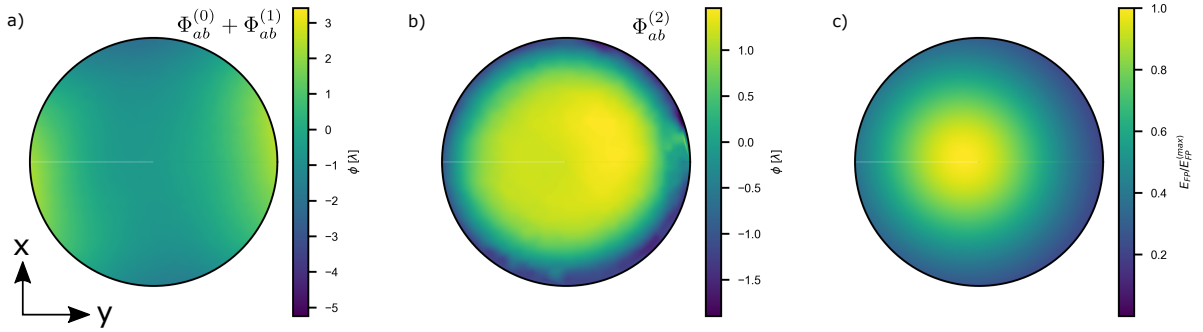

Figure 4.5: **FP phase and amplitude profile. a.** The aberration phase profile was measured using camera C1. **b.** The aberration phase profile is measured using the ion at IP2. For a-b, the piston and tilt terms are removed from the measured phase profiles, and the profile is further smoothened and interpolated. **c.** The scaled amplitude profile measured at IP2. The measured amplitude profile is smoothened, interpolated, and fit to 2D Gaussian.

the fringes with lower contrast because the new method immune to the undesired scattering and thus has a higher signal-to-noise ratio.

Shown in Fig. 4.5b, we presented the aberration characterized with the new method, and along with the amplitude profile of the beam at the FP. The aberration from IP1 to IP2 $\Phi_{\text{ab}}^{(2)}(\mathbf{x})$ are measured with the ion. It has a peak-to-peak value of 3λ.

We also use the ion to characterize the Fourier amplitude profile. For this, we only turn on the scanning patch without using the reference patch the center. The diffracted beam will not have the interference fringes and its intensity is measured with the same population transfer from $|1\rangle$ to $|0\rangle$. The scaled amplitude profile is presented in 4.5c.

4.5 Results: High Precision Individual Ion Addressing

With the aberration profile characterized, we are able to incorporate it in the hologram generation algorithm to compensate for the aberrations to achieve high precision individual ion addressing.

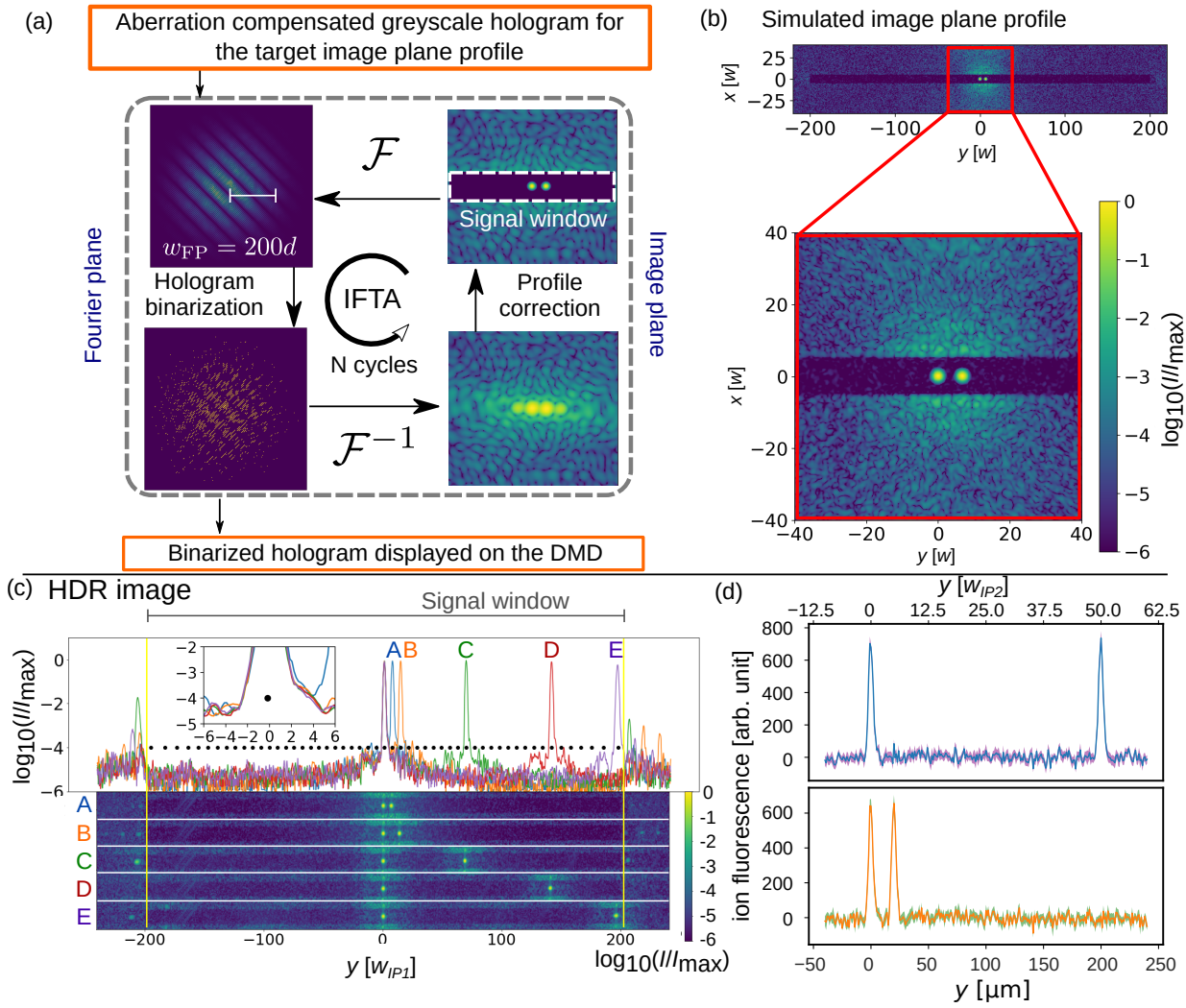
(a)
Aberration compensated greyscale hologram for the target image plane profile
$w_{\mathrm{FP}} = 200d$
Hologram binarization
IFTA
N cycles
Profile correction
Signal window
Fourier plane
Image plane
Binarized hologram displayed on the DMD
(b)
Simulated image plane profile
x [w]
y [w]
log10(I/Imax)
(c)
HDR image
Signal window
A
B
C
D
E
log10(I/Imax)
y [w_IP1]
(d)
y [w_IP2]
ion fluorescence [arb. unit]
y [μm]

In Fig. 4.6a-b, we schematically describe our iterative Fourier transformation algorithm (IFTA) and show a numerical simulation for creating a pair of Gaussian spots. More details of the algorithm can be found in Sec. 4.2.3

The IFTA strives to minimize errors only inside a user-defined 'signal window' in the image plane. A suitable spatial filter placed in IP1, such as a rectangular aperture, shields the ion chain from erroneous signals outside this signal window.

Figure 4.6c shows experimental data taken with camera C1 in IP1 of pairs of Gaussian spots suitable for simultaneously addressing arbitrary pairs of ions with non-uniform spacing.

A relative intensity crosstalk error below 10^{-4} is achieved at a distance of approximately $4w_{\mathrm{IP1}}$ within a $400w_{\mathrm{IP1}} \times 10w_{\mathrm{IP1}}$ signal window, where w_{IP1} is the spot size of the addressing Gaussian beam, limited by the numerical aperture. Crucially, this low error rate is maintained over a large signal window of length approximately $400w_{\mathrm{IP1}}$. This suggests that the low error window can fit up to $400w_{\mathrm{IP1}}/4w_{\mathrm{IP1}} = 100$ ions.

Figure 4.6 *(preceding page)*: **(a)** Illustration of the iterative Fourier transformation algorithm (IFTA) for programming holograms to create two Gaussian spots. We first binarize the ideal, aberration-corrected, and greyscale hologram (from Eq.4.1, which has a Gaussian envelope of width $w_{\mathrm{FP}} = 200d$) by setting a dynamic threshold on each mirror. The Fourier transformed profile in the image plane differs from the target profile due to this binarization. We numerically fix this error within a user-defined signal window at the image plane, by substituting the field profile with the target profile. The inverse Fourier transform of this modified profile results in another grey-scale hologram which will be binarized again in the next iteration. We iterate this procedure to achieve the numerical accuracy of the electric field within a small error of the target profile ($N = 2000$ iterations here). **(b)** Numerical simulation of two Gaussian addressing beams at the image plane with a binary hologram created by IFTA. **(c)** Intensity profile of Gaussian spots ($w_{\mathrm{IP1}} = 10\ \mu$m) measured by the camera C1 at IP1 suitable for addressing various pairs (A through E) in a chain of 53 $^{174}\mathrm{Yb}^{+}$ ions. Expected equilibrium positions of ions are represented by black dots and superimposed on the image (with 30x magnification). The top panel shows a cross-section of the signal window (a close-up shown in the inset) from the high dynamic range (HDR) images shown in the bottom panel. Each HDR image is composed of 5 images with exposure times varying in steps of 10x from 120 μs to 1.2 s. **(d)** Fluorescence signal (see Methods) of an $^{174}\mathrm{Yb}^{+}$ ion when illuminated by an addressing beam profile consisting of two Gaussian spots of waist $w_{\mathrm{IP2}} = 4\ \mu$m each. The beam is scanned on the ion identically as in Fig. 4.4f, and the shaded region indicates the standard error.

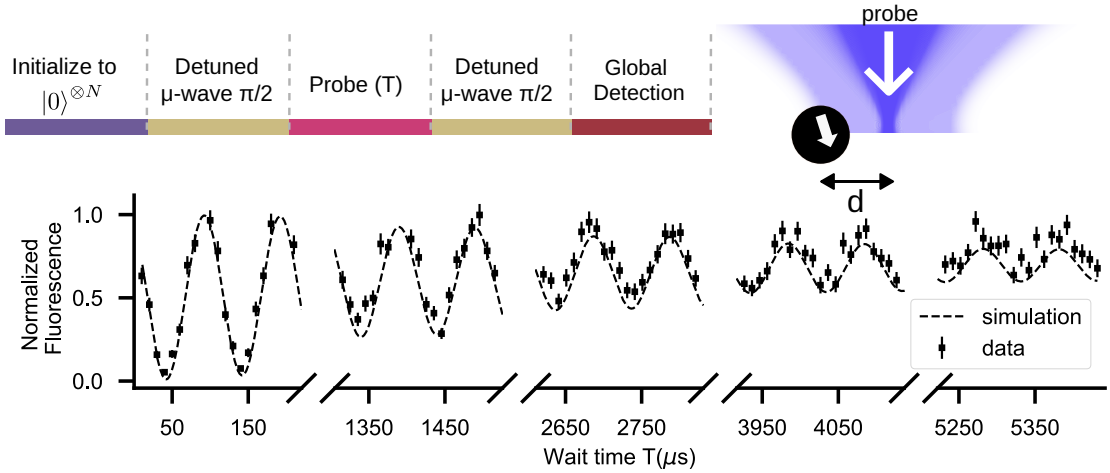

Figure 4.7: **Ramsey spectroscopy under exposure to the decoherence probe beam from the DMD.** This is measured with a single ion (N=1) in the trap. The ions are initially set to the $|0\rangle$ state, and then prepared in the superposition state $(|0\rangle + |1\rangle)/\sqrt{2}$ with a microwave $\pi/2$ rotation. The probe beam is applied for a duration T, after which a microwave $\pi/2$ rotation is applied to the ion. The center of the beam is deviated from the ion by a distance d. The contrast of the Ramsey will decrease exponentially. The characteristic time of this exponential decay is the coherence time of the superposition state, which corresponds to the decoherence time of the probe beam.

In Fig. 4.6d, we demonstrate high-quality optical addressing by directly observing ion-fluorescence at the centre of the image plane IP2, while scanning the addressing beam along y between the centre and the edge of a $120w_{\mathrm{IP2}} \times 10w_{\mathrm{IP2}} = 480\ \mu\mathrm{m} \times 40\ \mu\mathrm{m}$ signal window. While our measurements are limited by the signal-to-noise ratio of ion fluorescence (see Methods) on camera C2, we expect the low error rates to be transmitted to IP2. This is because, astigmatism (leading aberration) at a field point 240 μm away from the center of IP2 is independently estimated (using Zemax Optics Studio) to be about 0.02 in terms of the standard Zernike coefficient, smaller than the demonstrated aberration correction limit in Fig. 4.4e

At the intermediate image plane, we can characterize the crosstalk multiple orders of magnitude smaller than the signal using high dynamic range (HDR) imaging. However, the noise from fluorescence measurement limits us from doing the same. Instead, we resort to quantum sensing to properly characterize the crosstalk error at image plane IP2.

Rather than using the scheme we used in 4.4, which uses population transfer from $|1\rangle$ to $|0\rangle$ to characterize the intensity of the crosstalk, we use Ramsey measurements to extract

local intensity information. The timing sequence of the protocol is as follows:

1. Initialized the ion in $|0\rangle$ state.
2. We first prepare the ion in the superposition state $(|0\rangle + |1\rangle)/\sqrt{2}$ with a microwave $\pi/2$ rotation. (See section 2.5.1)
3. Wait for some time T while applying the probe beam from the DMD.
4. Apply another microwave $\pi/2$ rotation to the ion.
5. Measure the fluorescence of the ion.

We vary the probe duration T, and fit the measured fluorescence to the following function:

$$\begin{aligned} f(T)_{T_2,\alpha,\beta,\phi,C} = &\sin^2(\omega T)(\alpha e^{-T/T_2}) \\ &+ \beta(1 - e^{-T/T_2}) + C \end{aligned} \tag{4.13}$$

Here, ω is the detuning of the microwave frequency from the energy splitting between $|1\rangle$ and $|0\rangle$. α, β, and C are fitting parameters. T_2 is the characteristic time of the exponential decay of the fringe contrast, which is the coherence time of the superposition state. The intensity of the DMD probe beam is inversely proportional to T_2.

In the rest of the chapter, we will refer to the characteristic time of the Ramsey contrast decay as T_2, and the characteristic time of the population transfer as T_1.

The reason we do not use spin population transfer is that its rate doesn't always scale linearly with the intensity of the probe beam. This can lead to inaccurate estimation of the crosstalk error, as the probe beam and the crosstalk have multiple orders of magnitude difference in intensity.

The spin reset and detection process would saturate as the power of the addressing beam increases, due to the finite lifetime of the ion in the $^2P_{1/2}$ excited state. Nevertheless, the decoherence from collapsing the quantum state is not limited by power saturation.

As shown in Fig. 4.8, we demonstrate the rate of decoherence $1/T_2$ at various separations between the DMD probe beam and the target ion. This reveals that we are able to achieve about a 10^{-4} level of crosstalk.

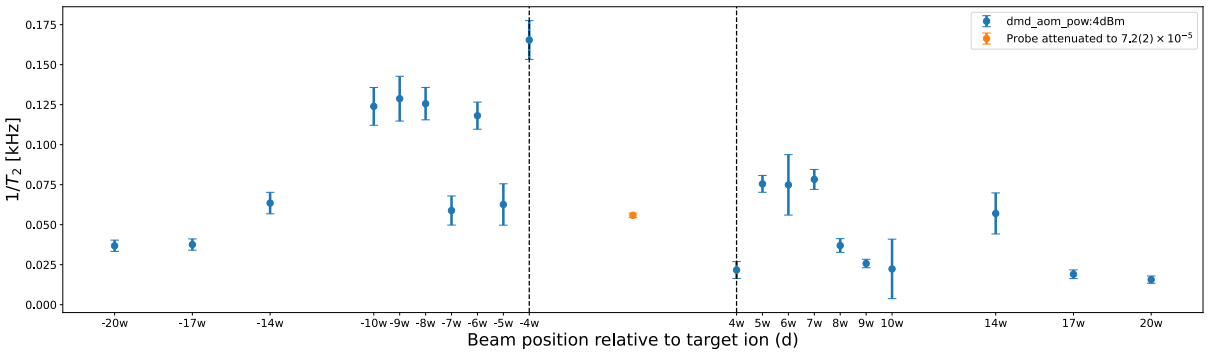

Figure 4.8: Intensity of crosstalk at the ion location. We measured the intensity by determining the decoherence time T_2. The intensity is proportional to $1/T_2$. We measured the intensity at various distances between the DMD probe beam and the target ion. Additionally, we display the measurement for the attenuated intensity beam directly addressing the ion. The intensity is attenuated by a factor of $7.2(2) \times 10^{-5}$.

4.6 Results: Fidelity in Individual Spin Reset and Measurement

When characterizing how crosstalk corrupts the quantum state of the neighboring ions during spin resets or measurements, there are additional factors to consider:

1. Polarization: σ^+, σ^-, π polarization all contribute to the detection process. However, only π polarization photons can corrupt the quantum state of the neighboring ions, as $|1\rangle$ and $|^2P_{1/2}, F = 0, m_F = 1\rangle$ are coupled via the π photon transition.

2. Power: The spin reset and detection process would saturate as the power of the addressing beam increases, but the decoherence from collapsing the quantum state is not limited by power saturation.

To quantitatively study the fidelity of the individual spin reset and the individual spin measurement process while preserving the quantum state of the neighboring ion, we can define its fidelity $F_{1|2}$ as:

$$F_{1|2} = \frac{2}{3} \exp\left[-\frac{\tau(\text{ion2})}{T_2(\text{ion1})}\right] + \frac{1}{3}. \tag{4.14}$$

where ion 2 is the ion we aim to reset or measure, and ion 1 is the neighboring ion whose quantum state we wish to maintain. τ(ion2) represents the process time during which the resonant probe beam illuminates the process qubit.

The definition of Eq. 4.14 is derived from fidelity metrics[54]:

$$F_{1|2}(t) = \mathrm{tr}\left(\sqrt{\rho(0)^{1/2}\rho(t)\rho(0)^{1/2}}\right) \tag{4.15}$$

This metrics yields the worst value when the ion is initially in the $|1\rangle$ state. With analytically solving the master equation for the worst scenario. The worst-case fidelity for a time T is linked to the Ramsey contrast $R_c(T)$ at the low crosstalk limit.

$$F_{1|2}(T) = \frac{2}{3}R_c T + \frac{1}{3} \tag{4.16}$$

The Ramsey fringes decay exponentially and the equation can this leads to the definition we have in Eq. 4.14.

Further details on solving the master equation for $F_{1|2}$ can be found in Motlakunta et al. (2023)[50].

In Fig. 4.9, we present the calculated $F_{1|2}$ for the spin reset process as a function of the distance between the DMD probe beam and the target ion. We calculate $F_{1|2}$ using Eq. 4.14, and the measured T_2 of the neighboring ion from 4.8. We observe that $F_{1|2}$ surpasses 99.9% for $d \geq 4w$, where w signifies the DMD probe beam's waist. For this experiment, we employ a pure optical pumping beam instead of an optical pumping beam generated by the EOM from the detection beam. More details can be found in section 2.4.

Regarding detection, we present the calculated $F_{1|2}$ for the spin measurement process as a function of the distance between the DMD probe beam and the target ion in Fig. 4.10. With an 11 $\tau = \mu$s detection time, required for high fidelity detection with current state-of-the-art detectors[15], $F_{1|2}$ can exceed 99.6% for $d \geq 4w$.

To maximize $F_{1|2}$, a few considerations are noteworthy:

1. Utilize pure optical pumping instead of using EOM to modulate the detection beam to generate the sideband for the spin reset. This is because the EOM modulation would not be able to deplete the power of the input beam frequency (the carrier). The residual carrier does not contribute to spin reset resonantly, but it could still contribute to accidental quantum measurement.

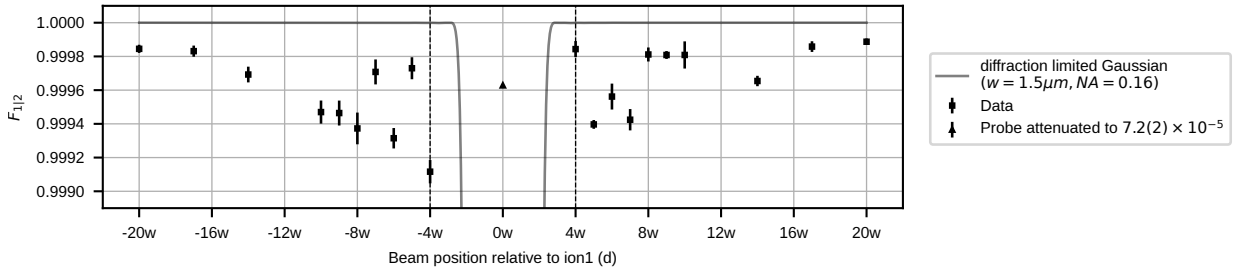

Figure 4.9: **Preservation Fidelity of Ion1 Against State Reset Light Targeted at Ion2 Location.** The $F_{1|2}$ is plotted against the distance d (expressed in multiples of the addressing beam waist w). Here, $w = 1.50(5)$ μm denotes the Gaussian beam waist of the addressing beam. Error bars indicate standard deviation in the $F_{1|2}$ estimation, obtained from 20 bootstrapping repetitions of 200 measurements each. For calibrating crosstalk I_X, we measure $F_{1|2}$ for a probe beam attenuated to a relative intensity of $7.2(2) \times 10^{-5}$ addressing Ion1 (denoted by the triangle marker at $d = 0$). For comparative purposes, $F_{1|2}$ is calculated (represented by the solid gray line) for a diffraction-limited (NA $= 0.16$) Gaussian beam with a beam waist $w = 1.50$ μm. $F_{1|2}$ exceeds 99.9% for $d \geq 4w$. For these measurements, the intensity is $I = 1.25(16)I_{\text{sat}}$, and the π polarization portion is $I_\pi/I = 0.86$ and $\tau = 9.73(7)$ μs.

2. Keep the intensity of the individual probe beam well below the saturation intensity. As the process rate $1/\tau$ in Eq. 4.14 saturates for a targeted fidelity as the time increases, the rate of loss of coherence for the neighboring ion T_2 due to coherence would not.

3. Optimal polarization may not be an equal portion between π, σ^+ and σ^- components. π and $\sigma^{+/-}$ polarization contribute to the decoherence of the neighboring ion differently.

Detailed theoretical analysis and numerical simulation can be found in Motlakunta, et al. (2023)[50].

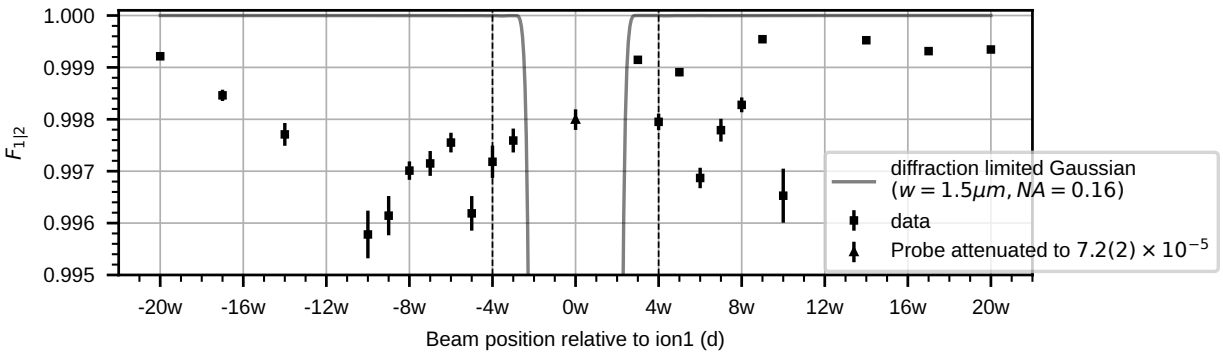

Figure 4.10: **Fidelity of preserving ion1 for detection light at ion2 location.** To compare the crosstalk, we evaluate $F_{1|2}$ with a probe beam addressing Ion1. This beam's relative intensity is attenuated to $7.2(2) \times 10^{-5}$ (denoted by the triangle marker at $d = 0$). For additional context, we calculate $F_{1|2}$ (represented by the solid gray line) using a diffraction-limited (NA=0.16) Gaussian beam with a waist of w. We find that the fidelity $F_{1|2}$ exceeds 99.6% when $d \geq 4w$. The uncertainty in estimating $F_{1|2}$ is represented by error bars, derived from 20 bootstrapping repetitions of 200 measurements each. During this process, we apply a detection probe light with an intensity $I = 1.25(16)I_{\mathrm{sat}}$ for a duration of $\tau_{\mathrm{d}} = 11$ μs.

4.7 Discussion: Scalability

4.7.1 Addressable Image Plane

The maximum number of addressable ions is limited by the addressable range of the DMD, and the spacing between ions relative to its waist. For a Gaussian beam, the $1/e^2$ intensity radius w_{IP} in the image plane is inversely proportional to the radius in the Fourier plane, $w_{\mathrm{IP}} = \frac{\lambda f}{\pi w_{\mathrm{FP}}}$.

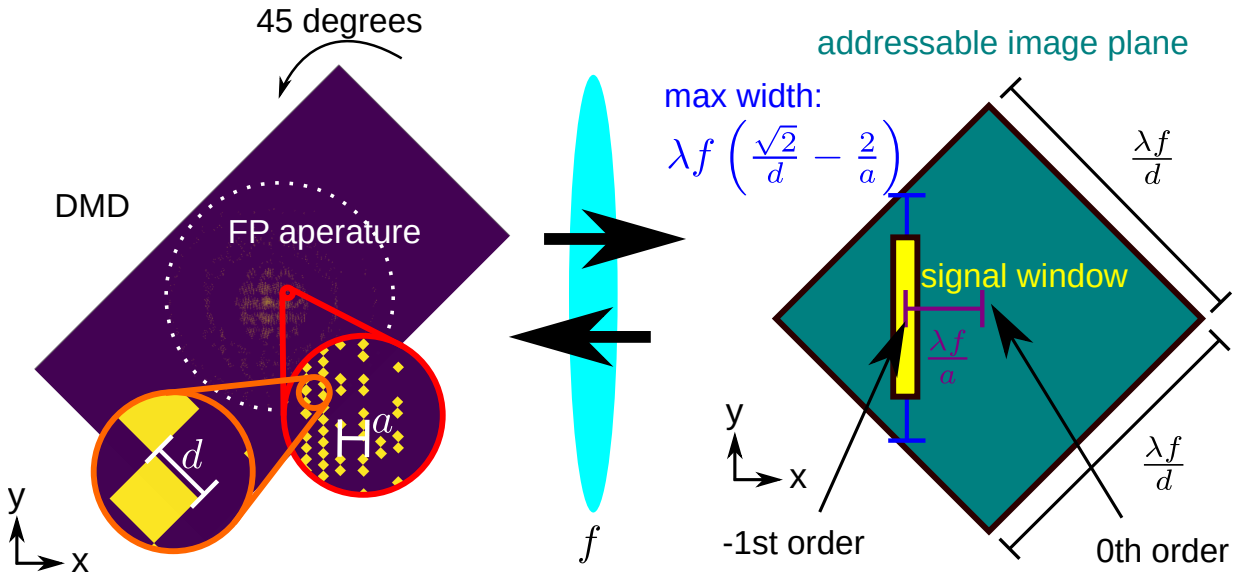

Figure 4.11: **Illustration on the addressable image plane and the signal window.** The signal window must stay within the addressable image plane, and thus its size is limited.

As Fig. 4.11 shows, the maximum addressable image plane is determined by the Nyquist limit $\frac{\lambda f}{2d}$. Here, d is the edge length of each mirror, and the beam profile and the signal window must be contained within it. In our setup, the periodicity is $a = 4d$ making the maximum width of the signal window $\lambda f\left(\frac{\sqrt{2}}{d}-\frac{2}{a}\right) \approx 0.9\frac{\lambda f}{d}$. We choose this to be about $0.6\frac{\lambda f}{d}$ while doing the experiment in order to fit the full image in C1. Numerical simulations show that the degradation in accuracy by extending the signal window towards the edge is marginal. The separation between $m = -1$ order and the $m = 0$ order beams depends on the periodicity of the grating a. The maximum length of the signal window can be increased further by reducing a. This effectively brings the addressing beam profile

closer to the center. One can adjust the position of the addressing beam profile as long as the zeroth-order beam at the center is not affecting the experiment. The ratio between the dimension of a single addressing beam and the addressable image plane is ultimately determined by the number of mirrors in the Fourier plane. With a different model of DMD (e.g. DLP9000XUV from Texas Instrument) that contains more micromirrors, it is possible to increase the number of addressable ions to more than a hundred. For example, to achieve more than a hundred addressable ions with similar spacings[62], we can set $a = 8d$, and this gives us an addressable window with width more than twice the width of the window of the addressing profile shown in the Fig. 4.6b-c. Also, for the DLP9000XUV DMD model, it has a similar aperture size but with the micromirror size d about 30% smaller. This effectively gives another 40% increase in the size of the addressable image plane.

4.7.2 Power Efficiency

For simultaneously addressing n ions by n focused Gaussian beams, the beam profile in the FP looks like an interference pattern of n sources (each located at an ion position), modulated by a wide Gaussian envelope. The maximum amplitude of this FP interference pattern is n times the amplitude of the Gaussian envelope from a single source (ion). Hence, for a fixed intensity of the incoming beam at the DMD FP, the intensity at each ion scales by $1/n^2$.

As a result, despite the DMD's numerous benefits, including flexible and accurate addressing capabilities, it may not be the optimal choice for power-intensive applications that require simultaneous addressing of many ions. For instance, engineering spin-spin interactions for all-to-all connectivity using the Mølmer-Sørensen scheme, a task that demands simultaneous multi-ion addressing and high power, might pose challenges when using a DMD. This underscores the importance of considering the specific requirements of an application when selecting the appropriate technology.

4.8 Conclusion

In this chapter, we have presented the key components of the DMD-based holographic addressing system. We discussed the design of the optical system, the generation of the hologram, and the techniques for evaluating performance.

Our system is highly precise and exhibits minimal crosstalk error (10^{-4} level intensity crosstalk). We demonstrated that we can achieve more than 99.9% fidelity for single ion resetting while preserving the quantum state of the neighboring ion. With reasonable assumptions regarding parameters from the current state-of-the-art detector, we can achieve more than 99.6% fidelity for performing single ion detection while preserving the quantum state of the neighboring ion. Such a low level of crosstalk opens up the possibility to experimentally study new types of physics, such as measurement-induced phase transitions[16], or making quantum error correction within reachable range[55, 1].

Note that the results presented in this chapter don't require us to shuffle or loosen the trapping potential to increase the inter-ion spacing for performing the reset or measurement. This offers a significant advantage as the shuffling process can be time-consuming and can lead to the excitation of motional modes.

We also examined the scalability of the DMD-based addressing system. Our scheme is incredibly scalable for large-number ion chains. The current setup enables us to create high-quality addressing beam profiles that is suitable for system with 50+ ions.

Moreover, our addressing system can be readily adapted to other ion species, 2D ion crystals, and other quantum computing platforms that also use optical addressing for quantum controls, such as neutral atom arrays, Rydberg atoms, and nitrogen-vacancy centers in diamond.

The downside of the DMD-based holographic addressing system is its suboptimal power efficiency. The scaling of power efficiency limits the number of simultaneously addressable ions for power-intensive applications. We will delve further into how we design the addressing beam specifically for individual Raman beam addressing, an application that falls into this category, in a later chapter (Chapter 6).

In conclusion, the individual optical addressing technique we presented provides a powerful tool for the quantum control of trapped ions and many other systems. It is especially useful in applications that require non-coherent quantum control, like spin reset or measurement, at an individual level. These applications have stringent requirements on crosstalk error and generally require minimal optical power.

Chapter 5

Temporal Quantum Control and Floquet Hamiltonian Simulation

This chapter delves into the temporal control of quantum systems and the investigation of dynamic freezing in strongly driven Floquet systems using trapped ions. The original theoretical framework for dynamic freezing was laid out by Haldar et al. (2018) [25] and Haldar et al. (2019) [26].

My colleagues - Sainath Motlakunta, Nikhil Kotibhaskar, Anthony Vogliano, Lewis Hahn, Jingwen Zhu, Rajibul Islam - and I have collaborated on adapting the protocol to a trapped ion system and experimentally demonstrating dynamic freezing in a strongly driven Floquet system using trapped ions.

My primary contributions encompass leading the experimental study demonstrating the dynamic freezing behavior in a strongly driven Floquet system using trapped ions. Additionally, I independently developed and performed the numerical simulations presented in this chapter.

The process to realize the requisite quantum controls for this protocol has also led to contributions to the open-source community:

1. **spcm** (as the lead developer): This Python package controls the arbitrary waveform generator from Spectrum Instrumentation GmbH. Compared to the official Python package, spcm offers a more intuitive, high-level, and more pythonic interface.

2. **WaveformConstructor** (as the lead developer): This Python package generates the waveforms necessary for Hamiltonian engineering. It automatically tracks the

phase across multiple waveform segments during evaluation, providing users with a simplified, high-level approach to waveform description.

5.1 Overview

Beyond the precise addressing control over individual ions as discussed in Chapter 4, another vital ingredient for quantum information processing is the temporal control of the quantum system. This control's flexibility and precision allow us to explore more complex quantum algorithms or simulate time-dependent Hamiltonians.

In this chapter, we will discuss engineering various types of Hamiltonians using arbitrary waveform generation, including spin-spin interactions and effective magnetic fields in the spin model. We will also explore a type of time-dependent Hamiltonian that necessitates more sophisticated temporal control, i.e. the Floquet Hamiltonian.

A Floquet system refers to a periodically driven system. Recent studies show that such systems can create novel forms of spatiotemporal orders in closed quantum chaotic systems, such as the so-called time crystals [73, 11]. The research on Floquet quantum system bridges quantum many-body physics and thermodynamics, heralding a new direction to investigate unique phases of matter that emerge under inherently non-equilibrium conditions.

Apart from the implementation of different types of Hamiltonians, we will also discuss our study on researching the emergent conservation laws in a strongly driven Floquet system. We will show both numerically and experimentally that the total magnetization of a transverse field Ising Hamiltonian implemented with trapped ions is conserved under a strong Floquet drive. This conservation occurs even though the system would otherwise be "thermalized" and become featureless due to the ergodicity of the Hamiltonian.

5.1.1 Outline

1. Section 5.2: We will discuss the Hamiltonian of interest and the drive protocol used to achieve dynamic freezing.
2. Section 5.3: We will describe the experimental setup and how we engineer the necessary Hamiltonian.
3. Section 5.3.2: We will present our experimental results demonstrating total magnetization freezing and examine the dynamics of individual spins.

4. Section 5.4: We will discuss future experiments exploring the freezing behavior in open quantum systems. Additionally, we will provide numerical simulations supporting the existence of this freezing behavior.

5.2 Description of the Protocol

Here, we will discuss the Hamiltonian we are interested and the drive protocol. The Hamiltonian $H(t)$ we are interested in is the transverse field Ising model H_0 with a Floquet Hamiltonian $H_D(t)$. The Hamiltonian is given by

$$H(t) = H_0 + H_D(t) \tag{5.1}$$

$$H_0 = \sum_{i,j} \frac{J_{ij}}{2} \sigma_x^i \sigma_x^j + B_y \sum_i \sigma_y^i \tag{5.2}$$

$$H_D(t) = B_x^{\text{Floquet}} \sum_i \text{sign}(\sin(\omega t)) \sigma_x^i \tag{5.3}$$

The static part of the Hamiltonian, H_0, consists of the Ising interaction of strength J_{ij} and a transverse field. This transverse field has a strength of B_y and is oriented along the y direction. It doesn't commute with the Ising interaction. The Floquet drive, H_D, is a periodic driven transverse field along the x direction. This drive field periodically flips its direction between the $+x$ and $-x$ directions with a period of $2\pi/\omega$.

Comparing to the Hamiltonian in the original protocol [26, 25], the difference lies in the Ising interaction. In the original protocol, the Ising interaction is limited to nearest and next-nearest neighbor interactions. However, in our case, we approximate the interaction strength J_{ij} to follow a power law decay of $J/|i-j|^\alpha$ [7]. Implementing our spin-spin interaction is relatively straightforward in the trapped ion system using a global Raman beam. By tuning the detuning from the center of mass mode (COM) frequency (radial mode) of the Mølmer-Sørensen interaction, we can control the decay constant α of the Ising interaction, which can range between 0 and 3 [7]. In essence, we can adjust the interaction range of the Ising interaction by manipulating the laser frequency.

The presence of the non-commuting transverse field ($B_y \sum_i \sigma_y^i$ in Eq. 5.2) renders the Hamiltonian H_0 ergodic. The verification of ergodicity can be found in the Supplementary section of Haldar et al. (2018) [25]. The ergodic nature of the Hamiltonian H_0 implies that the system will ultimately "thermalize" and lose its distinct features. Consequently, the magnetization of the spin will depolarize and tend towards zero.

However, both the original theoretical study[26, 25] and our numerical simulations with the modified Hamiltonian have shown that under strong Floquet driving, with certain ω values, the total magnetization of the system, as an emergent conserved quantity, freezes. Notably, the threshold for freezing B_x^{Floquet} lies roughly between $10J$ and $20J$, and the frequency of the sign flipping needs to satisfy the following condition:

$$\omega = \frac{B_x^{\text{Floquet}}}{N^{\text{Floquet}}} \tag{5.4}$$

where N^{Floquet} is a positive integer. We refer to the sign-flipping frequency ω that satisfies this relation as scar points.

As for the magnetization, we define the magnetization as the expectation value of the spins. For the ith ion, its magnetization along the x direction is defined as

$$m_x^i = \langle \sigma_x^i \rangle \tag{5.5}$$

The total magnetization of the system along the x direction is defined as the sum of the magnetization of all the spins:

$$m_x = \sum_i m_x^i \tag{5.6}$$

5.3 Setup

As outlined in Eq. (2.7) and Eq. (2.5.3), the transverse field Ising model can be realized using Raman beams. The experimental setup is depicted in Fig. (5.1). We utilize two Raman beams, R1 and R2, which illuminate the ions from two different angles. The detailed experiment setup can be found in Sec. 3.5.

The transverse field of the Hamiltonian can be engineered by R1 with a frequency driving the carrier flipping, as shown in Eq. (2.7). The direction of the field can be controlled by the phase difference between R1 and R2. Since R2 is driven by a fixed frequency and phase beam, the phase difference is effectively controlled by the phase of R1, which is controlled by the RF driving the AOM. The Floquet field can also be implemented similarly, but periodically changes the phase to flip the direction of the field.

For the spin-spin interaction, we can apply the Mølmer-Sørensen scheme as described in section 2.5.3. Specifically, we use the phase-sensitive configuration, where both beat notes co-propagate in the same direction.

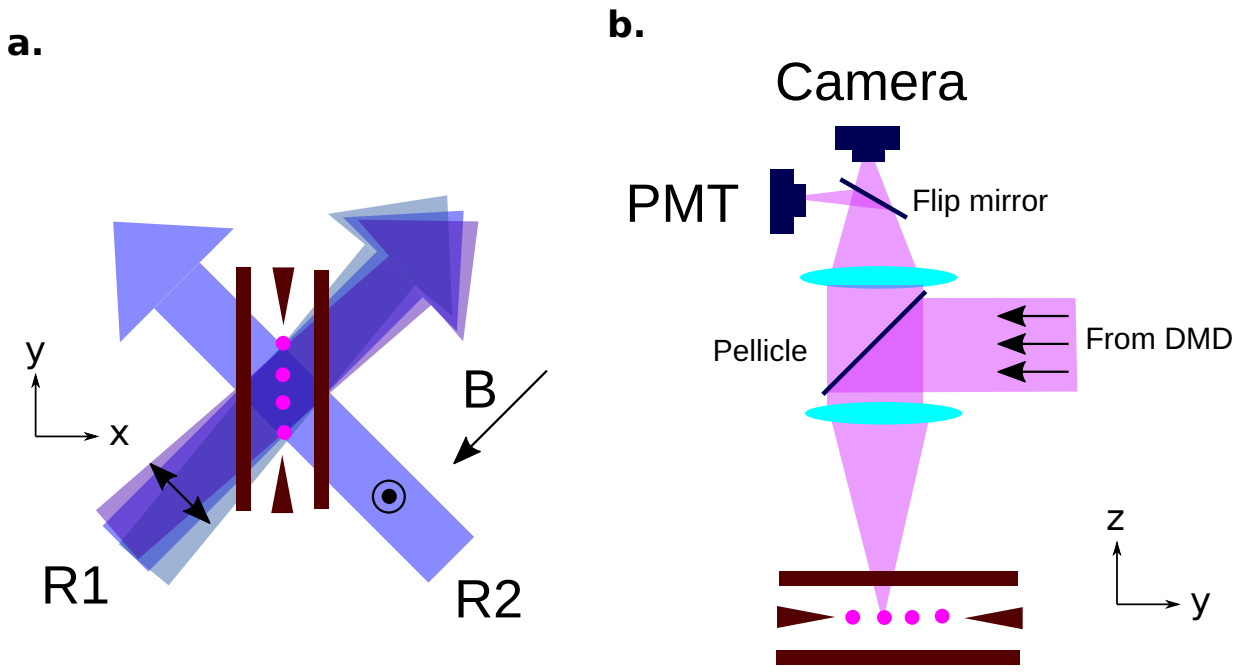

Figure 5.1: **Setup of the experiment. a.** The linear polarized Raman beams are on the x-y plane. The polarization of the two Raman beam is orthogonal to each other, and the resulting beat note is propagating along the x-axis, which is in the radial direction of the trap. **b.** The individual spin reset beam is coming along the z-axis (perpendicular to the x-y plane).

Interaction	Detuning (from carrier)	Phase
σ_x^i	0	0
σ_y^i	0	$\pi/2$
$\sigma_x^i\sigma_x^j$	$-\mu$, μ	0, $-\pi$
$\sigma_y^i\sigma_y^j$	$-\mu$, μ	$\pi/2$, $-\pi/2$

Table 5.1: Waveform generation for realizing the Hamiltonian. If there are multiple tones in the waveform, we separate them by commas.

In addition to the Raman beams, an imaging system collects the fluorescence from the ions and projects it onto either a photomultiplier tube (PMT) or a camera. The same microscope also delivers individual optical pumping beams created by the digital micromirror device (DMD), enabling us to individually reset the spin to the $|0\rangle$ state. Further details on the individual addressing system are discussed in Sec. (4.3) and illustrated in Fig. (4.2).

5.3.1 Waveform Generation for Realizing the Hamiltonian

We use a phase-sensitive configuration to realize the spin-spin interaction. In this configuration, both the phase of the spin operator in the transverse field (Eq. 2.9) and the phase of the spin-spin interaction (Eq. 2.18) contain a $\delta k\bar{X}$ term. This term can be disregarded as a global phase. In our setup, since R2 is driven by a beam with fixed frequency and phase, the phase and interaction strength are implemented by generating different phase-referenced waveforms from the AWG.

Table 5.1 specifies the frequency and phase of the waveform for realizing different terms of the Hamiltonian. We select a phase angle of 0 as the direction of the X axis. This is also the convention we used in the pre-defined waveform function in the WaveformConstructor Python package we developed.

This table illustrates the waveforms required to generate the various terms in the Hamiltonian. For example, to realize the σ_x^i interaction, the carrier is not detuned (i.e., 0 detuning), and the phase is set to 0. To realize the $\sigma_x^i\sigma_x^j$ interaction, two tones are required with a detuning of $-\mu$ and μ, and phases of 0 and $-\pi$, respectively. The detuning relative the Spectrum determines the interaction profiles. A few examples is shown in Fig. 2.10.

5.3.2 Results

5.3.3 Results: Characterization of the system

Characterization of the coherence time

To ensure the validity of the experiment, we first need to make sure the oscillator of the RF and the ions' internal states remain coherent. As mentioned previously in Table 5.1, the axis of the spin operators are defined by the phase of the Raman beams. If the two don't remain coherent, the engineered spin operators will no longer have a well-defined axis, and the Hamiltonian we engineered will no longer be valid.

To assess the coherence, we can employ the Ramsey spectroscopy technique referenced in Sec. 4.5. In the Ramsey spectroscopy, the state of the ion are first brought to the equator of the block sphere from the $|0\rangle$ through a $\pi/2$-pulse. After a certain period of the time, we apply another an opposite $\pi/2$-pulse to the state and measure the state of the ion. The pulse sequence is shown in Fig. 5.2a.

If we detune the frequency of the oscillator, the state will precess around the equator of the Bloch sphere. Consequently, we can observe state oscillation by varying the waiting time between the two $\pi/2$-pulses.

If the oscillator starts to lose coherence, the phase, a.k.a., the rotation axis of the second $\pi/2$-pulse will not be well-defined relative to the state. As a result, the contrast of the oscillation will decrease. By measuring the decay's characteristic time, we can deduce the system's coherence time. From the measurement presented in 5.2b, it shows that the characteristic time is 177 ms. Ideally, we aim to ensure our experiment's duration stays within this timescale.

5.3.4 Results: Calibrations of the Hamiltonian

We experimentally measure the individual terms of the Hamiltonian of the protocol described in Sec. 5.2 to verify that the Hamiltonian is implemented correctly. We first started with the measurement with two ions in the trap. With only two ions in the trap, there is only a pair of spin-spin interaction term. If we initialize the system to $|00\rangle$ (in the z basis), the system will evolve to $|11\rangle$ under the spin-spin interaction (along x direction).

The measurement result is shown in the Fig. 5.3a. We can observe the contrast of the flopping doesn't decrease significantly, which indicates that the evolution remains coherent withing the experimental time (10 ms here).

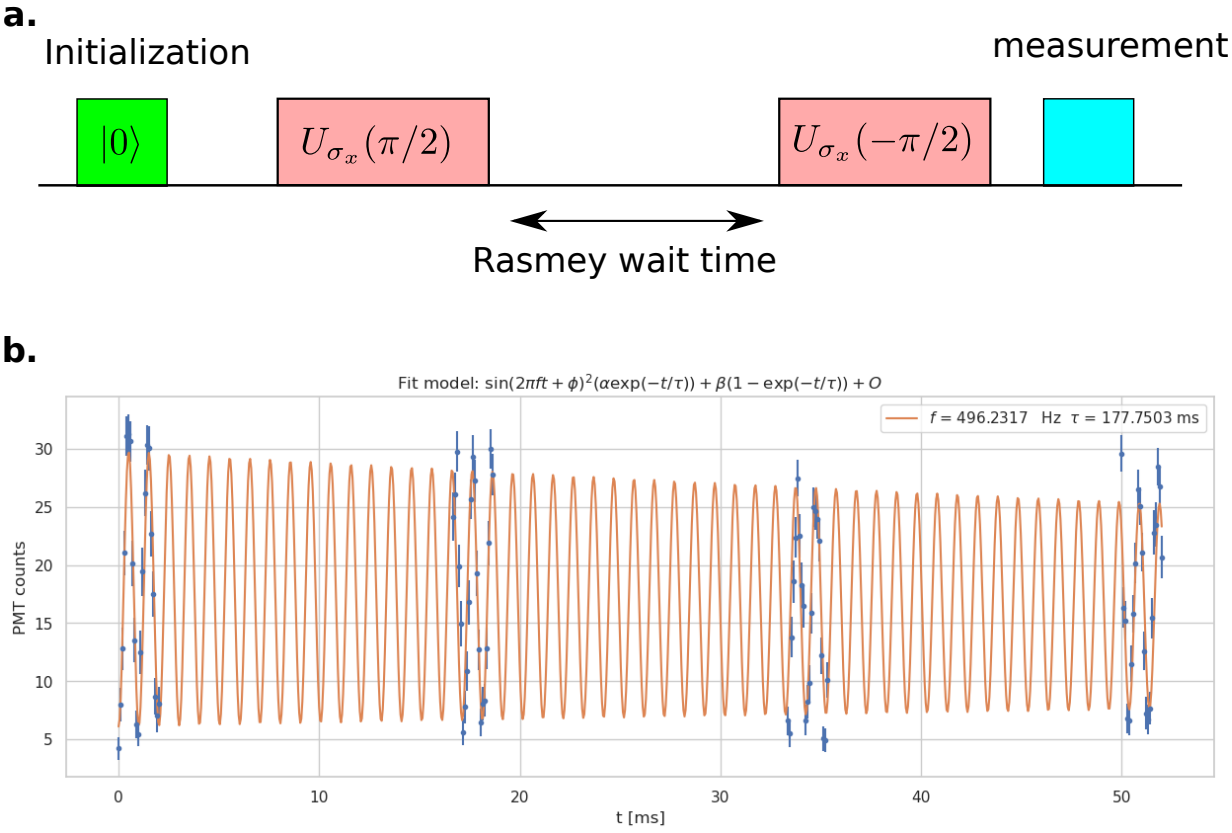

Figure 5.2: **Ramsey spectroscopy for coherence characterization. a.** The pulse sequences. **b.** Experimental measurement of the Ramsey spectroscopy. The error bars represent the standard error of the measurement. The data is fitted to a sinusoidal function with lopsided exponential decay envelope. The characteristic time of the decay is 177 ms. In this experiment, the oscillator is set to be detuned by 1 kHz.

In the protocol, the transverse field ($\sum_i B_y \sigma_y^i$) has its strength at the same order of magnitude of the spin-spin interaction. In Fig. 5.3b, we show the state evolution under the transverse filed Hamiltonian we engineered. The state is also initialized to $|00\rangle$, and the system evolves to $|11\rangle$ under the transverse field. We can see the contrast of the flopping also remains high and the evolution speed which indicates the strength of the field is close to the one of the spin-spin interaction. Both of them are around 0.35 kHz.

As for the Floquet drive, we can also calibrate the strength of the field similarly. Fig 5.3c shows the state evolution under a drive field that has the same amplitude of the Floquet drive we planned to engineer but without the sign flipping ($\omega = 0$). The frequency of the evolution is around 8.3 kHz which is about 23 times faster than the spin-spin interaction and the transverse field.

With the calibrated individual Hamiltonian terms, we applied them to the two ions and measure the fluorescence counts after a certain period of time. The fluorescence counts indicate the total magnetization of the spin state. We vary the time the Hamiltonian is applied and observe the dynamics and observe the difference with and without the presence of the Floquet drive.

The result is shown in Fig. 5.4, the fluorescence count remains the same if the Floquet drive described in Fig. 5.4c exists in the Hamiltonian. On the other hand, if the Hamiltonian is consists of only the spin-spin interaction (5.4a) and the transverse field (5.4b), the fluorescence count will not stay locked.

Characterization of the mode spectrum

With two ions with harmonic trapping potential confinement, the axial trapped frequency ω_a is related to the trapped frequencies of center-of-mass mode ω_{COM} and the tilt mode ω_{Tilt} of the radial modes by the following equation[30]:

$$\omega_a = \sqrt{\omega_{\text{COM}}^2 - \omega_{\text{Tilt}}^2} \tag{5.7}$$

Shown in the Fig. 5.5 is the radial mode spectrum of the two ions. The scan is performed with a blue sideband Raman pulse with duration close to its π-pulse time. The frequency of the Raman pulse is scanned by modulating the AOM driving the R2 beam. The center-of-mass mode (COM) of the radial mode which is also the radial trapped frequency is about 1.135 MHz, and the COM-Tilt mode splitting is about 17 kHz. With equation 5.7, we can estimate the axial trap frequency to be about 195.7 kHz.

a. spin-spin interaction

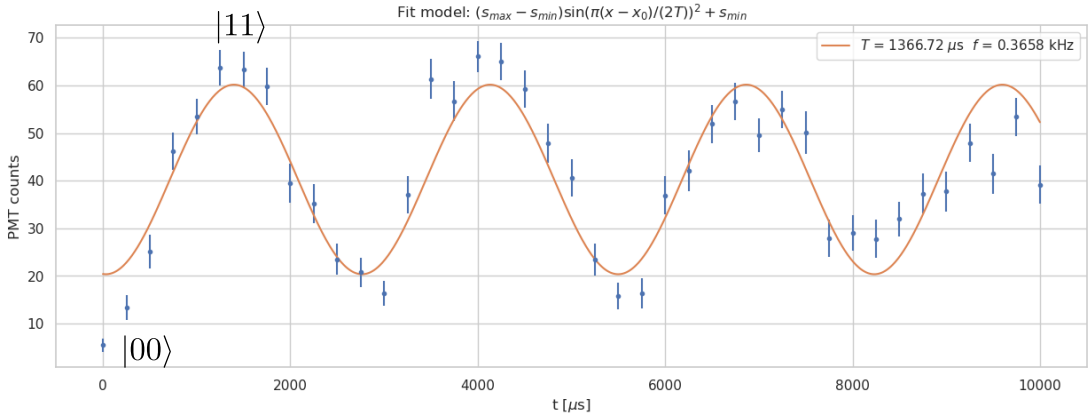

b. transverse field

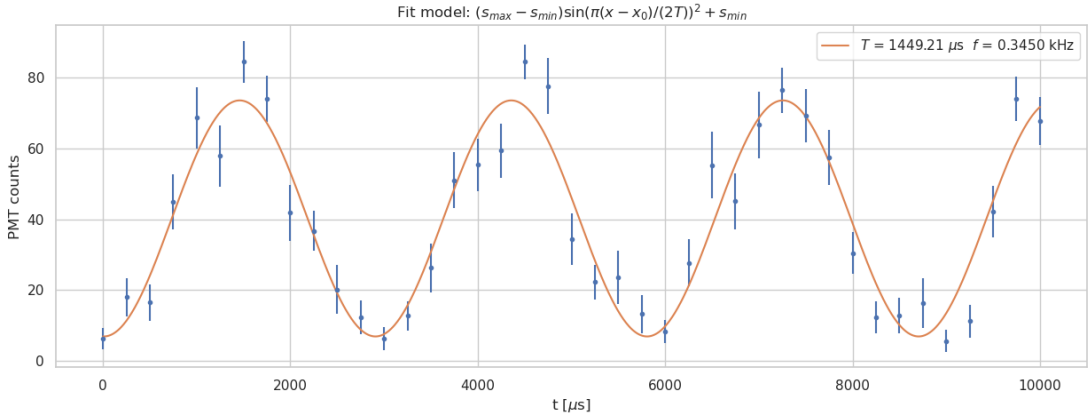

c. Floquet drive field

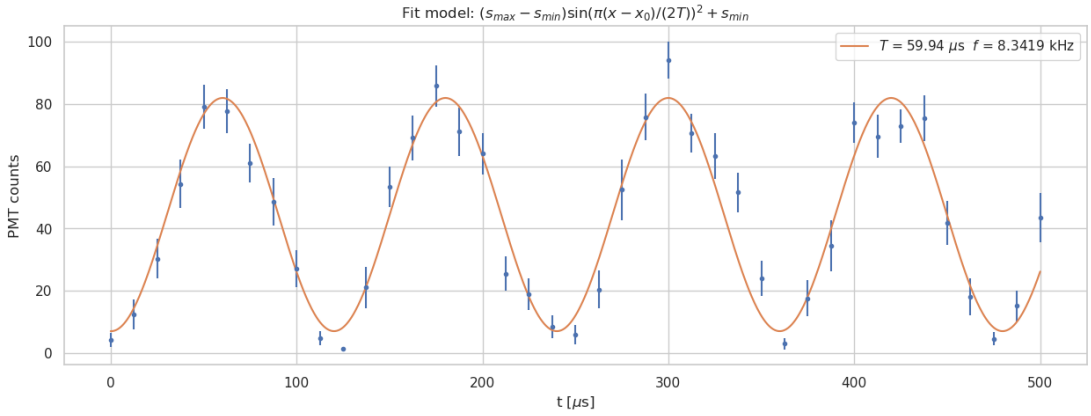

With this information, we are able to solve the equilibrium positions of the ions and all the mode frequencies ω_ms[31]. Using Eq. 2.24, we are then able to estimate the strength of the spin-spin interactions J_{ij} of pairs of ions while working with multiple ions.

5.3.5 Results: Dynamics within sectors of the Hilbert space

As discussed in Section 5.2, the total magnetization is an emergent conserved quantity. However, in order to provide further evidence that the freezing dynamics exhibit many-body physics properties, we examine the eigenstates of σ_x^i instead of considering the fully polarized state. These eigenstates have multiple instances with the same non-zero total magnetization.

The theoretical prediction suggests that the total magnetization is conserved, but not at the individual state level. The Hilbert space is fragmented into sectors, and within each sector, the total magnetization remains conserved. However, dynamics can occur within individual sectors. In other words, while the individual spin magnetizations are not conserved, the total magnetization of the system is conserved.

To create a non-fully polarized eigenstates, individual addressing capability is required. As depicted in Figure 5.6a, we initialize the state to $|000...0\rangle$ using global optical pumping. We then use a microwave π pulse to transform the state into $|111...1\rangle$. Next, utilizing the individual addressing system described in Chapter 4 and Section 5.3, we individually pump selected ions to the $|0\rangle$ state. Once the non-trivial state is prepared, we rotate it into the x basis using a Raman $\pi/2$ pulse and apply the Hamiltonian. Finally, we measure the system again in the x basis using another Raman $\pi/2$ pulse.

In Figures 5.6b-c, we present the experimental results. In this experiment, we have four ions in the trap, initialized in the $|1101\rangle_x$ state before applying the Hamiltonian. The Mølmer-Sørensen detuning μ is set to +5 kHz from the COM mode. The normalized interaction matrix is shown in Figure 5.6d.

Figure 5.3 *(preceding page)*: **Measurement of Individual Terms of the Hamiltonian of the Protocol** The error bars in all the figures indicate the standard error. **a. Spin-spin interaction.** The Mølmer-Sørensen detuning is set to be +5 MHz detuned from the center-of-mass mode. **b. Transverse field.** The transverse field is implemented with the carrier transition. **c. Floquet drive.** The Floquet drive is implemented with the carrier transition. The frequency of the sign flipping is set to be 0.

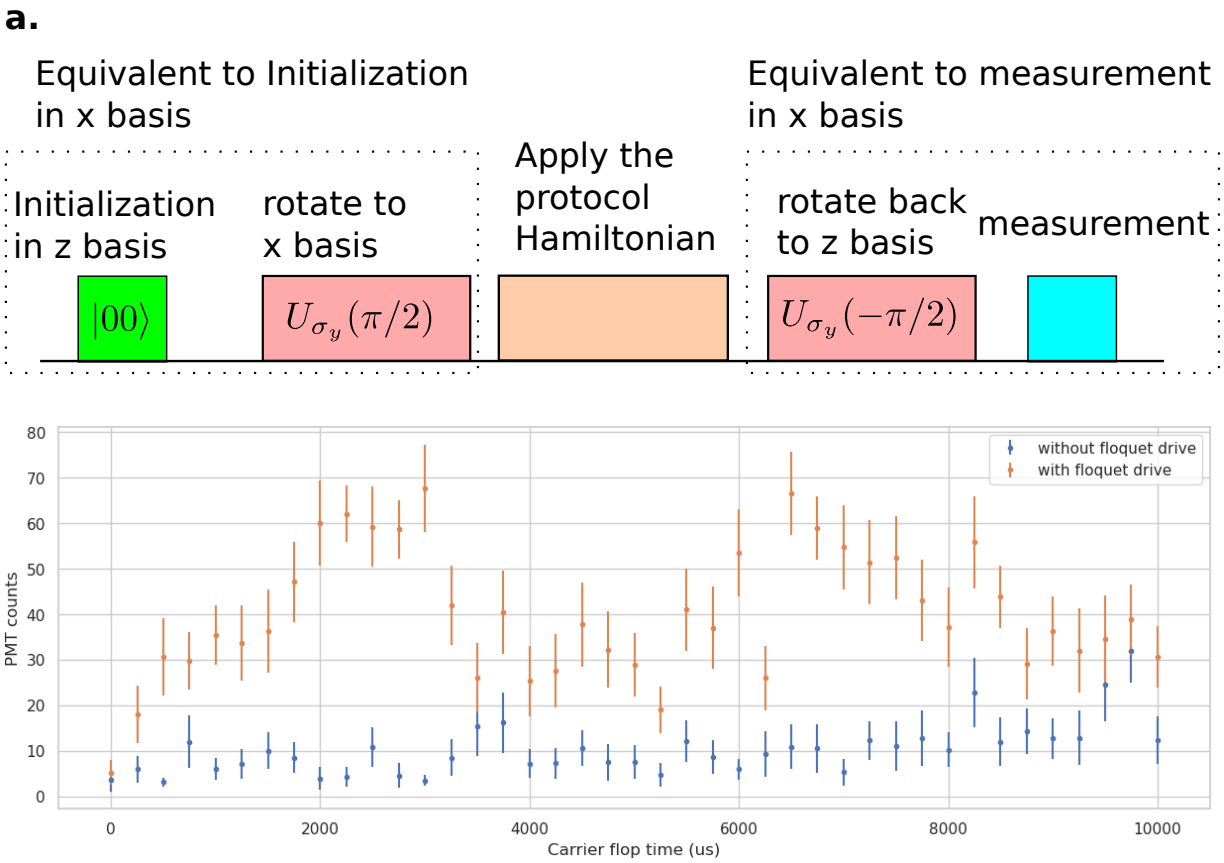

Figure 5.4: **Dynamics freezing with two ions. a.** Illustration of the timing sequence of the experiment. The ions are first initialized in the $|00\rangle$ state through optical pumping and rotate to the x basis ($|00\rangle_x$). The protocol Hamiltonian is applied for a certain period of time. Finally, the state is rotated back to the z basis and measured, which effectively measures the ions in the x basis. **b.** The fluorescence count of ions with and without the Floquet drive. The y-axis in the plots is the averaged fluorescence count of the ions. It indicates the total magnetization. In this experiment, two ions are initialized in the $|00\rangle_x$ states. With two ions The individual terms of the interaction are characterized in Fig. 5.3. The two-ion bright state $|11\rangle_x$ has an averaged fluorescence count of about 80 (40 each). The error bars in this plot indicates the standard error.

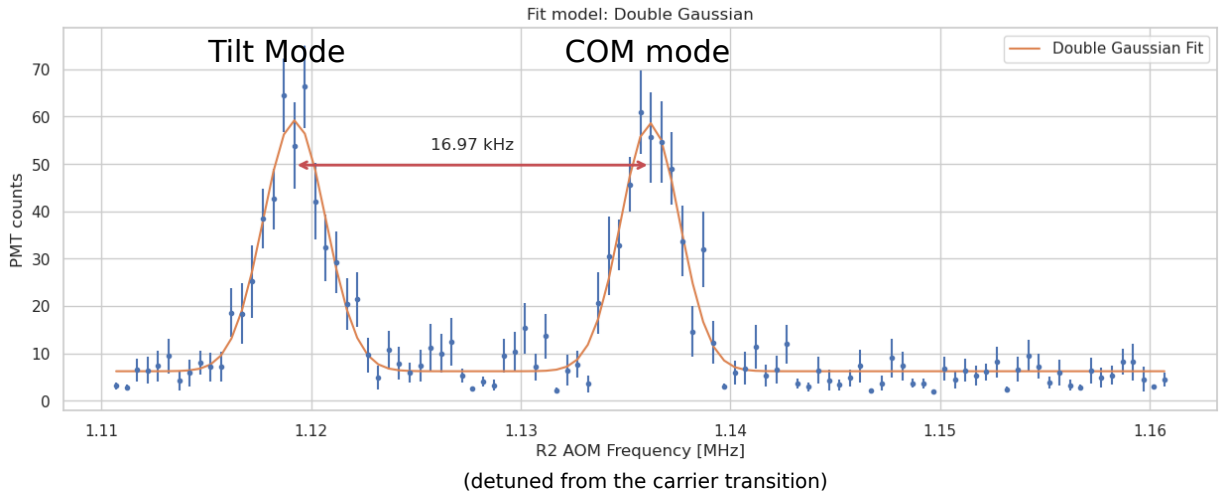

Figure 5.5: **Radial mode spectrum of the two ions.** The x-axis is the RF frequency modulating the R2 beam through the AOM. The frequency corresponding the carrier Raman transition is 211.088 MHz. The COM-Tilt mode splitting is about 17 kHz.

We compare two cases: with and without the Floquet drive field. Within the timescale of the spin-spin interaction $2\pi/J_0 \sim 2.6$ms, the total magnetization of the system without the Floquet drive is statistically significant deviated from the initial value. On the other hand, the change of the total magnetization of the system with the Floquet drive is strongly suppressed at system's interaction timescale. This supports the theory that total magnetization as an emergent conserved quantity under the Floquet drive.

Additionally, when examining the individual spin magnetizations in Figure 5.6c, it can be observed that they are not conserved within the interaction timescale. The spins do not evolve at the same rate, with the third spin, initialized in the opposite direction, evolving roughly three times faster than the other spins. Therefore, even though individual spin magnetizations are not conserved, the total magnetization remains conserved.

The disparity in the evolution rates of individual spin magnetizations suggests that the interactions play a role in the system's dynamics and the manifestation of many-body physics properties.

To accelerate the evolution of individual spin magnetizations, we introduce approximately 6% $\sigma_i^y\sigma_j^y$ interactions to the Hamiltonian. Numerical simulations have shown that the addition of $\sigma_i^y\sigma_j^y$ interactions does not alter the freezing behavior of total magnetization but accelerates the dynamics within the sector.

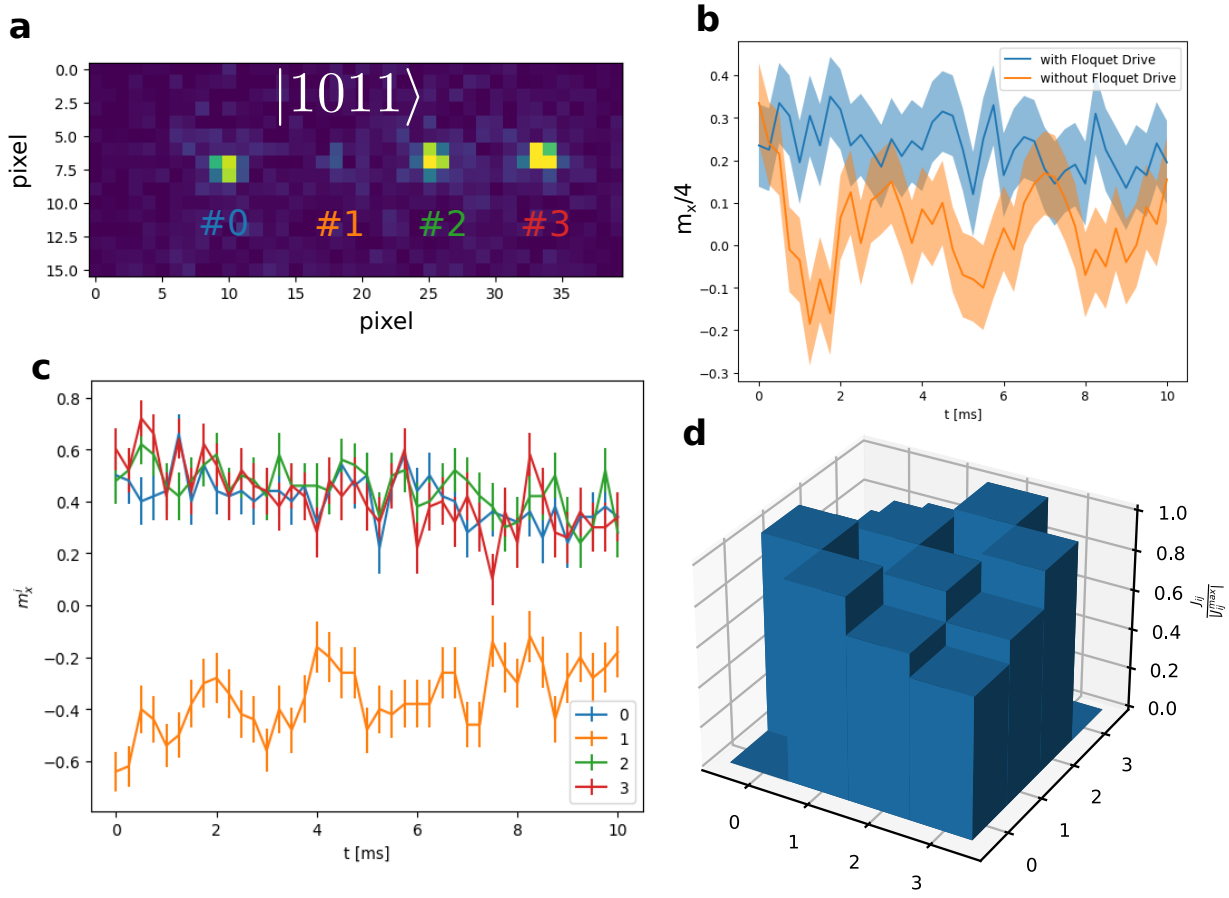

Figure 5.6: **Dynamics within sectors of the Hilbert space. a.** Ion image of the initial state. The initial state is initialized to $|1101\rangle$. Ion #1 is reset to $|0\rangle$ state by the individual reset beam. **b.** Total magnetization m_x of the system with and without the Floquet drive. The shaded area is the standard error of the measurement. The total magnetization in y-axis is divided by the number of ions in the trap (4 in this figure) for normalization. **c.** Individual magnetization m_x^i of each spin with the Floquet drive. The error bar represents the standard error of the measurement. **d.** Normalized interaction strength calculated by the experiment parameters. The experiment uses the following parameters $B_x^{\text{Floquet}} = \omega = 22.98J_0$, $B_y = 0.94J_0$, $J_0 = 2\pi \times 0.366$ kHz. Each points in **b** and **c** are averaged over 100 shots. To accelerate the evolution of individual magnetization, we add about 6% (relative to the $\sigma_i^x\sigma_j^x$ interactions) $\sigma_i^y\sigma_j^y$ interactions to the Hamiltonian.

We compare the experimental results with simulation results (Fig. 5.7). The simulation results also demonstrate that individual spin magnetizations evolve at different rates while the total magnetization remains conserved. Spin 3 evolves faster than the other spins.

It should be noted that the experimental results do not perfectly match the simulations, as the individual magnetizations m_x^i of spins 0 and 3 return to 1 (fully aligned along the $+x$ direction). This discrepancy may be attributed to two potential reasons: non-uniform Rabi frequency and decoherence.

The non-uniformity in Rabi frequency can arise from the finite beam width of the Raman beams and imperfect alignment of their optics. Shown in Figure 5.7, simulations with non-uniform Rabi frequencies across the ion chain demonstrate that the individual magnetizations of spins 0 and 3 do not return to 1. These simulation results align better with the experimental findings.

Regarding the potential impact of decoherence, we simulate the dynamics with decoherence. We model decoherence using the following collapse operator in the Lindblad master equation:

$$\sqrt{\gamma_{\text{de}}} \sum_i \sigma_x^i, \tag{5.8}$$

where γ_{de} corresponds to the decoherence rate. This choice of collapse operator represents the decoherence resulting from the heating of modes coupled to the spin states via the Mølmer-Sørensen interactions, as the heating relies on spin-dependent forces. Since the Mølmer-Sørensen interaction operates along the x-direction, we utilize σ_x^i as the collapse operator.

Figure 5.7 demonstrates the simulation results with decoherence. The simulations are performed by solving the Linbalad master equation using a Monte Carlo solver. It can be observed that the simulations better match the experimental results.

5.4 Outlook: Dynamics Freezing in Open Quantum System

One interesting direction for future study is to connect dynamic freezing to open quantum systems. The idea is to selectively decohere some of the spins in the system and observe the dynamics of the rest of the system.

To describe the engineered non-coherent process, we use the collapse operator C_n and simulate the dynamics of the quantum system. The evolution of the density matrix can be calculated by solving the Lindblad master equation.

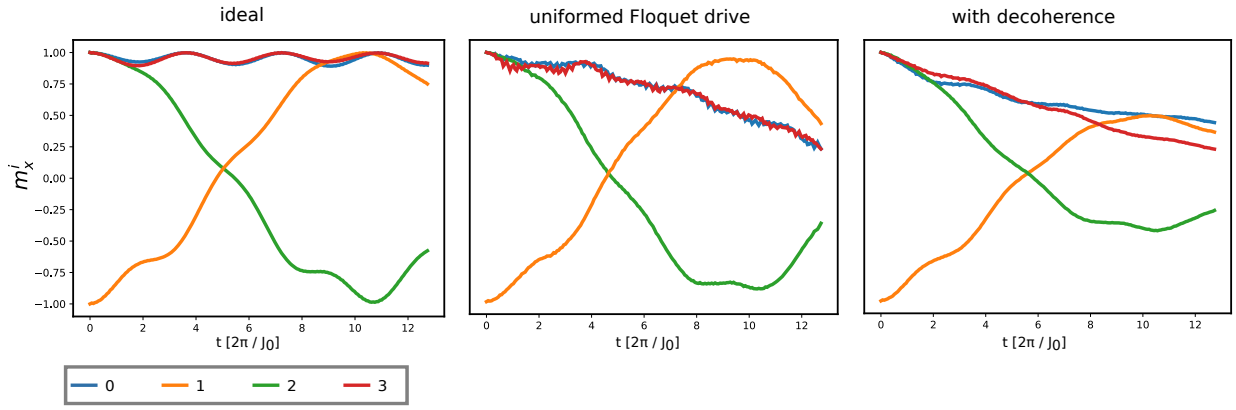

Figure 5.7: Evolution of magnetization of individual spins. The simulation of ideal scenario is performed with the parameters specified in Fig. 5.6. The simulation with non-uniformed Floquet drive, the strength of the Floquet fields for ion 0 and 3 are 10% lower. The simulation with $\sum_i \sigma_x^i$ decoherence has its rate $\gamma_{\text{de}} = 4J_0$.

$$\dot{\rho}(t) = -\frac{i}{\hbar}[H(t), \rho(t)] + \sum_n \frac{1}{2}\left[2C_n\rho(t)C_n^\dagger - \rho(t)C_n^\dagger C_n - C_n^\dagger C_n\rho(t)\right] \tag{5.9}$$

With the high-quality individual addressing we developed in chapter 4, we are able to selectively decohere the specific ions in the chain without affecting the rest of the system. Here we consider two processes, optical pumping and spin measurement.

The first process, optical pumping, resets the spin to the $|0\rangle$ state (along the Z direction). We model this process with projection operators. Below, we show the collapse operator modeling optical pumping of the spin of an ion in the chain, and the rest of the spins in the system are left intact. The γ_{opt} corresponds to the rate of the spin reset process.

$$C_{opt} = \sqrt{\gamma_{\text{opt}}} I \otimes ... I \otimes (|0\rangle\langle 1|) \otimes I ... \otimes I \tag{5.10}$$

Apart from optical pumping, the other non-coherent process we are able to engineer is spin measurement (along the Z direction). This can be modeled by applying the Pauli Z-gate to a particular spin σ_z. Similarly, the γ_{prob} corresponds to the rate of this process.

$$C_{prob} = \sqrt{\gamma_{\text{prob}}} I \otimes ... I \otimes \sigma_z \otimes I ... \otimes I \tag{5.11}$$

Shown in Fig. 5.8 is the simulation with optical pumping and spin measurement applied to the first spin of the chain. Note that we set the rate of the decoherence process to be

on the same order of magnitude as the spin-spin interaction strength J_{ij}. If the rate of the decoherence process is much faster than the spin-spin interaction strength, the spin of the addressed ion will be "pinned" and will not interact with the rest of the system due to the quantum Zeno effect.

From the numerical simulation, we can see that the total magnetization quickly drops by one but remains locked in the presence of the Floquet drive field. The rapid decay is because the first ion quickly depolarizes due to the probe beam. However, the total magnetization of the rest of the system is still locked by the Floquet drive field. It shows that dynamic freezing can still occur in a subsystem that is connected to the environment, and the physics behind it is yet to be explored.

The experiment described here is feasible with the current setup. The high-quality beam addressing we developed in chapter 4 allows us to selectively address the ions in the chain without affecting the others. Since the decoherence rates γ_{prob} and γ_{opt} are of the same order as the dynamics of the system, the 10^{-4} crosstalk shown in section 4.5 should have little effect on the rest of the system during the experiment time.

5.5 Conclusion

In this work, we have experimentally demonstrated the phenomenon of dynamical freezing in a system of trapped ions. Our results show that the total magnetization of the system can be locked by a Floquet drive field. Interestingly, we have also observed that individual magnetizations of the spins evolve at different rates, revealing a rich dynamic behavior within the sector of the Hilbert space.

Looking forward, there is considerable potential for further study of dynamical freezing in open quantum systems. It will be intriguing to observe how the presence of connections to environment, and the consequent decoherence mechanisms, affect this phenomenon. This proposal is within reach with our current experimental setup, especially given the high-quality individual addressing system we developed as discussed in Chapter 4. Thanks to the ultralow crosstalk error we have achieved, we anticipate that any introduced error will have negligible impact on the rest of the system within the timescale of the dynamics. To support this future work, we present numerical simulations that suggest dynamical freezing can still occur in a subsystem that is connected to an environment.

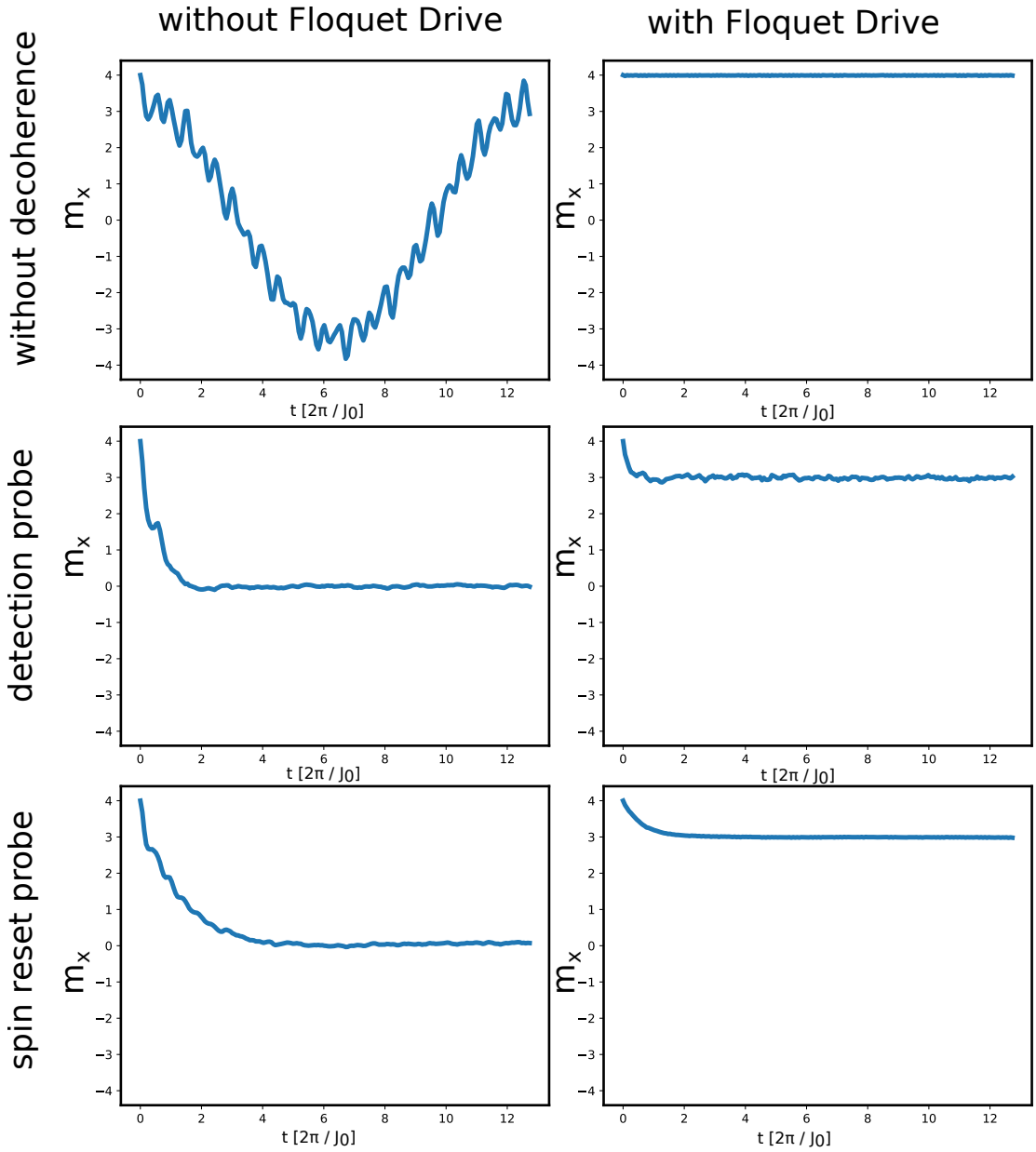

Figure 5.8: Total magnetization m_x comparison with and without the Floquet drive field in the presence of the decoherence process probing a selected ion. The simulation is performed with the following parameters: $B_x^{\text{Floquet}} = \omega = 22.98J_0$, $B_y = 0.94J_0$, $J_0 = 2\pi \times 0.366kHz$, $\gamma_{\text{prob}} = J_0$, $\gamma_{\text{opt}} = J_0$. The J_{ij} matrix follows the same interactions as described in Fig. 5.6. The ions are initialized to $|1111\rangle$.

Chapter 6

Design of Individual Addressing System for Coherent Quantum Operations and Optics for the Next-Generation Ion Trap

In this chapter, we will discuss the development of an optical individual addressing system for coherent quantum operations in our next-generation trapped ion quantum information processing platform. The primary focus of our next-generation ion trap is to operated with a large number of ions (50+) with high optical accessibility and increased trapping frequency.

My main contributions for our next-generation ion trap design are on laying out the optical requirements to ensure it has sufficiently high optical access. For the Raman addressing system presented in the chapter, I designed the optical design of the Raman individual addressing system and simulate the performance. The design presented in the chapter has inputs from my colleagues: Sakshee Samir Patil, Sainath Motlakunta, Nikhil Kotibhaskar, and Rajibul Islam.

6.1 Overview

The existing Raman beam apparatus mentioned in chapter 3 is not able to individually address ions in the ion chain. Though the holographic beam shaping system discussed in

chapter 4 has superior performance in terms of precision and crosstalk error, the power scaling of the system is suboptimal limiting its application in power demanding applications such Raman beam.

In addition, the limited optical access of the current apparatus (up to 0.1NA for the side view port) discussed in chapter 3 fundamentally limits resolution of the optical system. Therefore, the ion trap along with vacuum system also need to be upgraded in order to provide more optical access.

In this chapter, we will discuss the design of the individual addressing system for Raman beams. The addressing system is designed to work with our next-generation ion trap with high optical access.

6.1.1 Outline

1. Section 6.2: We will discuss the criteria for the individual Raman addressing system.
2. Section 6.3: We will provide a concise overview of the next-generation ion trap and discuss how we achieve high optical access in the trap and vacuum chamber design.
3. Section 6.4: We will discuss the optical design of the Raman beam addressing system, including the beam preparation module and the individual addressing module.

6.2 Criteria

We will start with the criteria for designing an optical individual addressing system for coherent quantum operations. These criteria are derived from the requirements of the quantum operations and the limitations of the current apparatus.

- Telecentricity: Unlike conventional imaging systems, the individual addressing system necessitates that the beam be telecentric at the image plane. This requirement arises from the fact that beam pointing affects the coupling to the motional mode in the Mølmer-Sølrensen process or other quantum gates utilizing spin-phonon entanglement. Non-telecentric addressing beams may result in non-uniform coupling and introduce coupling to undesired motional modes (e.g., axial modes). This can be problematic in high NA system as the divergence of the NA can be significant (e.g. 0.45 NA corresponding to about 26 degrees). This allows the beam to hit the

ion at a steeper angle, resulting a non-negligible portion of the wave-vector projection along the axial direction and mismatch in the radial direction. For example, a 0.5 degree incident angle at the intermediate image plane later described in 6.6 can translate into a few degrees of incident angles at the ion image plane without proper compensation.

- Beam Path Matching: The Raman beams employ pulsed lasers, and the pulses of the two Raman beams must temporally overlap at the ion position. From an optical standpoint, this requires that the beam paths of the two Raman beams be matched, ensuring that the pulses of the two beams can reach the ions simultaneously.

- Power Scaling: As Raman process typically require much more power as it is a two-photon process. Ideally, we'd like to have a linear scaling as we increase the number of addressed ion.

- Frequency Modulation: We'd like to have the ability to apply multiple tones of RF frequencies to modulate simultaneously. This is requirement for implementing Mølmer-Sølrensen. Ideally, we'd like to have the spatial profile of the beam to remain the same as we modulate the frequency.

Regarding the choice of laser, the requirements are essentially the same as those for the global Raman beam that we use for the four-rod trap. One can refer to Sec. 3.5 for more details.

6.3 Overview of the Next-Generation Ion Trap

Shown in Fig. 6.3 is the 3D design of our next-generation ion trap. The vacuum chamber is equipped with four reentrant windows in both vertical and horizontal directions, perpendicular to the ion chain direction. The ions are trapped by segmented blade electrodes at the center of the trap. The use of blade electrodes allows us to be closer to the ions, achieving a higher trapped frequency while maintaining good optical access. Along with the reentrant windows, we are able to achieve optical access of 0.5 in the horizontal direction and 0.3 in the vertical direction.

Among the four reentrant windows, the two horizontal entrant windows with larger optical access are used for the individual addressing system described in this section and the imaging system for state detection. The two vertical reentrant windows are used for the auxiliary imaging system and will be integrated with the individual addressing system

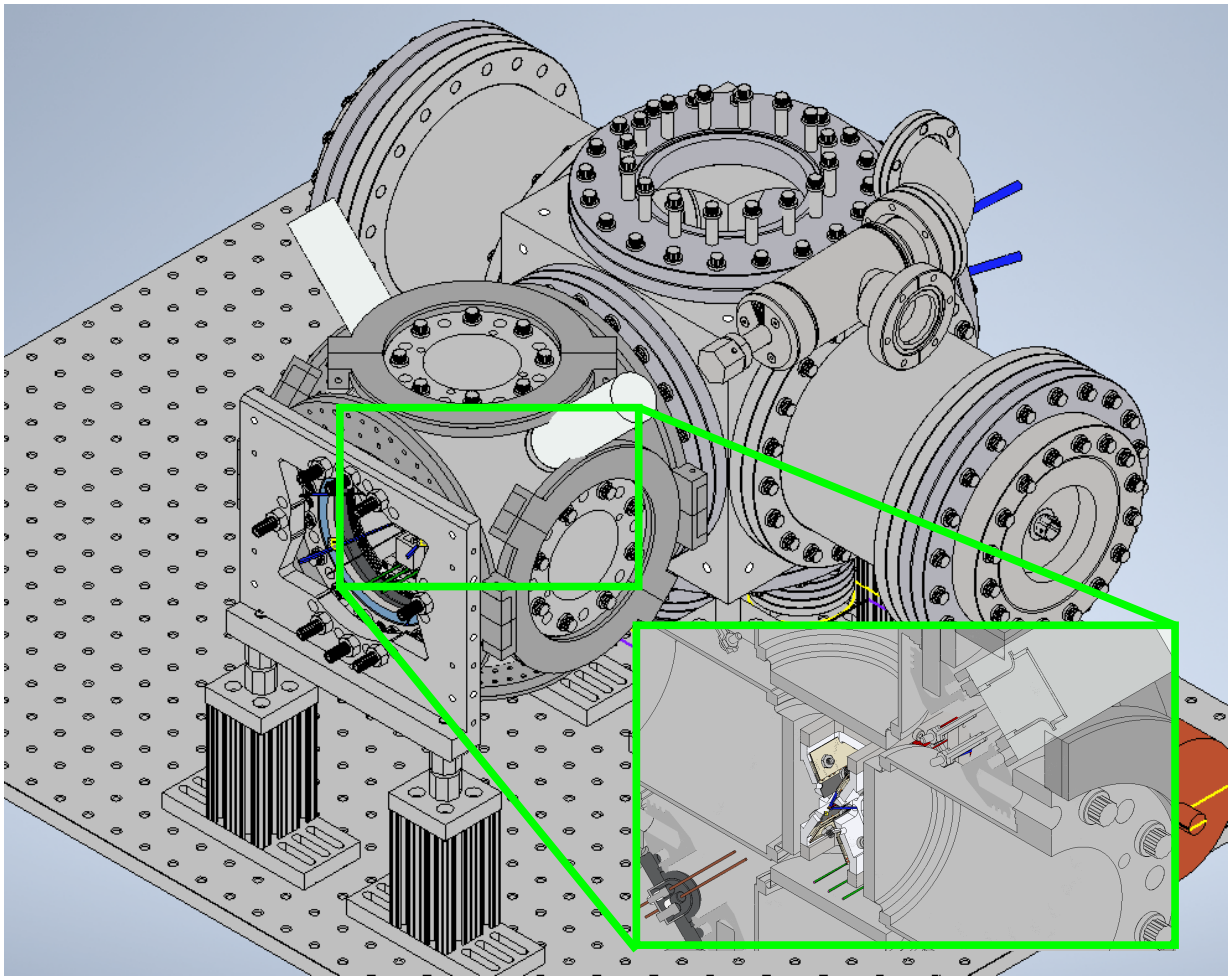

Figure 6.1: 3D design of the next-generation ion trap. The inset shows the crosssection of the internal structure of the trap.

powered by the digital micromirror device (DMD) described in chapter 4 for individual spin readout and reset. A cross-section of the trap and the reentrant windows is shown in Fig. 6.3. In the figures, R1 and R2 denote the two Raman beams entering the trap from the horizontal reentrant windows, while D1 denotes the DMD beam entering the trap from the vertical reentrant window.

6.4 Optical Design

Shown in Fig. 6.3 is an overview of the optical design of the individual Raman addressing system. The system can be divided into two modules: the beam preparation module and the individual addressing module.

The beam preparation module is responsible for modulating the frequency of the Raman beams and can be used as a fast global intensity switch. The Raman beams will be split into two beams and individually modulated with the AOMs. The two Raman beams are then coupled into their own fibers and delivered to the individual addressing module.

The individual addressing module is responsible for creating individually focused beam spots and controlling the power of each beam spot individually. The created beam spots are mapped to the ions in the trap. The individual addressing module consists of two sets of optics that are mirrored from two sides of the trap, corresponding to the two Raman beams.

6.4.1 Beam Preparation Module

In this module, the laser (355 nm) is branched and split into two beam paths. Each beam path is modulated by an AOM with a double-path configuration. By using a double-pass AOM, we are able to modulate the optical frequency with different RF frequencies without affecting the beam pointing.

It's worth noting that most of the commercially available UVFS AOMs, which have good transmission for the 355 nm laser, prefer vertical polarization.

We believe one of the reasons is that these AOMs are using longitudinal acoustic waves, which are known to have stronger polarization dependencies. This poses challenges for the typical double-pass configuration.

A few workarounds are:

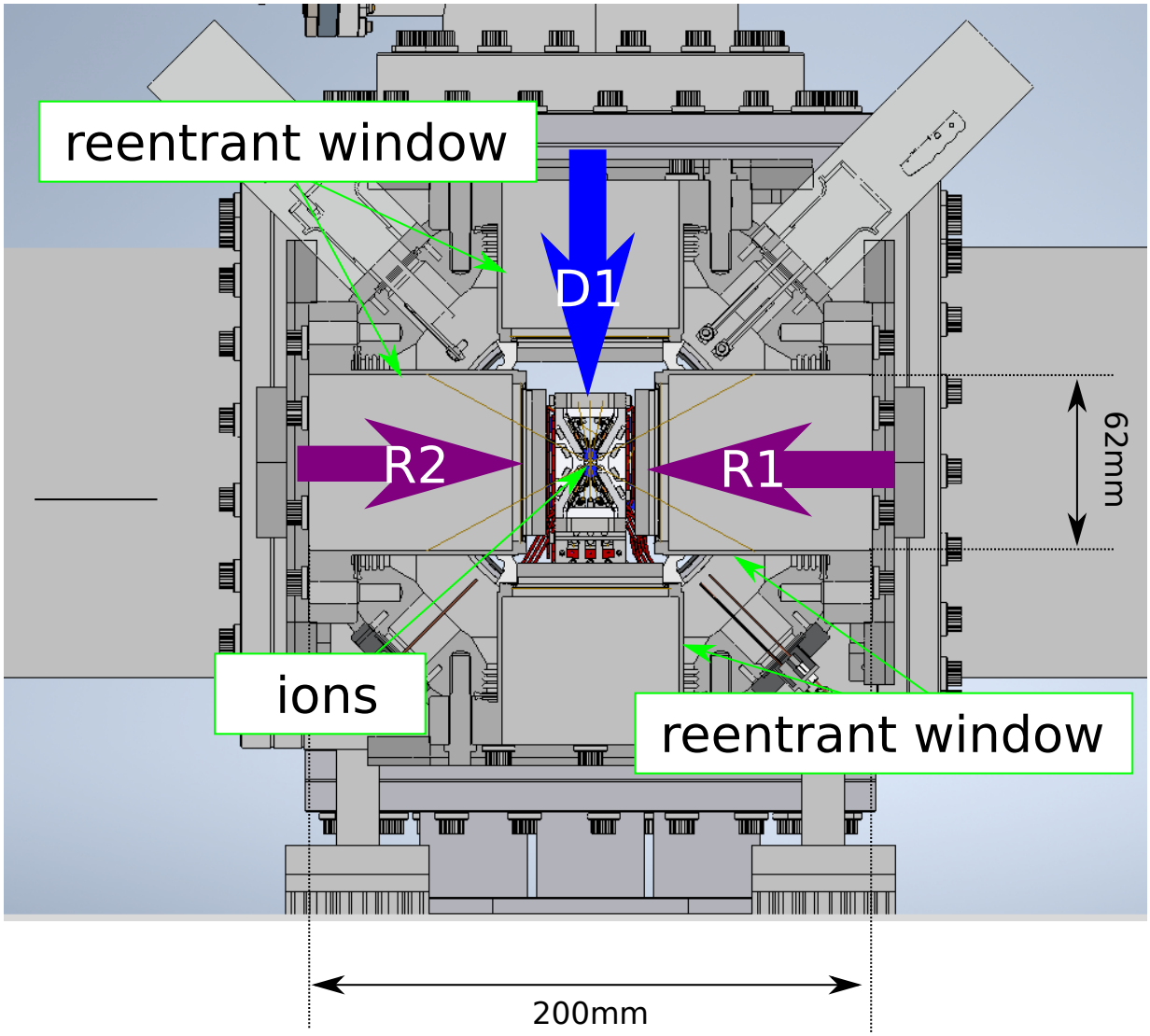

Figure 6.2: Cross-section of the trap and the reentrant windows. R1 and R2 are the two Raman beams entering the trap from the horizontal reentrant windows. D1 is the DMD beam entering the trap from the vertical reentrant window. The ions are trapped by the blade electrodes at the center of the trap. The ion chain direction is perpendicular to the plane of the figure.

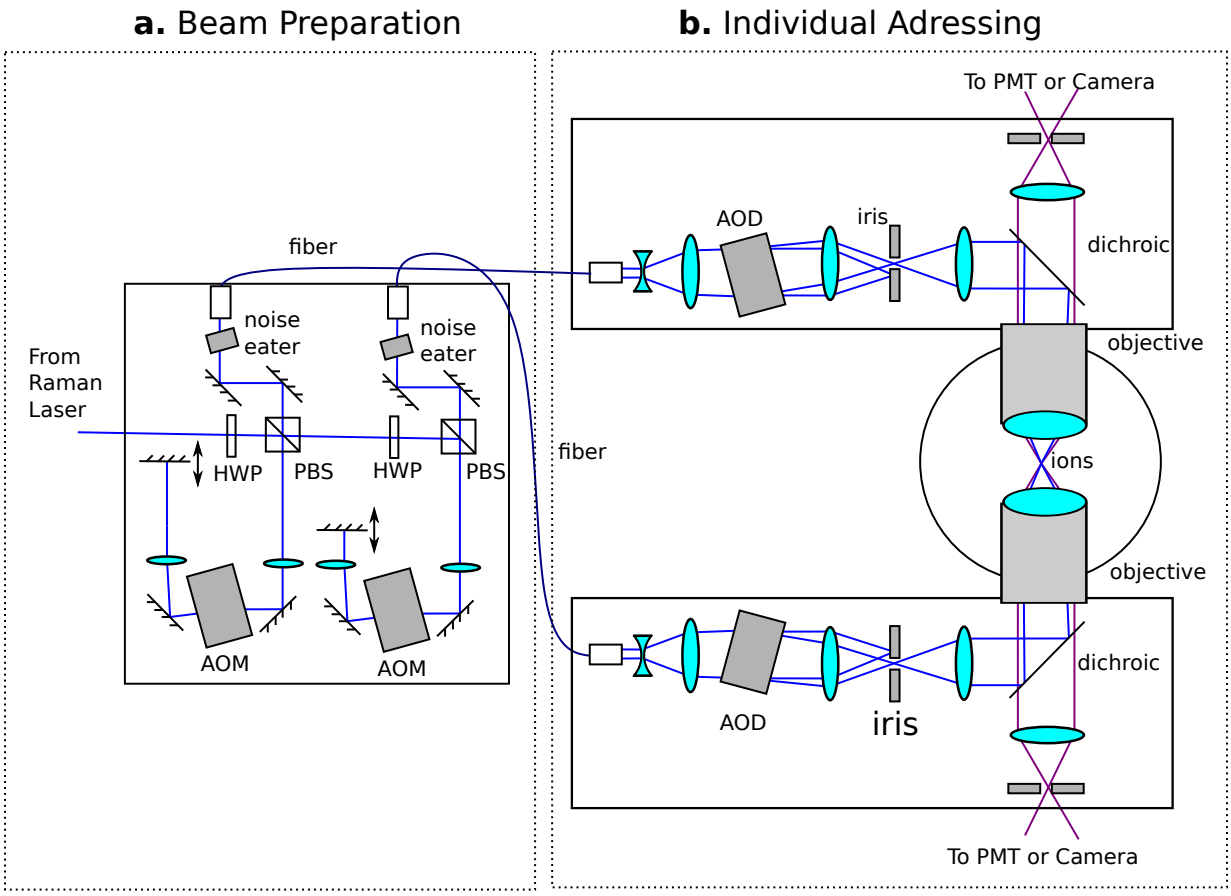

Figure 6.3: Overview of the Raman Optical Design: The Raman module can be divided into two sections, the beam preparation module, and the individual addressing module. The two modules are connected with photonic crystal fibers for beam delivery. **a.** Beam Preparation Module: The Raman beam is split into two beam paths and modulated by AOMs, respectively. The two beams are then coupled into photonic crystal fibers for beam delivery. Noise eater AOMs are used for intensity stabilization. **b.** Individual Addressing Module: The Raman beams are coupled out of the photonic crystal fibers and collimated. The two beams are then expanded by a cylindrical telescope and modulated by AODs. The AODs are fed with multi-tone RF frequencies. Each tone of the RF frequency diffracts the beam at a different angle. The diffracted beams are then focused to create spots that are mapped to different ions.

- Instead of using a quarter-wave plate and a polarization beam splitter to split the forwarding and returning beams, one can use an optical isolator to separate the beam paths. With an optical isolator, both the forwarding and returning beams can maintain the preferred polarization of the AOM.
- Use a shearing mode AOM: As demonstrated in Chang, et al. (2008) [10], more than 40% total efficiency (double-pass) is achieved in UV wavelength with a shearing mode AOM.

Shown in 6.4 is the layout of the beam preparation module. The high level functionality follows the design in Fig. 6.3. Instead of showing two beam paths for the two Raman beams, we have additional beam paths that has identical controls

6.4.2 Beam Delivery with Photonic Crystal Fiber

After the Raman beams have been modulated, the two Raman beams will be coupled to photonic crystal fibers and delivered to the optics close to the chamber.

The use of fiber fulfills a dual purpose. Primarily, it purifies the spatial mode, thus enabling the attainment of near single-mode operation. Furthermore, the use of fiber adds a level of flexibility to the placement of optics, while concurrently preserving the total beam path, which is crucial for the temporal overlap of the two Raman beams pulses as described in section 6.2.

Nevertheless, implementing fiber delivery for Raman beams in the UV wavelength range presents nontrivial challenges. The main obstacles include:

- Solarization Resistance: Conventional UV fibers, composed of fused silica, are susceptible to UV-induced solarization. This phenomenon leads to a gradual and permanent increase in fiber opacity. Solarization-resistant fibers are crucial because they can withstand the effects of solarization and maintain their optical performance over time.
- Power Handling: The Raman process is a two-photon process, meaning it typically requires more power compared to single-photon processes such as Doppler cooling. This necessitates the use of fibers with high power handling capabilities.

To address these issues, Colombe et al. (2014) [13] and Marciniak et al. (2017) [45] demonstrated the application of fiber delivery in the ultraviolet (UV) wavelength range. In

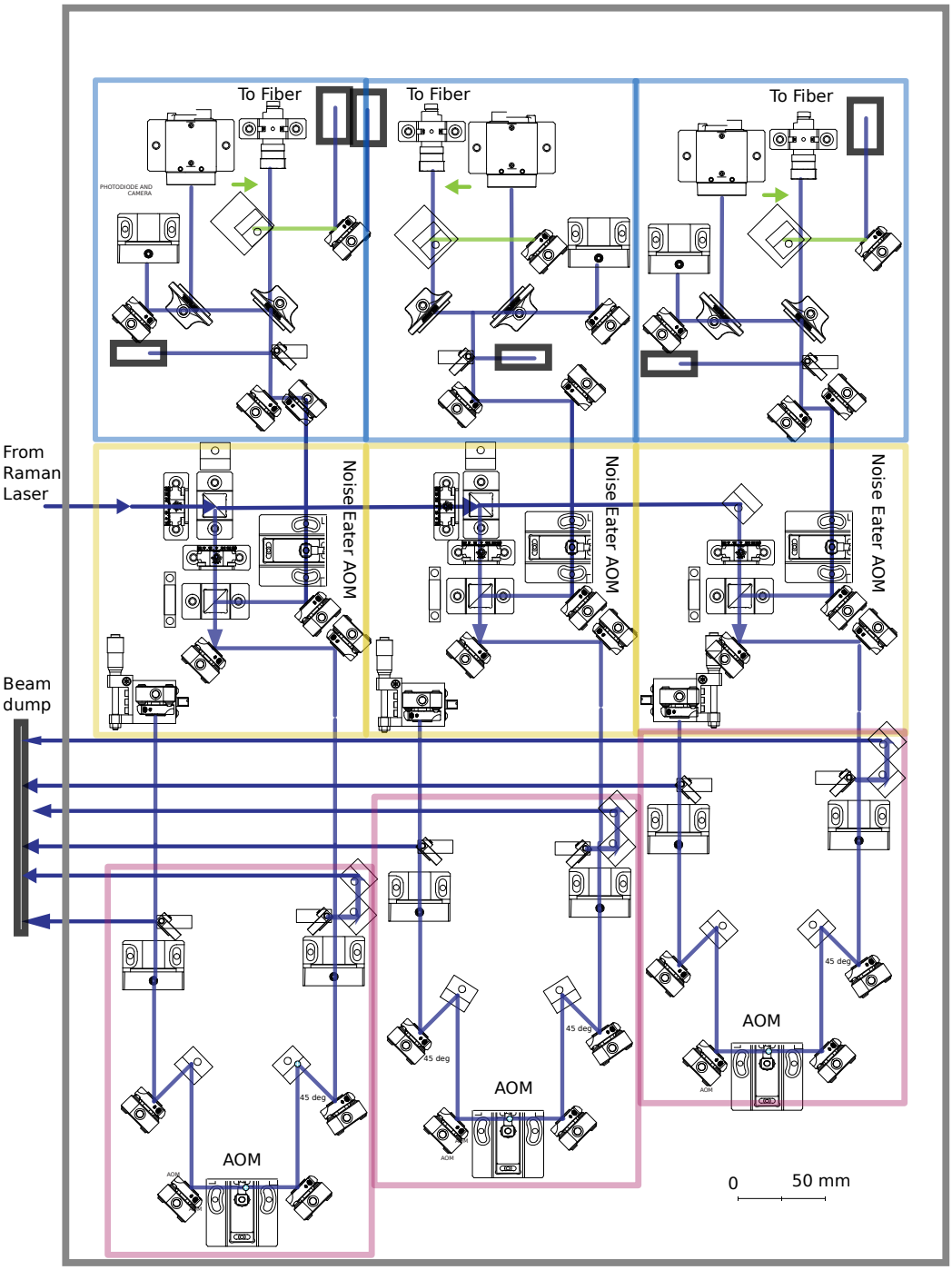

Figure 6.4: Layout of the beam preparation module. This optomechnical design are co-designed by me and Ryan Mark, who worked as a co-op student in our lab.

these studies, endlessly single-mode photonic crystal fibers from NKT Photonics (LMA-10-UV) were employed. These photonic crystal fibers are capable of maintaining single-mode operation even with a larger core diameter (MFD 8.6 μm as opposed to a conventional UV single-mode fiber MFD of 22.5 μm). This effectively reduces the average power density within the fiber.

Additionally, these fibers undergo a process known as hydrogen loading. In this procedure, the optical fiber is exposed to high-pressure hydrogen gas, typically at elevated temperatures[13, 45]. The hydrogen molecules diffuse into the silica matrix of the fiber, where they bond with optically active color centers formed by the UV radiation field propagating through the silica core. This bonding results in the creation of stable, optically passive states that are resistant to UV-induced solarization [34].

In our lab, we are exploring an alternative approach. Instead of using endlessly single-mode photonic fibers, we employ a distinct type of photonic crystal fiber known as hollow-core fiber. As the name implies, this fiber guides light within a hollow region, with only a small fraction of the power transmitted through the solid material.

Since the power density within the glass is minimal, solarization is mitigated. Using a hollow-core Kagome photonic crystal fiber, Gebert et al. (2014) [24] demonstrated near single-mode transmission of 15mW 280 nm continuous wave (CW) light for over 100 hours without any degradation. In contrast, conventional single-mode fibers experienced an 80% drop in transmission after only 3 hours of exposure to 2mW 280 nm lightcitegebert2014damage.

The hollow core fiber we are using is from GLO photonics. This hollow core fiber is optimized for 355 nm and has a mode field diameter of 22 μm. Chafer, et al. (2022)[9] shows no signatures of degradation in transmission for continuous exposure to 355 nm laser with 1 kHz repetition rate and 5 mW average power, and Leroi, et al. (2023)[40] further shows 20 W average power solarization-free transmission for 343 nm laser with 150 kHz repetition rate and 10 ns pulse width.

In our lab, we've tested it with 100 W of 355 nm laser with no evidence of solarization. Our current transmission is about 75% which is less than the 92% result shown in Leroi, et al. (2023)[40]. This is due to the imperfect mode profile. Our M^2 value is measured to be around 1.4. We are aiming for increasing the coupling efficiency by using a pin-hole.

6.4.3 Overview

The figure 6.5 provides an overview of the optical design of the imaging system.

The Raman beam is first collimated and then expanded by a cylindrical telescope at a ratio of 2.5, which increases the coverage of the acousto-optic modulator's (AOD) aperture. Different tones of the RF frequencies driving the AOD diffract the beam at various angles. These diffracted beams are subsequently focused by a triplet lens with an effective focal length of 570 mm, creating multiple spots. These spots are then relayed to the ion image plane at approximately 13 times demagnification.

The setup is mirrored on the other side of the chamber. The two individual addressing systems control the Raman beams to create the required beat note to drive the Raman transition.

In this configuration, the AOD serves to control the intensity and phase directed at individual ions. Even though each addressing beam has a different tone, as they are modulated by distinct RF frequencies, the frequency difference between the beams from the two sides remains consistent across the image plane, courtesy of the mirrored setup.

The AOD we selected is CQD3-120-80-355-X from Brimrose. It has an 80 MHz scanning range (corresponding to 5 mrad), about 80% diffraction efficiency, and 98% optical transmission.

The triplet lens post-AOD is employed to fine-tune and match the magnification of the addressing systems from both sides. By utilizing a triplet, we are able to adjust the focusing power while ensuring the beam continues to focus on the intermediate image plane.

The microscope objective is from Photon Gear. The objective has a 0.45 NA and is designed to work with both 355 nm and 369 nm, and it is also used for imaging. The Raman addressing system doesn't use the full NA of the objective.

6.4.4 Apodization

The number of addressable ions is ultimately limited by the bandwidth of AOD.

For an AOD, the diffraction angle satisfies the Bragg conditions. For the first-order diffraction beam, the Bragg angle is given by

$$\theta_B = \sin^{-1} \frac{\lambda}{2\Lambda} \tag{6.1}$$

where λ is the wavelength of the incoming beam, and Λ is the wavelength of the acoustic wave in the AOM's crystal. Given the Bragg angle θ_B, the wave vector $\boldsymbol{k_\nu}$ along with the

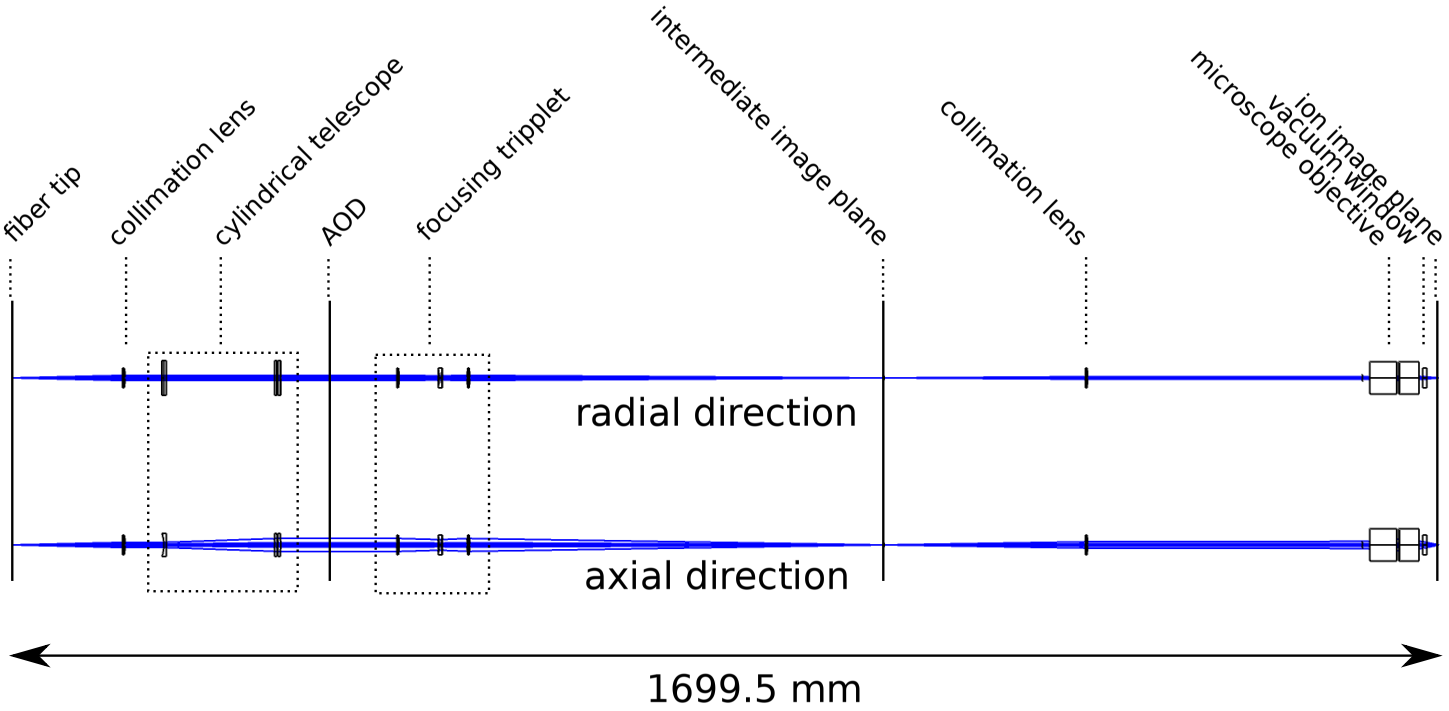

Figure 6.5: Overview of the Raman individual addressing optical design.

acoustic-wave propagating direction that is added to the diffracted beam, and its value can be expressed as

$$k_\nu = 2k_0 \sin\theta_B = \frac{k_0\lambda}{\Lambda} = 2\pi\frac{1}{\Lambda} \tag{6.2}$$

where k_0 is the value of the wave vector of the incident beam. The wavelength of the acoustic wave is determined by the speed of sound in the crystal v and the modulation frequency ν:

$$k_\nu = 2\pi\frac{\nu}{v} \tag{6.3}$$

As we've shown previously in Eq. 4.1, the lens performs an optical Fourier transformation that maps beams with different wave vectors to different positions on the image plane. The scaling factor between the wave vector and the position is $\frac{\lambda f}{2\pi}$. A larger bandwidth of the AOD allows it to diffract the beam at a wider angle, corresponding to a more significant range of wave vector and enabling the addressing of more ions.

In terms of the spot size, a Gaussian beam with a $1/e^2$ radius w_0 has its Fourier transformation as:

$$\mathcal{F}\left[e^{-\frac{x^2}{w_0^2}}\right] \propto e^{-\frac{k^2}{(2/w_0)^2}} = e^{-\frac{k^2}{k_w^2}} \tag{6.4}$$

The waist radius of the Gaussian beam in Fourier space, k_w, is inversely proportional to the beam waist:

$$k_w = \frac{2}{w_0} \tag{6.5}$$

The beam waist at the image plane is associated with the same scaling factor $\frac{\lambda f}{2\pi}$. Hence, the larger the beam coverage on the AOD, the smaller beam spot size one can create, leading to more site-resolved beam spots.

Given that both the spot size and the addressable field of view scale with the same factor, the number of site-resolved spots is independent of the system's effective focal lengths and the laser being used. Instead, it depends on the speed of sound of the AOD crystal, the beam size at the AOD, which is ultimately constrained by the device's aperture, and the AOD's bandwidth.

If we uniformly illuminate an aperture, the resultant spot would display an Airy pattern. Conversely, if the aperture is illuminated with a Gaussian profile, the spot would also adopt a Gaussian profile. While the Airy pattern has a smaller central lobe, its side lobes fall off more slowly. The Gaussian profile, on the other hand, has a larger central lobe, but the intensity drops off more rapidly, leading to less cross-talk.

In our design, we have implemented an apodization factor of about 2.5 along the RF direction, which means the $1/e^2$ Gaussian radius is 2.5 times smaller than the aperture's

radius. We chose this apodization factor to ensure that we achieve less than 10^{-4} level cross-talk at the 4 μm position, without unduly enlarging the spot size.

The AOD we selected features a rectangular window of 7 mm by 10 mm. The longer axis is aligned with the RF direction, providing adequate coverage for our purposes. Given that the shorter axis direction corresponds to the radial direction of the ion chain, cross-talk is not a primary concern, therefore allowing for a lower apodization ratio.

6.4.5 Telecentricity compensation

The coupling between the spin state and motional state can be quantified by the Lamb-Dicke parameter $\eta_{im} = \delta k b_{im} \xi_m^{(0)}$ as mentioned in Sec. 2.5.2.

For the Raman transition, since it is a two-photon process, the δk here corresponds to the direction of the beat note for the two Raman beams, which is the difference of the wave vectors of the two Raman beams.

Therefore, it's important for the individual addressing beams of the Raman beam to be parallel to each other, so the Lamb-Dicke parameters for the different ions are uniform.

To achieve this, one can use a telecentric imaging system. Typically, a 4-f imaging system is used for this purpose. In the 4-f imaging system, the two lenses relaying one image plane to another are separated by the sum of the focal lengths of the two lenses. In this configuration, the Fourier plane of the two lenses resides in the same plane.

Compared to an imaging system with arbitrary separation between the two lenses, the beam pointing is preserved. We are able to use this property to maintain the telecentricity from one image plane to another. The typical way is to place the AOD in the Fourier plane of a lens and use the 4-f imaging system to relay the beam from the intermediate image plane to the ion image plane. However, the disadvantage of the 4-f imaging system is its requirement for lengthy spacing between the two lenses.

Nevertheless, it's not always necessary to use a 4-f imaging system in our application. In fact, intermediate image plane telecentricity is not required. Only image space telecentricity is necessary. Namely, it only requires us to have the beams to be telecentric at the ion image plane. The beams don't have to be telecentric at the intermediate image plane. Meaning, we don't need to place the AOD in the Fourier plane, and we don't need the imaging relay to follow a 4-f configuration. We are able to adjust the separation between the AOD and lens and the separation between the two lenses of the relay as long as the image plane telecentricity is maintained.

As a result, when we design the addressing system, we only constrain the telecentricity at the last image plane (where ions reside). The way we do this is to use the EXPP operand in the merit function of the optical design software (We use Zemax Optics Studio) while performing optimization.

The EXPP operand calculates the (paraxial) exit pupil position with respect to the image surface. We can target the EXPP operand to a very large value. This effectively constrains the telecentricity at the image plane, as the parallel rays at the image plane have an exit pupil at infinity.

With this method, we can aim for a shorter total optical path than the 4-f imaging system while maintaining the telecentricity at the ion image plane.

Shown in Fig. 6.6, we display the incident angle relative to the image height of our design, simulated with Zemax Optics Studio. We can see that at the ion image plane we maintain a 0-degree incident angle of the chief ray throughout the field of view (FOV). On the other hand, the incident angle of the beam at the intermediate image plane increases as the image position shifts away from the center of the FOV. The two plots are simulated with the same aperture. The difference in magnification results in different sizes of the FOV in the plot. Though 0.5 degrees in the intermediate image plane may seem to be a small number, the corresponding tilt without proper compensation at the ion image plane can be much larger due to the demagnification between the two image planes.

6.4.6 Results: Optical Performance

As depicted in Fig. 6.7, we demonstrate that we can achieve less than 10^{-4} crosstalk error at the center and the edge (200 μm) of the FOV. It's possible to further reduce the crosstalk error by increasing the apodization factor. However, doing so will also increase the spot size, and the aberration from manufacturing errors or imperfect alignment will become more significant as the spot size expands.

If varying the apodization ratios is desired, one can easily do so by adjusting the telescope before the AOD. Since the beams before and after the AOD are collimated, the effort required to realign the optics should be minimal.

The scanning range of the AOD we are using has a 5 mrad scanning range. This translates to about a 200 μm scanning range ($\pm$100 μm) of the FOV. With 4 6 μm ion-ion spacing, we are able to address $30 \sim 50$ ions. We will discuss the scalability and approaches to increase the addressing range in the next section (Sec. 6.4.7).

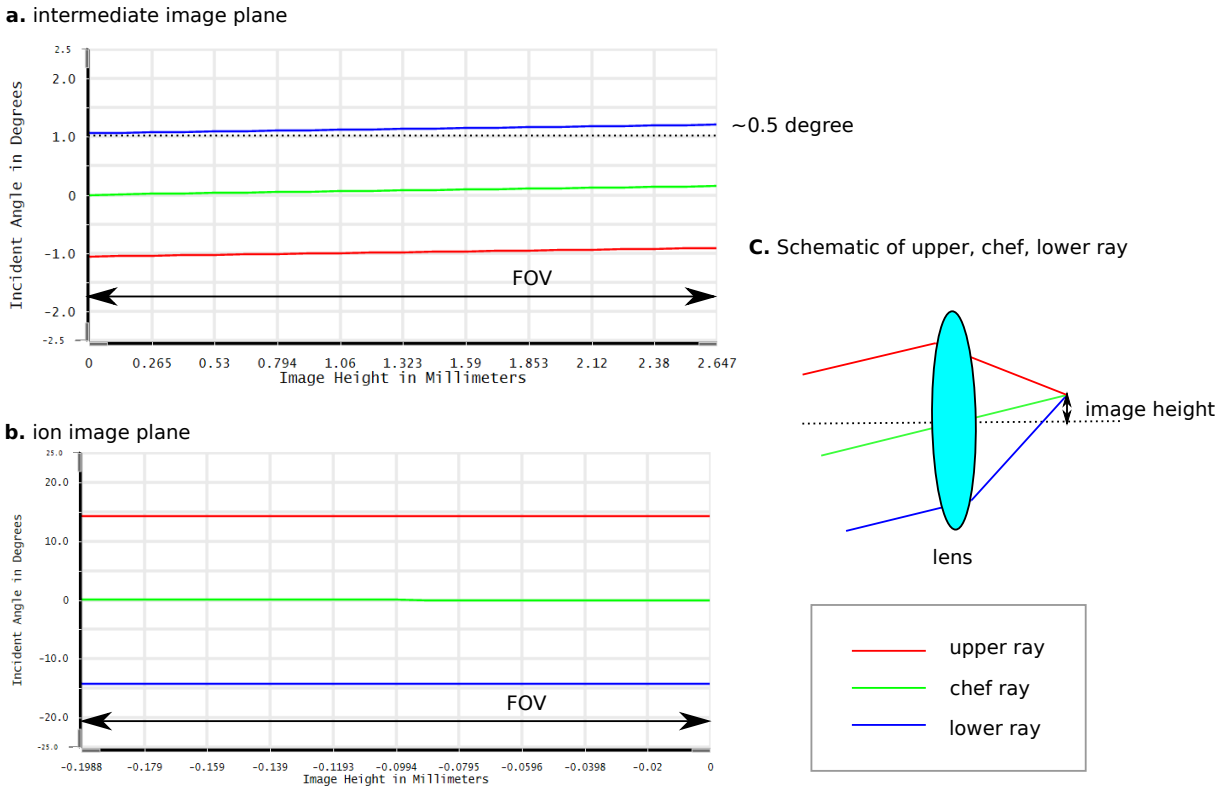

Figure 6.6: Incident angles versus image height at intermediate image plane and ion image plane. Note that the plotted range corresponds to the full FOV. Due to the different magnifications, image height at the ion image plane is about 13 times smaller than that at the intermediate image plane. **a.** Intermediate image plane. There is a 0.5 degree tilt at the edge of the FOV. **b.** Ion image plane. **c.** Schematic of showing the upper, chef, and lower ray. Note that the image is reversed between the intermediate image plane and the ion image plane.

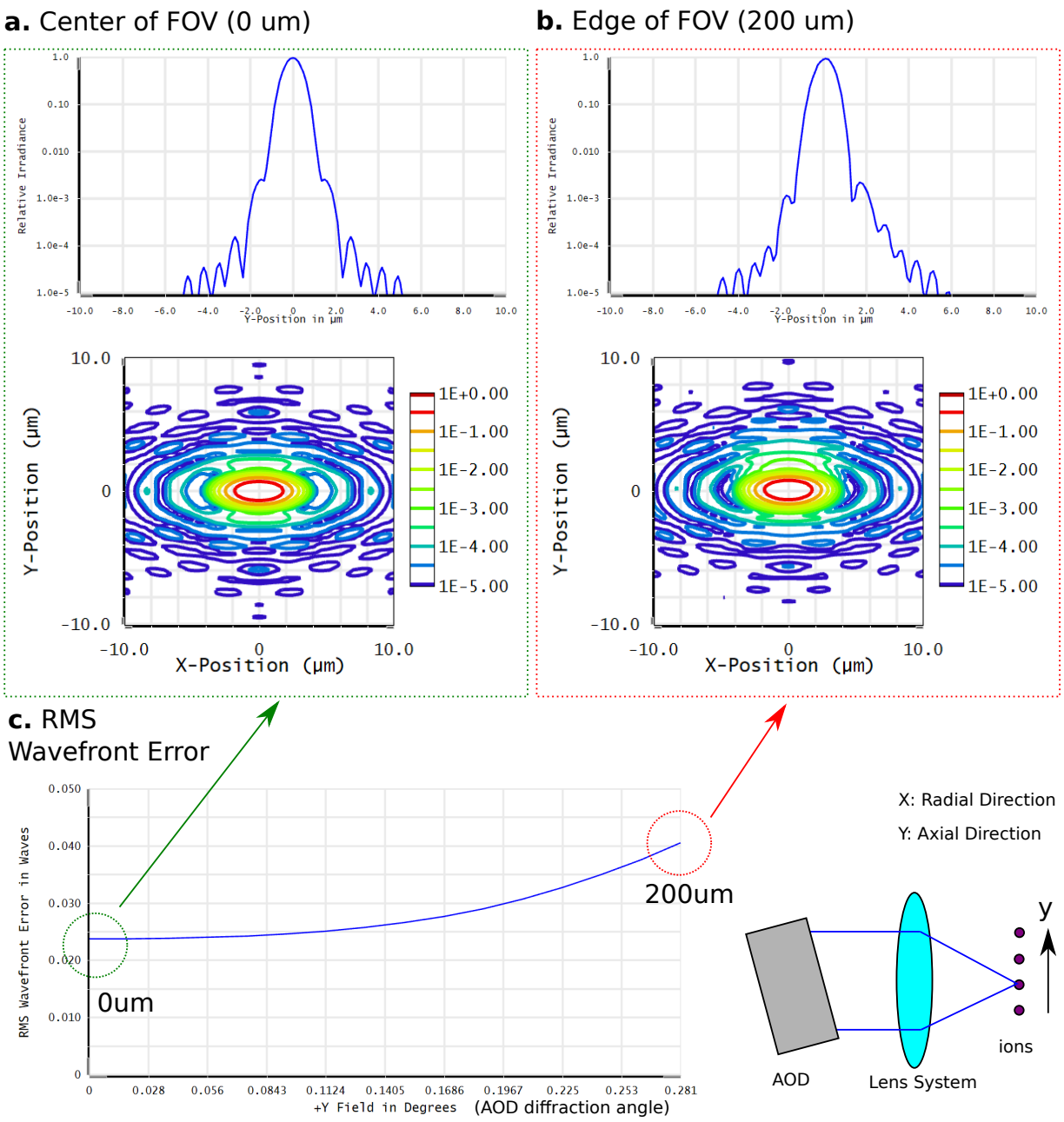

Figure 6.7: Optical performance of the individual Raman addressing system. The simulation is performed with an apodization factor of 2.5 and a wavelength of 355 nm. **a.** The point spread function (PSF) of the system at the center of the field. We plot the 2D PSF and the 1D PSF along the axial direction of the ion chain. **b.** The PSF of the system at the edge of the field (200 μm away from the center). **c.** RMS wavefront error across the FOV.

6.4.7 Discussion: Scalability

The scalability of site-resolved spots is largely governed by the bandwidth of the AOD. However, there are other parameters to consider in improving this scalability.

Firstly, the aperture of the AOD could be increased. A larger aperture can yield smaller spot sizes, thereby increasing the number of resolvable spots.

Secondly, we could consider using an AOD with a slower speed of sound, which would result in larger diffraction angles and hence, more addressable spots. The speed of sound in an acoustic wave is dependent not just on the crystal material used in the AOD, but also on the mode of the acoustic wave. For instance, the shear mode generally has a slower speed of sound compared to the longitudinal mode.

As for the choice of material, tellurium dioxide (TeO_2) has a slower speed of sound than fused silica, but its transmission properties are inferior under UV wavelengths. However, this may not be a problem for other ion species, for instance, the system that uses Barium ions typically uses 532 nm laser for Raman beams, which is in the visible range and has excellent transmission in TeO_2.

While both methods can effectively increase the number of acoustic waves covered within the aperture (and hence the number of site-resolved spots), they also come with their own disadvantages. For example, both methods lead to longer rise and fall times for the AOD, as the time taken for the acoustic waves to propagate through the larger aperture increases.

Regarding power scaling, our design is optimal. Except for the unmodulated zeroth order beam of the AOD, there is no waste of power. The power scales linearly with the number of ions that need to be addressed simultaneously. Compared to the multi-channel AOM, the power is not wasted on the unused channels. Namely, it's possible to provide more power when addressing a subset of ions.

6.5 Conclusion

In this chapter, we discussed the design of the individual addressing system for Raman beams for our next-generation ion trap apparatus. The design is based on the criteria we identified in Sec. 6.2 to ensure the system is capable of operating for a large number of ions ($30 \sim 50$).

Our design approach separates the beam modulation from individual addressing controls. To facilitate this, we employ a solarization-free hollow core photonic crystal fiber to

connect the two modules. Utilizing this fiber not only simplifies the mechanical design but also allows for greater flexibility in the positioning of optics.

We have demonstrated the capability of our design to create site-resolved spots with a crosstalk error of less than 10^{-4} at a 4 μm ion-ion spacing with simulation. Impressively, this performance is maintained even at the edge of the FOV ($\pm$200 μm). Although the existing AOD is capable of scanning about half of the FOV, the optical design is capable of maintaining the low cross talk error over the full FOV. Future upgrades will allow us to unlock the full potential of the optical design.

Moreover, we have discussed the potential scalability of our system and identified several strategies for increasing the number of addressable ions. In brief, this could be achieved by employing an AOD with a slower acoustic wave speed, larger aperture, or broader scanning bandwidth.

Chapter 7

Conclusion

In this thesis, we present our work on building a four-rod trapped ion apparatus for quantum operations and engineering the necessary optical controls for coherent and non-coherent quantum operations.

For the four-rod apparatus, my main contributions center around the optics for imaging systems and laser systems, including beam preparation, shaping, and delivery. We demonstrate engineering a high-density and stable optical pegboard. Compared to the traditional approach of building optical boards with pedestals and forks, it allows us to compactly place the optics and reduce the beam height from the baseboard, thereby increasing the stability.

For the imaging system, we presented the optical design of a 0.2NA home-made objective built with all in-stock lenses. We also conducted a detailed analysis comparing camera sensor technologies between qCMOS and EM-CCD. We demonstrated that qCMOS is capable of high-fidelity state detection and offers a significant advantage in scalability. Unlike the CCD that reads out counts pixel by pixel, the CMOS technique allows reading out a full row of pixels simultaneously. This increases the duty cycle of the experiment when working with a long chain of ions.

We also demonstrated classification of qubit states with the random forest algorithm, a machine learning algorithm. Unlike simple threshold on the histogram, the random forest algorithm is robust against increasing readout noise as the region of interest expands. This is particularly useful when dealing with the CMOS-based imaging sensor, as readout noise is the dominant source of error.

For the non-coherent quantum control, such as state measurement and initialization, it generally has more stringent requirements on precision and the crosstalk error. Unlike

the coherent quantum operations, the non-coherent operations acting on the qubit states are generally irreversible. Leakage to the neighboring ions can result in the collapse of the quantum states. Our individual addressing system utilizing the holographic beam shaping, discussed in chapter 4, is an ideal solution. The holographic beam shaping is performed with Fourier holograms displayed on a digital micromirror device. The use of holograms allows us to actively correct optical aberrations that may result from the manufacturing error of the optical elements or the misalignment of optics. We demonstrated using a single ion as a sensor to characterize the existing aberration in the system, all the way to the ion plane. We showed the aberration can be compensated down to less than $\lambda/20$ RMS error. This is beyond most of the specifications of commercial optics.

To verify the quality of the individual addressing beam, we developed a quantum sensing technique with ions to measure the beam's intensity. This technique is extremely power-efficient and highly sensitive, as only a few photons are needed for optical pumping. It allows us to characterize intensity with a high dynamic range. In addition, the technique is immune to undesired scattering from the addressing beam entering the imaging system. This makes it possible to have an individual addressing beam and share the same microscope objective with the imaging system, thus saving limited resources of optical access.

We showed that the imaging system can suppress the relative crosstalk error down to a 10^{-4} level. This translates to 99.9% fidelity in resetting the spin of an ion without affecting the quantum state of the neighboring ion. Assuming the use of a state-of-the-art detector from Crain, et al. (2019)[15], it's possible to achieve 99.6% fidelity of individual spin readout without affecting the neighboring ion. Note that these results do not require shuttling the ions or relaxing the axial trap potential to expand the ion-ion spacing, offering a significant advantage in time usage and not disrupting the phonon Hilbert space.

As for the coherent quantum operations, they typically require more power compared to non-coherent quantum operations. This is because most of them rely on second-order processes, such as $S \rightarrow D$ narrow-line transitions or coherent two-photon Raman transitions. Consequently, the holographic beam shaping may not be feasible for working with a large number of ions due to its suboptimal power scaling. In chapter 6, we presented our design for an individual addressing system for Raman beams. We also showed that there is a clear route for scaling the addressable field of view of the system by increasing the number of micromirrors contained in the Fourier plane.

The design uses acousto-optic deflectors (AOD) to create individual beam spots that map to individual ions. We used a mirrored setup for the two Raman beams, so the site-dependent frequency shifts from the AOD are compensated. We examined the effect of

apodization on crosstalk and showed that the design is capable of creating sub-10^{-4} level crosstalk for $\sim 4-6$ μm inter-ion spacing. Our solution offers optimal scaling of power with respect to increasing the number of simultaneously addressable spots.

The Raman addressing system is designed to be image-space telecentric. Namely, the individual addressing beams have the same beam pointing at the ion image plane. The uniform beam pointing ensures minimal spin-phonon coupling to the axial mode. We showed practical techniques for designing such an image-space telecentric optical system while reducing the total length of the beam path, as 4-f imaging systems usually have a long optical beam path.

Along with the addressing system, we also presented work on design of beam preparation optics. We adopted a modular approach that separates the Raman beam preparation into a separate module. We used hollow-core photonic crystal fibers to deliver the beams from the beam preparation module to the individual addressing system module. The use of the fiber simplifies the routing of the optics and reduces the complexity of the optics surrounding the chamber.

Beyond individual addressing and spatial quantum control, we also explored the temporal aspect of quantum controls. In this thesis, we present the work of implementing complex Hamiltonians that require multiple phase-referenced RF frequencies and time-dependent controls with an arbitrary waveform generator (AWG).

With the capability to engineer complex Hamiltonians, we also present our study on emerging conservation laws in strongly interacting Floquet systems. More specifically, we are interested in the dynamic freezing behavior in a transverse Ising system with strong Floquet drive. The Floquet drive is a field along the spin operators of the spin-spin interaction and periodically flips its sign.

We experimentally observed the dynamic freezing behavior of total magnetization. For states sharing the same magnetization, we observed dynamics between them. Our works of experimentally demonstrating the emerging conservation law in an interacting, chaotic quantum many-body system under strong Floquet drive, of which such phenomenon is unexpected and intriguing. This sheds the light on in structuring the Hilbert space and engineering in stable Floquet quantum systems[26].

7.1 Final Remarks

Throughout this work, we have developed and demonstrated various techniques and methodologies for engineering scalable individual optical addressing for both coherent and non-

coherent quantum operations in trapped ion quantum apparatus. The addressing systems we presented can be readily adopted in apparatuses with different ion species, and potentially applied to other quantum information processing platforms that also require optical controls for quantum state manipulation.

Our work exploring dynamic freezing in the strongly interacting quantum system with Floquet drive presents preliminary experimental evidence supporting the theory. The temporal controls implemented with arbitrary waveform generation enable the exploration of complex and time-dependent Hamiltonians.

Moving forward, we aim to conduct a more detailed study and explore the possibility of connecting the system to a controlled environment. This line of inquiry can further our understanding of the intricacies of open quantum systems.

References

[1] CJ Ballance, TP Harty, NM Linke, MA Sepiol, and DM Lucas. High-fidelity quantum logic gates using trapped-ion hyperfine qubits. *Physical review letters*, 117(6):060504, 2016.

[2] AG Basden, CA Haniff, and CD Mackay. Photon counting strategies with low-light-level ccds. *Monthly notices of the royal astronomical society*, 345(3):985–991, 2003.

[3] RW Berends, EH Pinnington, B Guo, and Q Ji. Beam-laser lifetime measurements for four resonance levels of yb ii. *Journal of Physics B: Atomic, Molecular and Optical Physics*, 26(20):L701, 1993.

[4] DJ Berkeland and MG Boshier. Destabilization of dark states and optical spectroscopy in zeeman-degenerate atomic systems. *Physical Review A*, 65(3):033413, 2002.

[5] Ali Binai-Motlagh, Matthew Day, Nikolay Videnov, Noah Greenberg, Crystal Senko, and Rajibul Islam. A guided light system for agile individual addressing of ba^+ qubits with 10^{-4} level intensity crosstalk. *arXiv preprint arXiv:2302.14711*, 2023.

[6] Alexander Braun. *Addressing Single Yb_1hn+ Ions: A New Scheme for Quantum Computing in Linear Ion Traps;[Experimente Durchgeführt Am Institute Für Laser-Physik Der Universität Hamburg]*. Cuvillier Verlag, 2007.

[7] Joseph W Britton, Brian C Sawyer, Adam C Keith, C-C Joseph Wang, James K Freericks, Hermann Uys, Michael J Biercuk, and John J Bollinger. Engineered two-dimensional ising interactions in a trapped-ion quantum simulator with hundreds of spins. *Nature*, 484(7395):489–492, 2012.

[8] WC Campbell, J Mizrahi, Q Quraishi, C Senko, D Hayes, D Hucul, DN Matsukevich, P Maunz, and C Monroe. Ultrafast gates for single atomic qubits. *Physical review letters*, 105(9):090502, 2010.

[9] M Chafer, JH Osório, A Dhaybi, François Ravetta, F Amrani, F Delahaye, B Debord, Cristelle Cailteau-Fischbach, Gérard Ancellet, F Gérôme, et al. Near-and middle-ultraviolet reconfigurable raman source using a record-low uv/visible transmission loss inhibited-coupling hollow-core fiber. *Optics & Laser Technology*, 147:107678, 2022.

[10] Chih-Hao Chang, RK Heilmann, ML Schattenburg, and P Glenn. Design of a double-pass shear mode acousto-optic modulator. *Review of Scientific Instruments*, 79(3), 2008.

[11] Soonwon Choi, Joonhee Choi, Renate Landig, Georg Kucsko, Hengyun Zhou, Junichi Isoya, Fedor Jelezko, Shinobu Onoda, Hitoshi Sumiya, Vedika Khemani, et al. Observation of discrete time-crystalline order in a disordered dipolar many-body system. *Nature*, 543(7644):221–225, 2017.

[12] Juan I Cirac and Peter Zoller. Quantum computations with cold trapped ions. *Physical review letters*, 74(20):4091, 1995.

[13] Yves Colombe, Daniel H Slichter, Andrew C Wilson, Dietrich Leibfried, and David J Wineland. Single-mode optical fiber for high-power, low-loss uv transmission. *Optics express*, 22(16):19783–19793, 2014.

[14] S Crain, E Mount, S Baek, and J Kim. Individual addressing of trapped 171yb+ ion qubits using a microelectromechanical systems-based beam steering system. *Applied Physics Letters*, 105(18):181115, 2014.

[15] Stephen Crain, Clinton Cahall, Geert Vrijsen, Emma E Wollman, Matthew D Shaw, Varun B Verma, Sae Woo Nam, and Jungsang Kim. High-speed low-crosstalk detection of a 171yb+ qubit using superconducting nanowire single photon detectors. *Communications Physics*, 2(1):97, 2019.

[16] Stefanie Czischek, Giacomo Torlai, Sayonee Ray, Rajibul Islam, and Roger G Melko. Simulating a measurement-induced phase transition for trapped-ion circuits. *Physical Review A*, 104(6):062405, 2021.

[17] Zohreh Davoudi, Mohammad Hafezi, Christopher Monroe, Guido Pagano, Alireza Seif, and Andrew Shaw. Towards analog quantum simulations of lattice gauge theories with trapped ions. *Physical Review Research*, 2(2):023015, 2020.

[18] Shantanu Debnath, Norbert M Linke, Caroline Figgatt, Kevin A Landsman, Kevin Wright, and Christopher Monroe. Demonstration of a small programmable quantum computer with atomic qubits. *Nature*, 536(7614):63, 2016.

[19] Samuel Earnshaw. On the nature of the molecular forces which regulate the constitution of the luminiferous ether. *Transactions of the Cambridge Philosophical Society*, 7:97, 1848.

[20] CL Edmunds, TR Tan, AR Milne, A Singh, MJ Biercuk, and C Hempel. Scalable hyperfine qubit state detection via electron shelving in the 2 d 5/2 and 2 f 7/2 manifolds in 171 yb+. *Physical Review A*, 104(1):012606, 2021.

[21] Laird Egan, Dripto M Debroy, Crystal Noel, Andrew Risinger, Daiwei Zhu, Debopriyo Biswas, Michael Newman, Muyuan Li, Kenneth R Brown, Marko Cetina, et al. Fault-tolerant operation of a quantum error-correction code. *Preprint at https://arxiv.org/abs/2009.11482*, 2020.

[22] Nicolai Friis, Oliver Marty, Christine Maier, Cornelius Hempel, Milan Holzäpfel, Petar Jurcevic, Martin B Plenio, Marcus Huber, Christian Roos, Rainer Blatt, et al. Observation of entangled states of a fully controlled 20-qubit system. *Physical Review X*, 8(2):021012, 2018.

[23] Alexander L Gaunt and Zoran Hadzibabic. Robust digital holography for ultracold atom trapping. *Scientific reports*, 2:721, 2012.

[24] Florian Gebert, MH Frosz, T Weiss, Y Wan, A Ermolov, NY Joly, PO Schmidt, and P St J Russell. Damage-free single-mode transmission of deep-uv light in hollow-core pcf. *Optics express*, 22(13):15388–15396, 2014.

[25] Asmi Haldar, Roderich Moessner, and Arnab Das. Onset of floquet thermalization. *Physical Review B*, 97(24):245122, 2018.

[26] Asmi Haldar, Diptiman Sen, Roderich Moessner, and Arnab Das. Dynamical freezing and scar points in strongly driven floquet matter: Resonance vs emergent conservation laws. *Physical Review X*, 11(2):021008, 2021.

[27] TP Harty, DTC Allcock, C J Ballance, L Guidoni, HA Janacek, NM Linke, DN Stacey, and DM Lucas. High-fidelity preparation, gates, memory, and readout of a trapped-ion quantum bit. *Physical review letters*, 113(22):220501, 2014.

[28] Philipp Hauke, David Marcos, Marcello Dalmonte, and Peter Zoller. Quantum simulation of a lattice schwinger model in a chain of trapped ions. *Physical Review X*, 3(4):041018, 2013.

[29] Tin Kam Ho. Random decision forests. In *Proceedings of 3rd international conference on document analysis and recognition*, volume 1, pages 278–282. IEEE, 1995.

[30] Kazi Rajibul Islam. *Quantum simulation of interacting spin models with trapped ions*. University of Maryland, College Park, 2012.

[31] Daniel FV James. Quantum dynamics of cold trapped ions with application to quantum computation. Technical report, 1997.

[32] Sonika Johri, Shantanu Debnath, Avinash Mocherla, Alexandros Singk, Anupam Prakash, Jungsang Kim, and Iordanis Kerenidis. Nearest centroid classification on a trapped ion quantum computer. *npj Quantum Information*, 7(1):122, 2021.

[33] Mingyu Kang, Kai T Liu, Sutirtha N Chowdhury, Jonathon L Yuly, Ke Sun, Jacob Whitlow, Jesús Valdiviezo, Zhendian Zhang, Peng Zhang, David N Beratan, et al. Trapped-ion quantum simulations for condensed-phase chemical dynamics: seeking a quantum advantage. *arXiv preprint arXiv:2305.03156*, 2023.

[34] P Karlitschek, G Hillrichs, and K-F Klein. Influence of hydrogen on the color center formation in optical fibers induced by pulsed uv-laser radiation. part 1: all silica fibers with high-oh undoped core. *Optics communications*, 155(4-6):376–385, 1998.

[35] Nikhil Kotibhaskar. Design and construction of an ion trapping apparatus for quantum simulation experiments. Master's thesis, University of Waterloo, 2019.

[36] Nikhil Kotibhaskar, Noah Greenberg, Sainath Motlakunta, Chung-You Shih, and Rajibul Islam. Fast and high-yield fabrication of axially symmetric ion-trap needle electrodes via two step electrochemical etching. *Review of Scientific Instruments*, 94(3), 2023.

[37] Maria A Kuczmarski and James C Johnston. Acoustic absorption in porous materials. 2011.

[38] R Lange, AA Peshkov, N Huntemann, Chr Tamm, A Surzhykov, and E Peik. Lifetime of the f 7/2 2 level in yb+ for spontaneous emission of electric octupole radiation. *Physical Review Letters*, 127(21):213001, 2021.

[39] Aaron C Lee, Jacob Smith, Philip Richerme, Brian Neyenhuis, Paul W Hess, Jiehang Zhang, and Christopher Monroe. Engineering large stark shifts for control of individual clock state qubits. *Physical Review A*, 94(4):042308, 2016.

[40] Florian Leroi, Frédéric Gérôme, Julien Didierjean, Julien Saby, Fetah Benabid, and Johan Boullet. Uv 20w-class single-mode nanosecond pulse delivery using a vacuum-free/ambient air inhibited-coupling hollow-core fiber. *Applied Physics B*, 129(7):116, 2023.

[41] Norbert M Linke, Dmitri Maslov, Martin Roetteler, Shantanu Debnath, Caroline Figgatt, Kevin A Landsman, Kenneth Wright, and Christopher Monroe. Experimental comparison of two quantum computing architectures. *Proceedings of the National Academy of Sciences*, 114(13):3305–3310, 2017.

[42] Fuan Liu, Zeliang Gao, Guoru Li, Qian Wu, Zhitai Jia, Baitao Zhang, Jingliang He, and Xutang Tao. An α-batemo 2 o 9 acousto-optical q-switch for all-fiber lasers. *IEEE Photonics Technology Letters*, 33(9):445–448, 2021.

[43] Pei Jiang Low, Brendan White, and Crystal Senko. Control and readout of a 13-level trapped ion qudit. *arXiv preprint arXiv:2306.03340*, 2023.

[44] Jiaju Ma, Saleh Masoodian, Dakota A Starkey, and Eric R Fossum. Photon-number-resolving megapixel image sensor at room temperature without avalanche gain. *Optica*, 4(12):1474–1481, 2017.

[45] Christian D Marciniak, Harrison B Ball, Alex T-H Hung, and Michael J Biercuk. Towards fully commercial, uv-compatible fiber patch cords. *Optics Express*, 25(14):15643–15661, 2017.

[46] Esteban A Martinez, Christine A Muschik, Philipp Schindler, Daniel Nigg, Alexander Erhard, Markus Heyl, Philipp Hauke, Marcello Dalmonte, Thomas Monz, Peter Zoller, et al. Real-time dynamics of lattice gauge theories with a few-qubit quantum computer. *Nature*, 534(7608):516–519, 2016.

[47] Christopher Monroe, Wes C Campbell, L-M Duan, Z-X Gong, Alexey V Gorshkov, Paul W Hess, Rajibul Islam, Kihwan Kim, Norbert M Linke, Guido Pagano, et al. Programmable quantum simulations of spin systems with trapped ions. *Reviews of Modern Physics*, 93(2):025001, 2021.

[48] Thomas Monz, Daniel Nigg, Esteban A Martinez, Matthias F Brandl, Philipp Schindler, Richard Rines, Shannon X Wang, Isaac L Chuang, and Rainer Blatt. Realization of a scalable shor algorithm. *Science*, 351(6277):1068–1070, 2016.

[49] William Morong, Fangli Liu, Patrick Becker, KS Collins, Lei Feng, Antonis Kyprianidis, Guido Pagano, Tianyu You, AV Gorshkov, and Christopher Monroe. Observation of stark many-body localization without disorder. *Nature*, 599(7885):393–398, 2021.

[50] Sainath Motlakunta, Nikhil Kotibhaskar, Chung-You Shih, Anthony Vogliano, Darian Mclaren, Lewis Hahn, Jingwen Zhu, Roland Hablützel, and Rajibul Islam. Preserving a qubit during adjacent measurements at a few micrometers distance. *arXiv preprint arXiv:2306.03075*, 2023.

[51] H Ch NAÈgerl, D Leibfried, H Rohde, G Thalhammer, J Eschner, Ferdinand Schmidt-Kaler, and Rainer Blatt. Laser addressing of individual ions in a linear ion trap. *Physical Review A*, 60(1):145, 1999.

[52] Yunseong Nam, Jwo-Sy Chen, Neal C Pisenti, Kenneth Wright, Conor Delaney, Dmitri Maslov, Kenneth R Brown, Stewart Allen, Jason M Amini, Joel Apisdorf, et al. Ground-state energy estimation of the water molecule on a trapped-ion quantum computer. *npj Quantum Inf.*, 6(1):1–6, 2020.

[53] Nhung H Nguyen, Minh C Tran, Yingyue Zhu, Alaina M Green, C Huerta Alderete, Zohreh Davoudi, and Norbert M Linke. Digital quantum simulation of the schwinger model and symmetry protection with trapped ions. *PRX Quantum*, 3(2):020324, 2022.

[54] Michael A Nielsen and Isaac L Chuang. Quantum computation and quantum information. *Phys. Today*, 54(2):60, 2001.

[55] Pedro Parrado-Rodríguez, Ciarán Ryan-Anderson, Alejandro Bermudez, and Markus Müller. Crosstalk suppression for fault-tolerant quantum error correction with trapped ions. *Preprint at https://arxiv.org/abs/2012.11366*, 2020.

[56] Pedro Parrado-Rodríguez, Ciarán Ryan-Anderson, Alejandro Bermudez, and Markus Müller. Crosstalk suppression for fault-tolerant quantum error correction with trapped ions. *Quantum*, 5:487, 2021.

[57] Wolfgang Paul and Helmut Steinwedel. Ein neues massenspektrometer ohne magnetfeld. *Zeitschrift für Naturforschung A*, 8(7):448–450, 1953.

[58] F. Pedregosa, G. Varoquaux, A. Gramfort, V. Michel, B. Thirion, O. Grisel, M. Blondel, P. Prettenhofer, R. Weiss, V. Dubourg, J. Vanderplas, A. Passos, D. Cournapeau, M. Brucher, M. Perrot, and E. Duchesnay. Scikit-learn: Machine learning in Python. *Journal of Machine Learning Research*, 12:2825–2830, 2011.

[59] M Roberts, P Taylor, SV Gateva-Kostova, RBM Clarke, WRC Rowley, and P Gill. Measurement of the 2 s 1/2- 2 d 5/2 clock transition in a single 171 yb+ ion. *Physical Review A*, 60(4):2867, 1999.

[60] H Schweppe. Elastic and piezoelectric properties of paratellurite (teo2). *Ultrasonics*, 8(2):84–87, 1970.

[61] Chung-You Shih. Holographic optical manipulation of trapped ions for quantum simulation. Master's thesis, University of Waterloo, 2019.

[62] Chung-You Shih, Sainath Motlakunta, Nikhil Kotibhaskar, Manas Sajjan, Roland Hablützel, and Rajibul Islam. Reprogrammable and high-precision holographic optical addressing of trapped ions for scalable quantum control. *npj Quantum Information*, 7(1):57, 2021.

[63] Jacob Smith, Aaron Lee, Philip Richerme, Brian Neyenhuis, Paul W Hess, Philipp Hauke, Markus Heyl, David A Huse, and Christopher Monroe. Many-body localization in a quantum simulator with programmable random disorder. *Nature Physics*, 12(10):907–911, 2016.

[64] Anders Sørensen and Klaus Mølmer. Quantum computation with ions in thermal motion. *Physical review letters*, 82(9):1971, 1999.

[65] Gregor Thalhammer, Richard W Bowman, Gordon D Love, Miles J Padgett, and Monika Ritsch-Marte. Speeding up liquid crystal slms using overdrive with phase change reduction. *Optics express*, 21(2):1779–1797, 2013.

[66] Stefan Van der Walt, Johannes L Schönberger, Juan Nunez-Iglesias, François Boulogne, Joshua D Warner, Neil Yager, Emmanuelle Gouillart, and Tony Yu. scikit-image: image processing in python. *PeerJ*, 2:e453, 2014.

[67] Anthony Vogliano. Coherent interactions and thermometry in a trapped ion quantum simulator. Master's thesis, University of Waterloo, 2022.

[68] Pengfei Wang, Chun-Yang Luan, Mu Qiao, Mark Um, Junhua Zhang, Ye Wang, Xiao Yuan, Mile Gu, Jingning Zhang, and Kihwan Kim. Single ion qubit with estimated coherence time exceeding one hour. *Nature communications*, 12(1):233, 2021.

[69] Brendan M White, Pei Jiang Low, Yvette de Sereville, Matthew L Day, Noah Greenberg, Richard Rademacher, and Crystal Senko. Isotope-selective laser ablation ion-trap loading of ba+ 137 using a bacl 2 target. *Physical Review A*, 105(3):033102, 2022.

[70] Frank Wyrowski. Iterative quantization of digital amplitude holograms. *Applied optics*, 28(18):3864–3870, 1989.

[71] N Yu and L Maleki. Lifetime measurements of the 4 f 14 5 d metastable states in single ytterbium ions. *Physical Review A*, 61(2):022507, 2000.

[72] Ilia Vladimirovich Zalivako, Il'ya Aleksandrovich Semerikov, Aleksandr Stanislavovich Borisenko, Mikhail Dmitrievich Aksenov, K Yu Khabarova, and Nikolai Nikolaevich Kolachevsky. Experimental study of the optical qubit on the 435-nm quadrupole transition in the 171 yb+ ion. *JETP Letters*, 114:59–64, 2021.

[73] Jiehang Zhang, Paul W Hess, A Kyprianidis, Petra Becker, A Lee, J Smith, Gaetano Pagano, I-D Potirniche, Andrew C Potter, Ashvin Vishwanath, et al. Observation of a discrete time crystal. *Nature*, 543(7644):217–220, 2017.

[74] Daiwei Zhu, S Johri, NH Nguyen, C Huerta Alderete, KA Landsman, NM Linke, C Monroe, and AY Matsuura. Probing many-body localization on a noisy quantum computer. *Physical Review A*, 103(3):032606, 2021.

[75] Philip Zupancic, Philipp M Preiss, Ruichao Ma, Alexander Lukin, M Eric Tai, Matthew Rispoli, Rajibul Islam, and Markus Greiner. Ultra-precise holographic beam shaping for microscopic quantum control. *Optics express*, 24(13):13881–13893, 2016.

APPENDICES

Appendix A

Phase Profile Extraction

The interference fringes in IP1 (in Fig. 4.3b for example) are sampled by the camera C1 as a 2D array. We crop the array within a region of interest (ROI) for phase extraction. The cropped array is denoted as $I^{xy}(m_\mathrm{p}, n_\mathrm{p})$ where $\mathbf{\Delta} \equiv (x, y)$ denotes the coordinate of the scanning patch relative to the reference patch in the DMD FP, and $(m_\mathrm{p}, n_\mathrm{p})$ denotes the coordinates of camera pixels. Here, m and n denote the two spatial directions of the fringes on the camera. We first calculate the spectrum S^{xy} of I^{xy} with a 2D fast Fourier transformation (FFT),

$$S^{xy} = \mathrm{abs}(\mathrm{FFT}[I^{xy}]). \tag{A.1}$$

Next, we apply a high-pass filter (HPF) to filter out the low spatial frequency background envelope of I^{xy} and retrieve the spatial frequency of the interference fringes $(\kappa_m^{xy}, \kappa_n^{xy})$,

$$(|\kappa_m^{xy}|, |\kappa_n^{xy}|) = \mathrm{abs}(\mathrm{argmax}[\mathrm{HPF}[S^{xy}]]). \tag{A.2}$$

A robust estimate for $(\kappa_m^{xy}, \kappa_n^{xy})$, that is insensitive to shot-to-shot fluctuations in the interference fringes, can be obtained by finding their linear functional dependence on the FP coordinates (x, y), as

$$\kappa_m^{xy} = ax + by, \ a > 0 \tag{A.3}$$
$$\kappa_n^{xy} = a'x + b'y, \ a' < 0. \tag{A.4}$$

Here, a, a', b, b' are fitting parameters. The relative negative sign between a and a' is due to the fact that the camera is facing opposite to the beam pointing direction. From the two spatial frequencies, we can construct a complex plane wave fringe profile,

$$T^{xy}(m_\mathrm{p}, n_\mathrm{p}) = \exp(\mathrm{i}(\kappa_m^{xy}(m_\mathrm{p} - m_c) + \kappa_n^{xy}(n_\mathrm{p} - n_c))), \tag{A.5}$$

where (m_c, n_c) is the coordinate of the user-defined center of the interference fringes. The phase of the FP at (x, y) is computed from,

$$\phi(x, y) = \text{angle}(\sum_{m_\text{p}, n_\text{p}} (T^{xy} \cdot I^{xy})). \tag{A.6}$$